

ALMA MATER STUDIORUM · UNIVERSITY OF BOLOGNA

---

School of Science  
Department of Physics and Astronomy  
Master Degree in Physics

# Measurement of quantum correlations in the $WZ$ system at the LHC

Supervisor:  
Prof. Fabio Maltoni

Submitted by:  
Nicola Forti

Co-supervisor:  
Dr. Federica Fabbri

Academic Year 2023/2024



# Abstract

The study of heavy vector bosons has been fundamental both for the understanding and testing the prediction of the Standard Model and for exploring the potential existence of new physics. In recent years, a new approach to study particle physics is quickly developing using quantum information principle and inspired observables to investigate relations between particles created at colliders. In this thesis, it has been analyzed the bipartite qutrit system resulting from the process  $pp \rightarrow W^\pm Z$ , where the produced bosons decay into leptonic final states. The spin density matrix of the process has been derived by applying a quantum tomography approach to the simulated final state. This procedure allows to derive information on the heavy bosons' spin by exploiting the angular distribution of the decay products. The key measurement in this thesis is the lower bound of the concurrence, which is a quantum observable sensitive to the entanglement between the  $WZ$  spin. During the analysis, realistic selections and reconstruction procedures have been included to estimate the realistic effects that will affect such measurement performed in collider experiments. Moreover, a dedicated statistical analysis is employed to recover the observable of interest and estimate the corresponding statistical uncertainties expected to be achievable at the LHC. The analysis results indicate that measuring entanglement between the  $W$  and  $Z$  bosons is feasible, though it would be highly challenging with the current Run 3 dataset.



# Contents

<b>Introduction</b>	<b>6</b>
<b>1 The Standard Model</b>	<b>8</b>
1.1 Classification of fundamental particles . . . . .	8
1.2 Gauge invariance in the Electroweak theory . . . . .	11
1.3 The Spontaneous Symmetry Breaking of EW theory and Higgs Mechanism	13
1.4 Diboson Production at the LHC . . . . .	17
1.4.1 $pp$ collision at LHC . . . . .	18
1.4.2 $WZ$ Diboson Production . . . . .	20
<b>2 Quantum Information</b>	<b>23</b>
2.1 Postulates of Quantum Mechanics . . . . .	23
2.2 The Qubit . . . . .	26
2.3 The Density operator . . . . .	28
2.4 Entanglement . . . . .	31
<b>3 Quantum State Tomography and Qutrit Formalism</b>	<b>36</b>
3.1 Generalized Gell-Mann parameterizations . . . . .	36
3.2 Weyl-Wigner formalism for spin-1 particle . . . . .	39
3.3 Concurrence . . . . .	45
<b>4 Data analysis</b>	<b>48</b>
4.1 Monte Carlo Simulation . . . . .	48
4.2 Event selections . . . . .	49
4.2.1 Reconstruction of the $p_z$ component of the neutrino momentum .	52
4.3 Basis choice . . . . .	54
4.4 Measurement of spin density matrix coefficients . . . . .	56
4.4.1 Differences between Parton and Particle level . . . . .	59
4.4.2 Studies with different analysis limitations . . . . .	61
4.5 Unfolding . . . . .	63
4.6 Bootstrap method . . . . .	66

4.7	Measurement of the Concurrence . . . . .	68
4.7.1	Concurrence in different phase space regions . . . . .	71
4.7.2	Transverse momentum selection . . . . .	74

# Introduction

The  $W$  and  $Z$  bosons are fundamental particles that mediate the weak force, one of the four fundamental forces in nature, as described by the Standard Model (SM) of particle physics. The study of these heavy vector bosons performed at the Large Hadron Collider (LHC) is fundamental for testing SM predictions at high energy scales and providing a window into potential new physics beyond the current framework. In recent years, a new approach to studying particle physics has emerged using quantum information principles and inspired observables to investigate the fundamental properties of particles created at colliders. The spin density matrix, in particular, is a fundamental tool for describing the spin state of a quantum system. This thesis presents a study of the process  $pp \rightarrow W^\pm Z$ , where the resulting bosons decay into leptonic final states. The focus is on analyzing the entanglement of the bipartite quantum state formed by the spin of the two heavy vector bosons. This is the first feasibility study of the entanglement for  $W^\pm Z$  bosons including realistic selections and reconstruction effects. The analysis is conducted using quantum state tomography, which allows for determining the spin density matrix of the diboson system from an ensemble of measurements. In particular, the spin density matrix is reconstructed by analyzing the direction of the decay products of the  $WZ$  system. The primary quantum observable examined in this work is the concurrence, which is used to determine whether the state is entangled. However, for a pair of qutrits, the concurrence cannot be measured directly. Instead, this analysis measures a lower bound on the concurrence, which can be used to confirm entanglement in the state. Moreover, the lower bound depends on all the coefficients of the spin density matrix of the  $WZ$  system, making its measurement very challenging. The reconstruction of this quantity and the estimate of the statistical uncertainty are conducted to evaluate whether this type of measurement is feasible within the ATLAS and CMS collaborations, while also identifying the primary limitations of such an approach. In addition, various phase space selections are studied to enhance the entanglement between the two bosons, and consequently the possibility to observe it using real data collected at LHC.

Chapter 1 presents the theoretical foundation of the Standard Model of particle physics, providing a description of electroweak theory, spontaneous symmetry breaking, and the Higgs mechanism. Finally, it gives an overview of the phenomenology of proton-proton collisions at LHC, focusing on the production of  $W^\pm Z$  diboson.

Chapter 2 introduces quantum mechanics and quantum information theory, starting with the postulates of quantum mechanics followed by a description of the qubit and density matrix operator. The chapter concludes by exploring the concept of entanglement, including an overview of two key quantum observables: concurrence and the Bell inequality.

Chapter 3 outlines the method used in this thesis to determine the spin density matrix for the  $WZ$  system, represented by a pair of qutrits. It also details the calculations required to compute the primary observable in this analysis, the lower bound of the concurrence.

Chapter 4 presents the detailed analysis performed on the  $W^\pm Z$  systems using a Monte Carlo simulation. It begins by detailing the event generation and selection processes, followed by the measurement of the spin density matrix and concurrence. The chapter also presents the results and explores these measurements across various regions of phase space and under different selection criteria.

The Conclusions contains a discussion and consideration of the results obtained with a future outlook of the measurement.

# Chapter 1

## The Standard Model

The Standard Model of particle physics is a comprehensive theory that describes the fundamental particles and their interactions, excluding gravity. The Standard Model, developed in the latter half of the twentieth century by numerous physicists, has proved very successful in explaining a wide range of phenomena and has withstood rigorous experimental tests. This chapter presents an overview of the Standard Model, including its key components and the theoretical framework that supports it.

### 1.1 Classification of fundamental particles

Fundamental particles, also known as elementary particles, are crucial for understanding the structure and behaviour of matter and the universe. They constitute the basis of the Standard Model, which successfully describes the vast majority of known phenomena and experimental discoveries in particle physics.

In the SM, fundamental particles are categorized as either fermions or bosons, as illustrated in Figure 1.1. Fermions, which are the particles that constitute matter, have half-integer spin ( $s = \frac{1}{2}$ ) and obey Fermi-Dirac statistics. Moreover, they follow the Pauli exclusion principle, which states that two fermions can not simultaneously occupy the same quantum state. Fermions are further classified as three families of leptons and three families of quarks. In the Standard Model, leptons are grouped in doublets as follows

$$\begin{pmatrix} \nu_e \\ e \end{pmatrix} \quad \begin{pmatrix} \nu_\mu \\ \mu \end{pmatrix} \quad \begin{pmatrix} \nu_\tau \\ \tau \end{pmatrix}.$$

Each lepton family consists of a negatively charged lepton—namely, the electron ( $e$ ), muon ( $\mu$ ), and tau ( $\tau$ )—paired with a corresponding neutral lepton, known as a neutrino, specific to each family:  $\nu_e$ ,  $\nu_\mu$ , and  $\nu_\tau$ . The charged leptons are *colourless* and interact through both the electromagnetic and weak forces, whereas neutrinos interact only through the weak force, making them extremely difficult to detect.

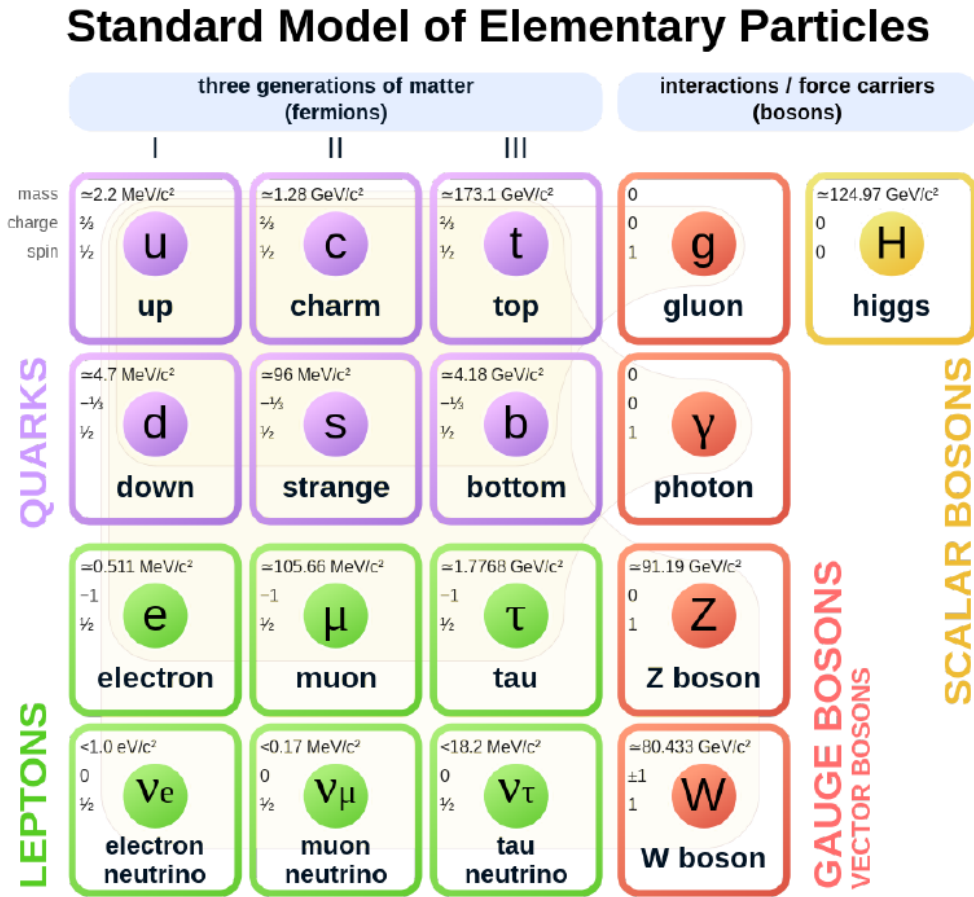


Figure 1.1: The Standard Model fundamental particles reported with some properties.

In the same way, quarks are divided into three doublets as follows:

$$\begin{pmatrix} u \\ d \end{pmatrix} \quad \begin{pmatrix} c \\ s \end{pmatrix} \quad \begin{pmatrix} t \\ b \end{pmatrix}$$

where the *up-like* quarks ( $u, c, t$ ) have a positive electric charge of  $\frac{2}{3}$ , while the *down-like* quarks have a negative charge of  $-\frac{1}{3}$ . Furthermore, quarks have three different colour charges, which are connected to their ability to interact through strong force. In the Standard Model, each particle has a corresponding antiparticle with the same mass but opposite physical charges, such as electric charge.

Bosons	Symbols	Spin	Mass ( $GeV/c^2$ )
Photon (1)	$\gamma$	1	0
Gluons (8)	$g$	1	0
W's and Z (3)	$W^\pm, Z$	1	$80.3692 \pm 0.0133$ $91.1876 \pm 0.0021$
Higgs (1)	$H$	0	$125.25 \pm 0.17$

Table 1.1: Summary of the Standard Model bosons [29].

The SM also includes several bosons, as illustrated in Table 1.1. These are the fundamental particles that mediate the interactions included in the SM: electroweak, strong and the Higgs interaction. Unlike fermions, bosons follow Bose-Einstein statistics, which allows multiple bosons to occupy the same quantum state. This property is crucial for their role in force mediation. Bosons can be classified into two types based on their spin: vector bosons and scalar bosons. Vector bosons have a spin  $s = 1$ , while scalar bosons have a spin  $s = 0$ . The only scalar boson known within the Standard Model is the Higgs boson, which plays a crucial role in the mechanism of mass generation for other particles through the Higgs mechanism.

The vector bosons are gauge bosons linked with the Standard Model's three fundamental interactions: the strong, electromagnetic, and weak forces. Specifically, the eight gluons are responsible for mediating the strong force, which operates between quarks and binds them together to form protons, neutrons, and other hadrons. Gluons are massless bosons that carry a colour charge, which is analogous to the electric charge in electromagnetism but comes in three types (red, green, blue) and their corresponding anticolours. These particles can interact with each other because they carry colour charges. This leads to the property of confinement, where quarks and gluons are always bound together in colour-neutral combinations, preventing them from being observed as free particles. The photon is the electromagnetic force's gauge boson, it is charge-less and mediates interactions between charged particles. Finally, the  $W^\pm$  and  $Z$  bosons are the weak interaction mediators. These bosons are massive, with the  $W$  bosons carrying an electric charge and the  $Z$  boson being electrically neutral.

## 1.2 Gauge invariance in the Electroweak theory

Formally, the Standard Model theory is based on a gauge principle of local invariance and is described mathematically by three different gauge symmetry groups, nominally

$$SU(3)_C \otimes SU(2)_L \otimes U(1)_Y$$

where each term of the product represents respectively:

- The non-Abelian group  $SU(3)_C$  is responsible for the strong interaction, also known as quantum chromodynamics (QCD) between quarks and gluons. This group has 8 generators, known as the Gell-Mann matrices representing the number of the gauge vector bosons of QCD. The  $SU(3)_C$  group is characterized by its own type of charge, known as the colour charge, which comes in three varieties.
- The non-Abelian group  $SU(2)_L$  is the gauge group associated with the weak interaction, where the subscript stands for the "left-handed", indicating that it acts on left-handed fermions.
- The Abelian group  $U(1)_Y$  is the group responsible for electrodynamics (QED) and its quantum number is the hypercharge, related to electric charge and weak interaction.

The theory that unifies electromagnetism and weak interaction is the Electroweak (EW) theory, formulated by Glashow, Salam and Weinberg in the 1960s [27]. It based on the symmetry subgroup  $SU(2)_L \otimes U(1)_Y$ , where  $SU(2)_L$  can be represented with the three generators of weak isospin  $I_i = \frac{\tau_i}{2}$ , where  $\tau_i$  are Pauli matrices, and the group  $U(1)_Y$  is associated with the hypercharge  $Y$ , defined through the Gell-Mann–Nishijima relation:

$$Q = I_3 + \frac{Y}{2} \quad (1.1)$$

To construct the theory, the  $SU(2)_L \otimes U(1)_Y$  group must satisfy local gauge invariance, for this reason, four gauge bosons are introduced

$$\begin{aligned} b_\mu^1, b_\mu^2, b_\mu^3 & \text{ for } SU(2)_L, \\ A_\mu & \text{ for } U(1)_Y \end{aligned} \quad (1.2)$$

associated with weak isospin and hypercharge groups. Inside the electroweak theory, fermions are in doublets of left-handed particles and right-handed singlets as follows

$$\begin{aligned} L_q &= \begin{pmatrix} u \\ d \end{pmatrix}_L, & R_u &= u_R, & R_d &= d_R \\ L_l &= \begin{pmatrix} \nu_l \\ l \end{pmatrix}_L, & R_l &= l_R \end{aligned} \quad (1.3)$$

where  $u$  and  $d$  are the *up-like* and *down-like* quark component of each family, while  $\nu_l$  and  $l$  represent the neutrino and lepton for each family. In the Standard Model, the right-handed neutrino is not included, since it hasn't been observed yet in nature. This classification of fermions is fundamental in understanding the behaviour of particles under the electroweak interaction and it is linked to the concept of chirality and helicity. In particular, helicity refers to the projection of a particle's spin along its direction of motion. The helicity operator is defined as

$$h = \frac{\vec{S} \cdot \vec{p}}{|\vec{p}|}, \quad (1.4)$$

where  $\vec{S}$  is the spin operator and  $\vec{p}$  is the momentum of the particle. For example, if a particle with spin-1 moves exactly in the same direction as its spin points then the helicity is  $h = +1$ , while if it moves in the exact opposite direction, the helicity is  $h = -1$ . This property, since is related to the momentum of the particle, depends on the reference frame. Chirality instead is a more abstract concept related to the intrinsic handedness of particles. It is a property of the particle's field rather than its physical spin direction. Chirality is described by the projection operators:

$$P_L = \frac{1 - \gamma^5}{2} \quad \text{and} \quad P_R = \frac{1 + \gamma^5}{2} \quad (1.5)$$

where  $\gamma^5$  is the Dirac matrix. States with left-handed chirality have a non-zero  $P_L$  projection, whereas right-handed chirality states have a  $P_R$  projection. For massless particles, chirality is the same as helicity. For massive particles, it is important to differentiate between chirality and helicity. For these particles, an observer can change to a reference frame moving faster than the spinning particle, in which case the particle will then appear to move backwards, and its helicity will be reversed. This means that helicity is conserved within a given reference frame but is not Lorentz invariant, whereas chirality is Lorentz invariant but not a constant of motion. Therefore, chirality is a fundamental concept for the Standard Model since the electroweak interaction, which is described by the symmetry group  $SU(2)_L \otimes U(1)_Y$ , where  $SU(2)_L$  acts only on left-handed doublets.

The Lagrangian for the electroweak theory associated with one generation of quarks and leptons can be written as:

$$\mathcal{L}_{EW} = \mathcal{L}_{gauge} + \mathcal{L}_{fermions} \quad (1.6)$$

where  $\mathcal{L}_{gauge}$  describes the four gauge bosons and  $\mathcal{L}_{fermions}$  describes fermions and their interaction with bosons. In particular, the kinetic term of the gauge bosons can be formulated as

$$\mathcal{L}_{gauge} = -\frac{1}{4} F_{\mu\nu}^i F^{i\mu\nu} - \frac{1}{4} f_{\mu\nu} f^{\mu\nu} \quad (1.7)$$

in which,  $F_{\mu\nu}^i$  is the field-strength tensor for the  $SU(2)_L$  gauge bosons, defined as

$$F_{\mu\nu}^i = \partial_\nu b_\mu^i - \partial_\mu b_\nu^i + g\varepsilon_{ijk}b_\mu^j b_\nu^k \quad (1.8)$$

with  $\varepsilon_{ijk}$  the Levi-Civita symbol denoting the structure constant of  $SU(2)_L$  group and  $g$  the coupling constant of the this group. Meanwhile, the field-strength tensor  $f_{\mu\nu}$  is related to the Abelian group  $U(1)_Y$  and can be written as follows

$$f_{\mu\nu} = \partial_\nu A_\mu - \partial_\mu A_\nu. \quad (1.9)$$

The Lagrangian of the fermions is defined as

$$\mathcal{L}_{fermions} = \bar{R}_l i\gamma^\mu D_\mu R_l + \bar{L}_l i\gamma^\mu D_\mu L_l + \bar{R}_u i\gamma^\mu D_\mu R_u + \bar{R}_d i\gamma^\mu D_\mu R_d + \bar{L}_q i\gamma^\mu D_\mu L_q, \quad (1.10)$$

where the covariant derivative  $D_\mu$  for singlets is

$$D_\mu = \partial_\mu + \frac{ig'}{2}A_\mu Y \quad (1.11)$$

with  $g'$  the coupling constant of the group  $U(1)_Y$  and  $Y$  the hypercharge of the corresponding particle. In the case of doublets, the covariant derivative can be written as

$$D_\mu = \partial_\mu + \frac{ig'}{2}A_\mu Y + \frac{ig}{2}\tau^i b_\mu^i, \quad (1.12)$$

where  $\tau^i$  are the generators of the  $SU(2)$  group, i.e. the Pauli matrices. Using the definition of Lagrangians just described, Eq.(1.6) can be reformulated to make the interaction terms between fermions and gauge bosons of the EW theory explicit. Moreover, it can be noticed that the Lagrangian of the electroweak lacks mass terms for both fermions and gauge bosons, while it is known that fermions are massive and there is only one massless boson in EW theory: the photon.

### 1.3 The Spontaneous Symmetry Breaking of EW theory and Higgs Mechanism

As explained in the previous section, a mechanism is needed to give mass to these fundamental particles without introducing an explicit mass term. Adding a mass term for, e.g., the fermions would break the  $SU(2)_L \otimes U(1)_Y$  gauge invariance of the theory. This purpose can be achieved within the Standard Model via the Brout-Englert-Higgs mechanism as a consequence of the electroweak spontaneous symmetry breaking.[28]

In particular,  $SU(2)_L \otimes U(1)_Y$  is broken by the vacuum expectation value ( $vev$ ) of a complex doublet of scalar field with hypercharge  $Y = +1$  called Higgs multiplet

$$\phi \equiv \begin{pmatrix} \phi^\dagger \\ \phi^0 \end{pmatrix} = \frac{1}{\sqrt{2}} \begin{pmatrix} \phi^1 + i\phi^2 \\ \phi^3 + i\phi^4 \end{pmatrix} \quad (1.13)$$

The Lagrangian (1.6) can now be extended by introducing a new term associated with the complex scalar field  $\phi$  and a term describing the interaction between fermions and the scalar field. The first term added to the electroweak Lagrangian is

$$\mathcal{L}_{scalar} = (D^\mu \phi)^\dagger (D_\mu \phi) - V(\phi^\dagger \phi) \quad (1.14)$$

where  $D_\mu$  is the gauge covariant derivative described in Eq.(1.12) and the potential  $V(\phi^\dagger \phi)$  can be written as

$$V(\phi^\dagger \phi) = \mu^2 (\phi^\dagger \phi) + |\lambda| (\phi^\dagger \phi)^2 \quad \text{with } \lambda > 0 \quad (1.15)$$

The interaction term, which involves Yukawa couplings of the scalars to fermions, is described by

$$\mathcal{L}_{Yukawa} = -\zeta_l \bar{R}_l (\phi^\dagger L_l) - \zeta_d \bar{L}_q \phi R_d - \zeta_u \bar{L}_q \tilde{\phi} R_u + h.c. \quad (1.16)$$

where  $\tilde{\phi} = i\tau_2 \phi^*$ , with  $\tau_2$  the second Pauli matrix, is the complex conjugate of Higgs doublet and  $\zeta_l, \zeta_u, \zeta_d$  are the Yukawa coupling constant for leptons and up-like and down-like quarks. Let's now recall the Higgs potential to study how it changes depending on the sign of the parameter  $\mu^2$ . It is possible to distinguish two different cases:

- if  $\mu^2 > 0$ , the potential function has a unique minimum at  $\phi = 0$ , corresponding to the vacuum. In this case, the symmetry would be manifest.
- if  $\mu^2 < 0$ , the potential takes the typical form of a "Mexican hat" and the minima are described by a circle of radius  $v = \sqrt{\mu^2/\lambda}$  known as vacuum expectation value. This leads to the spontaneous symmetry breaking of the  $SU(2)_L \otimes U(1)_Y$  into the  $U(1)_{EM}$  gauge group.

Thus the Lagrangian can be expanded around one of the possible ground states, considering for simplicity the ground state  $\phi_0$  defined as

$$\phi_0 = \langle 0 | \phi | 0 \rangle = \frac{1}{\sqrt{2}} \begin{pmatrix} 0 \\ v \end{pmatrix}. \quad (1.17)$$

and rewriting the potential minimum in a more general way as

$$\phi = \exp\left(\frac{i\pi^a \tau^a}{2v}\right) \begin{pmatrix} 0 \\ (v+h)/\sqrt{2} \end{pmatrix} \quad (1.18)$$

where  $\tau^a$  are the  $SU(2)$  generators,  $\pi^a$  represent an arbitrary phase and  $h$  the scalar Higgs boson. The Lagrangian can now be rewritten in terms of the unitary gauge, in particular, the kinetic term becomes:

$$\mathcal{L}_{kin} = (D^\mu \phi)^\dagger (D_\mu \phi) = \frac{(v+h)^2}{8} \left[ g^2 |b_\mu^1 - ib_\mu^2|^2 + (g'A_\mu - gb_\mu^3)^2 \right] + \frac{1}{2} (\partial^\mu h) (\partial_\mu h) \quad (1.19)$$

with  $v = 246.22$  GeV the vacuum expectation value of the EW theory. The gauge bosons can be redefined through a linear combination obtaining the physical  $W^\pm$ ,  $Z$  and photon bosons as follows:

$$W_\mu^\pm \equiv \frac{b_\mu^1 \mp ib_\mu^2}{\sqrt{2}}, \quad (1.20)$$

$$Z_\mu \equiv \frac{-g'A_\mu + gb_\mu^3}{\sqrt{g^2 + g'^2}} = -A_\mu \sin \theta_w + b_\mu^3 \cos \theta_w, \quad (1.21)$$

$$A_\mu \equiv \frac{gA_\mu + g'b_\mu^3}{\sqrt{g^2 + g'^2}} = A_\mu \cos \theta_w + b_\mu^3 \sin \theta_w. \quad (1.22)$$

where  $\theta_w$  is the electroweak mixing angle, known as the Weinberg angle, which relates the coupling  $g$  and  $g'$  through the following definition

$$g' \equiv g \tan \theta_w. \quad (1.23)$$

Using Eqs. (1.20) and (1.21) within the Lagrangian (1.19), additional terms are obtained as shown below

$$\mathcal{L}_{kin} = \frac{g^2 v^2}{4} W_\mu^+ W^{-\mu} + \frac{(g^2 + g'^2) v^2}{8} Z_\mu Z^\mu + \dots \quad (1.24)$$

From these quadratic terms, the masses of the  $W$ ,  $Z$  electroweak gauge bosons can ultimately be expressed as

$$m_Z = \frac{v \sqrt{g^2 + g'^2}}{2}, \quad m_W = m_Z \cos \theta_w = \frac{gv}{2}. \quad (1.25)$$

The potential of the scalar Lagrangian (1.14) can be rewritten now in function of the field  $h$  as

$$V(h) = \frac{1}{2} (2\lambda v^2) h^2 + \lambda v h^3 + \frac{\lambda}{4} h^4 \quad (1.26)$$

where it can be noticed that the Higgs field has acquired a mass defined as

$$m_H = \sqrt{-2\mu^2} = \sqrt{2\lambda v} \quad (1.27)$$

The BEH mechanism is not only able to give mass to gauge bosons but is also responsible for giving mass to fermions, which otherwise would be massless due to the gauge

invariance of the theory. Thus, the Yukawa term (1.16) added to the Lagrangian of EW theory becomes

$$\begin{aligned} \mathcal{L}_{yukawa} = & -\frac{v}{\sqrt{2}}(\zeta_l \bar{l}_L l_R + \bar{d}_L \zeta_d d_R + \bar{u}_L \zeta_u u_R) + h.c. \\ & + \text{interaction terms} \end{aligned} \quad (1.28)$$

where the mass of fermions can be written in general as

$$m_i = \frac{\zeta_i v}{\sqrt{2}} \quad (1.29)$$

with  $\zeta_i$  Yukawa coupling of the respective fermion.

Let's consider the fermion Lagrangian (1.10) and expand it using the redefinition of the gauge bosons (1.20-1.22). The term between fermions and gauge field can be written as follows

$$\begin{aligned} \mathcal{L}_{fermions} = & g(W_\mu^+ J_W^{\mu+} + W_\mu^- J_W^{\mu-} + Z_\mu J_Z^\mu) + \mathcal{A}_\mu J_{EM}^\mu \\ & + \text{kinetic terms} \end{aligned} \quad (1.30)$$

where  $J_i^\mu$  are the current for the different interaction of processes and  $e$  is the electric charge of the electron defined as

$$e = \frac{gg'}{\sqrt{g^2 + g'^2}} = g \sin \theta_W \quad (1.31)$$

Each current can be expressed as

$$\begin{aligned} J_W^{\mu+} &= \frac{1}{2\sqrt{2}} \sum_i (\bar{\nu}^i \gamma^\mu (1 - \gamma^5) e^i + \bar{u}^i \gamma^\mu (1 - \gamma^5) d^i), \\ J_W^{\mu-} &= \frac{1}{2\sqrt{2}} \sum_i (\bar{e}^i \gamma^\mu (1 - \gamma^5) \nu^i + \bar{d}^i \gamma^\mu (1 - \gamma^5) u^i), \\ J_Z^\mu &= \frac{1}{4 \cos \theta_W} \sum_i [\bar{\Psi}^i \gamma^\mu (V_f - A_f \gamma^5) \Psi^i], \\ J_{EM}^\mu &= \sum_i Q_i \bar{\Psi}^i \gamma^\mu \Psi^i, \end{aligned} \quad (1.32)$$

where in the first two currents,  $\nu^i, e^i, u^i, d^i$  are neutrinos, electron and up-like and down-type quarks. In the third equation, the angle  $\theta_W$  is the Weinberg angle,  $V_f$  and  $A_f$  are the vector and axial-vector coupling constants and  $\Psi^i$  are generic charged fermions with charge  $Q^i$ . Figure 1.2 displays how the  $W$  and  $Z$  bosons interact with fermions.

In particular, the  $Z$  boson is the mediator of the neutral current (NC) interactions 1.2a where the electric charge of the particles involved does not change in the interaction

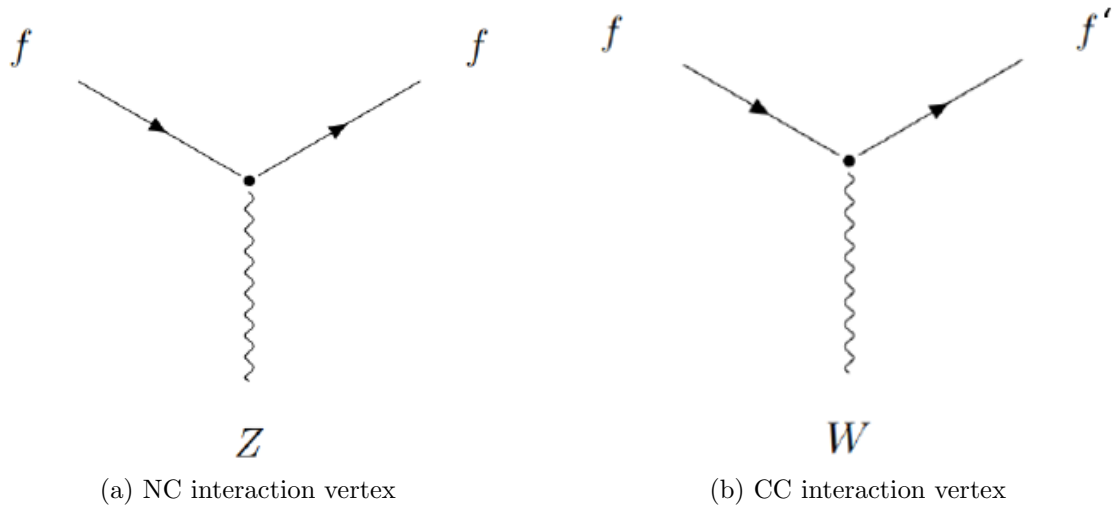


Figure 1.2: Feynman diagrams of the neutral and charged current interaction in the electroweak theory for the  $Z$  and  $W$  bosons.

and it is described by  $J_Z^\mu$  in Eq.(1.32). An important characteristic of the  $Z$  boson as a mediator in the Standard Model is that it does not allow a change in particle flavour in the interaction. The  $W^\pm$  boson is the mediator of charged current (CC) interactions, in which the electric charge of the particles involved changes as a result of the interaction, as shown in Fig.1.2b. The interaction is described by  $J_W^{\mu-}$  and  $J_W^{\mu+}$  in Eq.(1.32). In particular, interactions mediated by the  $W$  boson occur with higher probability within the same family of quarks or leptons, although interactions between different families are possible but highly suppressed. This suppression is linked to the Cabibbo-Kobayashi-Maskawa (CKM) matrix, which governs the strength of flavour-changing processes in the SM .

## 1.4 Diboson Production at the LHC

As described in the previous section, the electroweak interactions in the SM are governed by the non-Abelian  $SU(2)_L \otimes U(1)_Y$  gauge group. Investigating diboson production at LHC provides a fundamental test of the electroweak theory at the TeV scale. One particular example is the precise measurement of the triple gauge boson couplings, which could provide sensitive probes of new physics. Moreover, diboson production measurements are crucial, as these processes and their decay products constitute an irreducible background for Higgs and new physics searches.

### 1.4.1 $pp$ collision at LHC

The Large Hadron Collider (LHC) is primarily a proton-proton ( $pp$ ) collider, where particles are accelerated to very high energies. The proton is a hadron, a subatomic particle composed of three valence quarks bound together by gluons: two  $up$  quarks and one  $down$  quark, carrying an electric charge of +1 and a total colour charge equal to zero. Gluons continuously interact inside the proton, giving rise to pairs of quark-antiquark, known as "sea" quarks. Protons undergo head-on collisions with a center-of-mass energy of up to 13.6 TeV. Figure 1.3 sketches a simplification of  $pp$  interaction showing the outgoing products.

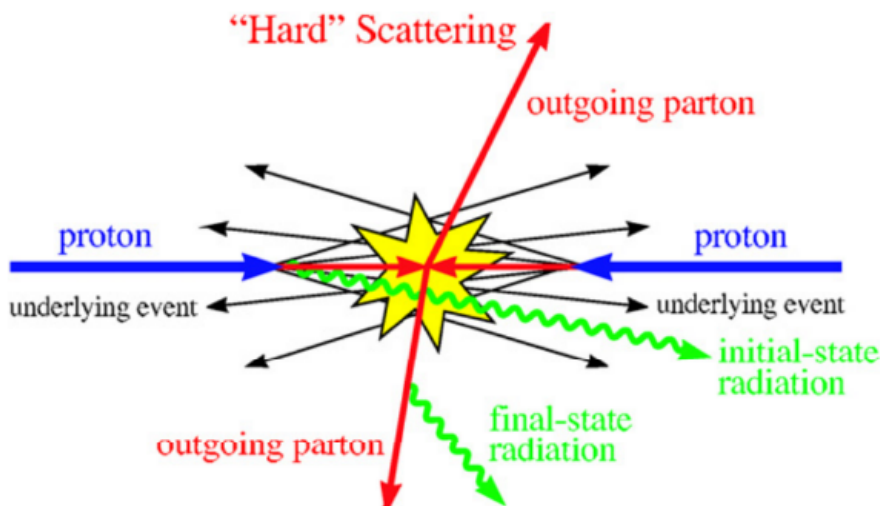


Figure 1.3: Representation of a  $pp$  collision showing a hard scattering process between partons

In proton collisions, there can be two types of events depending on the energy in which protons interact. At low energies, elastic scattering takes place, where the protons collide but their internal structure remains intact. At high energies, inelastic scattering dominates, allowing the quarks and gluons inside the protons to interact. At this energy, 'hard-scattering' processes, which are extensively studied, can instead be described by perturbative QCD (pQCD) due to the asymptotic freedom of the theory [18].

The total cross-section of hard interactions can be computed using the factorization theorem, which accounts for both soft and hard scattering collisions. Considering a hard-scattering event of the type  $AB \rightarrow X$  depicted in Figure 1.4, the total cross-section, using factorization theorems [15], can be written as

$$\sigma_{AB \rightarrow X} = \sum_{a,b} \int dx_a dx_b f_{a/A}(x_a, Q^2) f_{b/B}(x_b, Q^2) \hat{\sigma}_{ab \rightarrow X} \quad (1.33)$$

where  $x_{a,b}$  represents the momentum fractions of the two interacting partons and  $f_{n/N}(x_n, Q^2)$  are the Parton Distribution Functions (PDFs) for the two partons  $a, b$  generated from hadrons  $A, B$  with  $Q^2$  being the momentum scale that characterizes the scattering. Figure 1.5 shows the gluon and valence PDFs obtained by measurements performed at different colliders. The valence quarks (up and down) carry the majority of the proton's momentum, with a significant probability peak around  $x = \frac{1}{3}$ . The distribution of up quarks is roughly double that of down quarks. However, at very small  $x$  values, the sea quarks and gluons dominate, surpassing the contribution of the valence quarks.

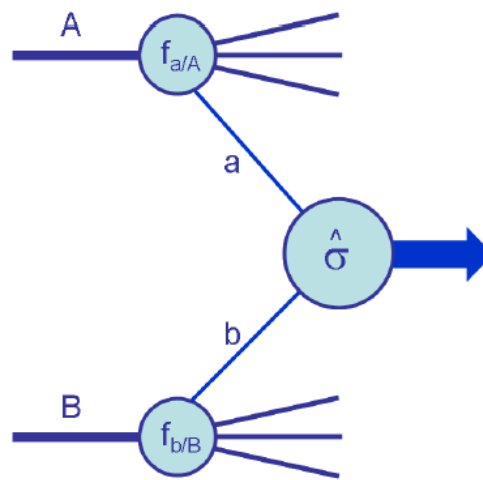


Figure 1.4: Schematic structure of a generic hard-scattering process.

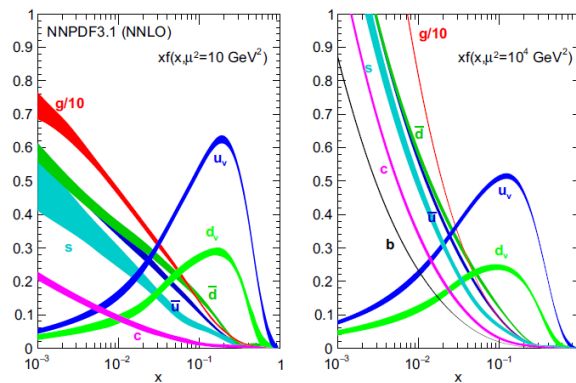


Figure 1.5: The gluon and valence PDFs obtained by the NNPDF collaboration including measurements performed at several collider experiments (D0, LHCb, ATLAS, CMS) [10]

### 1.4.2 $WZ$ Diboson Production

At the LHC various studies are conducted on diboson events, including  $WW$ ,  $WZ$ ,  $ZZ$ ,  $W\gamma$ ,  $Z\gamma$  and  $\gamma\gamma$  [9]. This thesis will focus on measurements of heavy vector bosons, with a particular focus on the  $WZ$  diboson system. Figure 1.6 represents the leading order (LO) Feynman diagrams of diboson production from quark-antiquark interaction.

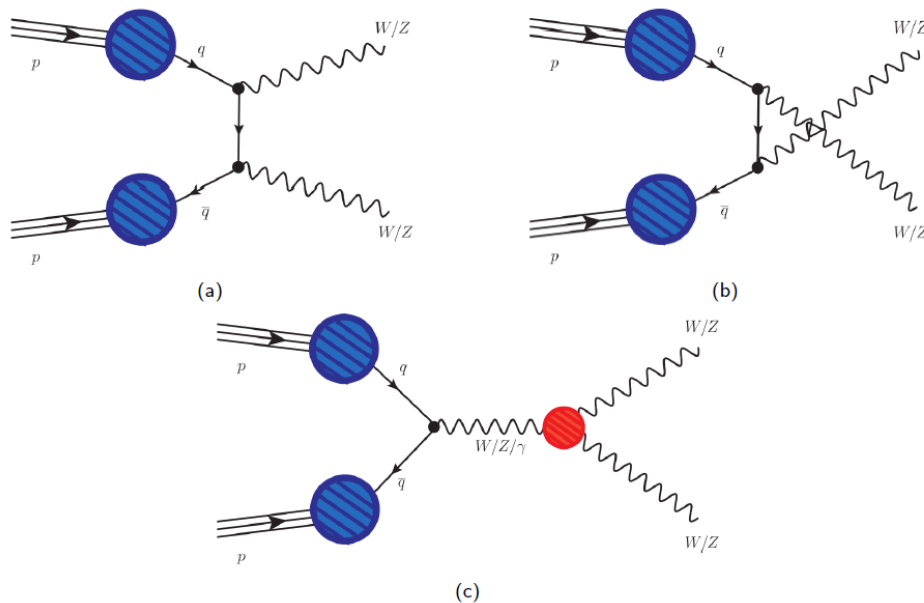


Figure 1.6: Leading order Feynman diagrams for diboson production at the LHC. The red dot indicates the triple gauge coupling vertex.

The diboson production cross-sections were measured in proton-proton collisions at a centre of mass energy of 13 TeV at LHC by ATLAS during Run 2, obtaining the results shown in Table 1.2.

Cross Section	Predicted	LHC
	( $pp$ , 13 TeV, [pb])	( $pp$ , 13 TeV, [pb])
WW	$128 \pm 3.5$	$142 \pm 5(\text{stat}) \pm 13(\text{syst}) \pm 3(\text{lumi})$
WZ	$49.1 \pm 1.0$	$51.0 \pm 0.8(\text{stat}) \pm 1.8(\text{exp. syst}) \pm 1.1(\text{lum.})$
ZZ	$15.7 \pm 0.7$	$17.8 \pm 1.0(\text{stat}) \pm 0.7(\text{syst}) \pm 0.4(\text{lumi})$

Table 1.2: Summary of cross-sections for  $WW$ ,  $WZ$  and  $ZZ$  at ATLAS at  $\sqrt{s} = 13$  TeV and their theoretical predictions [13] [12] [14].

The  $WZ$  diboson, as illustrated in Figure 1.6 can be produced by  $pp$  collisions in pairs through three channels: the  $t$ -channel (a), the  $u$ -channel (b) and  $s$ -channel (c). In

the  $s$ -channel, an off-shell  $W$  boson is created from the annihilation of a quark-antiquark pair, which decays into an on-shell  $W$  and  $Z$  boson through an interaction vertex.

At the LHC, there is a disparity in the production rates of  $W^+Z$  and  $W^-Z$  dibosons. This difference arises because the probability of finding a valence  $u$ -quark, compared to a  $d$ -quark is doubled in the proton, as shown in Figure 1.5. As a result, the production rate for  $W^+Z$  is higher compared to  $W^-Z$  as shown in Figure 1.8a.

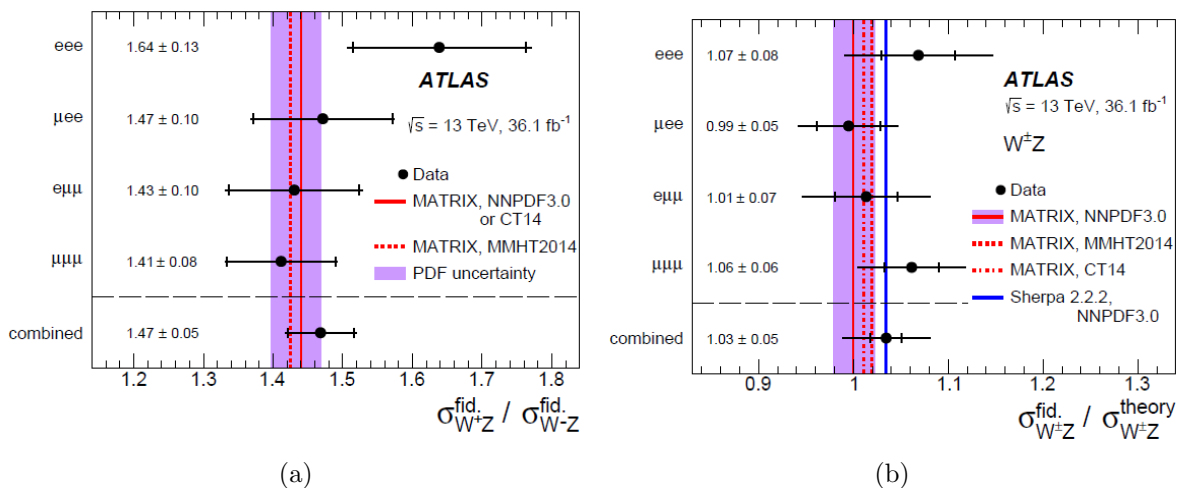


Figure 1.7: (a) Measured ratios of  $W^+Z$  and  $W^-Z$  integrated cross-sections in the fiducial phase space for all four channels. (b) Ratio of the measured  $W^\pm Z$  integrated cross sections in the fiducial phase space to the NLO SM prediction in each of the four channels and for their combination [12].

These particles have a very short lifetime, thus they decay before the interaction with the detector can happen. There are three possible decay channels for the  $WZ$  state: the pure hadronic channel, the one with the highest branching ratio, where both  $W$  and  $Z$  bosons decay into quarks, which then hadronize to produce jets; the semileptonic channel where a boson decay in hadrons and the other in leptons and neutrino; the pure leptonic decay channel in which bosons decay fully into four leptons. In this thesis, the focus will be on pure leptonic decay channels, in particular, the process considered will be  $W^\pm Z \rightarrow l'^\pm \nu l^+ l^-$ , in which the only leptons considered are electrons ( $e$ ) and muons ( $\mu$ ). This channel has the smallest branching ratio, but it is also easy to identify and distinguish from other background processes at LHC. Indeed, this is the channel selected for the precision diboson measurements at ATLAS and CMS. Figure 1.8 presents the measured distributions of the transverse momentum and the invariant mass of the  $Z$  candidate studied by ATLAS Collaboration in the measurement of the  $W^\pm Z$  production cross-section [12]. These distributions indicate that the background of other processes is minimal compared to the signal when analyzing the fully leptonic decay of the  $WZ$  system.

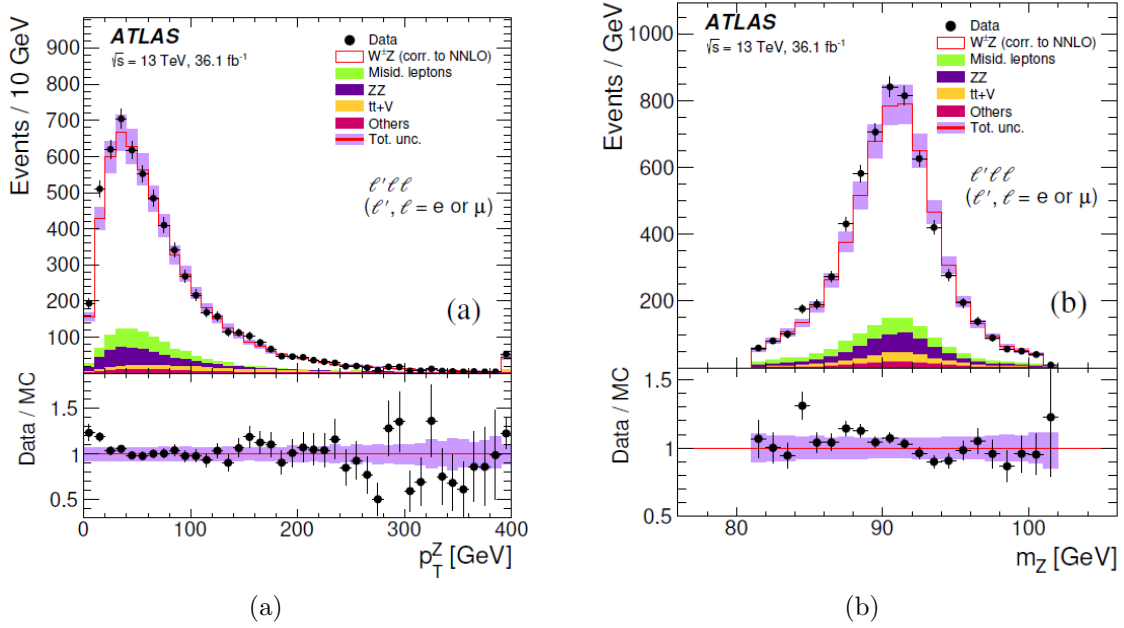


Figure 1.8: The distributions, for the sum of all channels, of the transverse momentum and the invariant mass of the  $Z$  boson. The points correspond to the data with the error bars representing the statistical uncertainties, and the histograms correspond to the predictions of the various SM processes.[12]

The fiducial cross-section of  $W^\pm Z$  and decay into pure leptonic channel considering all the four possible processes is

$$\sigma_{W^\pm Z \rightarrow l'^\pm \nu l^-}^{\text{fid.}} = 63.7 \pm 1.0 \text{ (stat)} \pm 2.3 \text{ (exp. sys)} \pm 0.3 \text{ (mod. sys)} \pm 1.4 \text{ (lumi)} \text{ fb} \quad (1.34)$$

which, in Figure 1.8b is compared to the theoretical cross-section of the Standard Model computed at next-to-leading order (NLO).

# Chapter 2

## Quantum Information

Quantum mechanics is a fundamental physics theory that outlines nature's behaviour at atomic and subatomic scales. While classical physics successfully describes many macroscopic phenomena, it fails to accurately explain systems at the microscopic scales of atoms and subatomic particles. In contrast, quantum mechanics offers a comprehensive framework for comprehending these systems. Quantum information refers to the information held in the state of a quantum system, extending the concept of classical information. This chapter will outline the main characteristics of quantum mechanics with an introduction to quantum information concepts.

### 2.1 Postulates of Quantum Mechanics

#### Postulate 1: State of a quantum system

Every isolated physical system is associated with a complex vector space with an inner product, known as a Hilbert space, which serves as the state space of the system. The system is completely described by its state vector (ray), which is a unit vector in the system's state space. The Hilbert space is a vector space over the complex numbers  $\mathbb{C}$  with an inner product  $\langle\psi|\phi\rangle$ , with  $|\psi\rangle$  and  $|\phi\rangle$  vectors in the inner product space. The product has the following properties [26]:

- Positivity:  $\langle\psi|\psi\rangle > 0$  for  $|\psi\rangle \neq 0$ .
- Linearity:  $\langle\psi|(a|\psi_1\rangle + b|\psi_2\rangle)\rangle = a\langle\psi|\psi_1\rangle + b\langle\psi|\psi_2\rangle$ .
- Skew symmetry:  $\langle\psi|\phi\rangle = \langle\phi|\psi\rangle^*$ .

Given two states,  $|\psi_1\rangle$  and  $|\psi_2\rangle$ , another state can be constructed as the linear superposition of the two,  $|\psi\rangle = a|\psi_1\rangle + b|\psi_2\rangle$ , which is also an admissible description of the quantum state under consideration.

## Postulate 2: Observables

An observable is a property of a physical system that can, in principle, be measured. In quantum mechanics, an observable is represented by a self-adjoint operator. An operator is a linear map that takes vector to vector, defined as

$$A : |\psi\rangle \rightarrow A|\psi\rangle, \quad A(a|\psi_1\rangle + b|\psi_2\rangle) \rightarrow aA|\psi_1\rangle + bA|\psi_2\rangle. \quad (2.1)$$

The operator  $A$  is self-adjoint if  $A = A^\dagger$ , which means that  $\langle\phi|A|\psi\rangle = \langle\psi|A|\phi\rangle^*$ . In a Hilbert space  $\mathcal{H}$ , a self-adjoint operator can be written in a spectral representation as follows

$$A = \sum_n a_n E_n \quad \text{with} \quad a_n \in \mathbb{R}, \quad (2.2)$$

where each  $a_n$  is an eigenvalue of  $A$  and  $E_n$  is the corresponding orthogonal projection onto the space of eigenvectors with eigenvalue  $a_n$ . The orthogonal projections satisfy the following properties

$$\begin{aligned} E_n E_m &= \delta_{n,m} E_n, \\ E_n^\dagger &= E_n \end{aligned} \quad (2.3)$$

The orthogonal projector onto the one-dimensional space spanned by the vector  $|\psi\rangle$  can be expressed as  $|\psi\rangle\langle\psi|$ . An alternative notation for the spectral representation of  $A$  is defined as

$$A = \sum_n a_n |n\rangle\langle n| \quad (2.4)$$

in which  $|n\rangle$  is the orthonormal basis of the eigenstates of  $A$ , with  $A|n\rangle = a_n|n\rangle$ .

## Postulate 3: Quantum Measurement

A measurement is a process in which an observer acquires information about the state of a physical system. Quantum measurements are described by a set of measurement operators denoted as  $M_m$  [25]. These are operators acting on the state space of the system being measured. The index  $m$  corresponds to the possible outcomes of the measurement. If the quantum system is in the state  $|\psi\rangle$  just before the measurement, the probability of obtaining the outcome  $m$  is given by

$$p(m) = \langle\psi|M_m^\dagger M_m|\psi\rangle. \quad (2.5)$$

After the measurement, the quantum state will be in the form:

$$|\psi^{PM}\rangle = \frac{M_m\psi}{\sqrt{\langle\psi|M_m^\dagger M_m|\psi\rangle}} \quad (2.6)$$

The measurement operator satisfies the completeness equation written as

$$\sum_m = M_m^\dagger M_m = I. \quad (2.7)$$

This equation is linked to the fact that the probabilities of the possible results sum up to one

$$1 = \sum_m p(m) = \sum_m \langle \psi | M_m^\dagger M_m | \psi \rangle. \quad (2.8)$$

A specific type of measurement, known as a projective measurement, is a special case of the general measurement process. A projective measurement is defined by an observable  $M$ , which is a Hermitian operator acting on the state space of the system being measured. The observable  $M$  can be expressed through its spectral decomposition as follows:

$$M = \sum_m m P_m, \quad (2.9)$$

where  $P_m$  is the projector onto the eigenspace of  $M$  with eigenvalue  $m$ . The possible outcomes of the measurement correspond to the eigenvalues  $m$  of the observables. The probability of obtaining the result  $m$  when measuring the state  $|\psi\rangle$  is given by

$$p(m) = \langle \psi | P_m | \psi \rangle. \quad (2.10)$$

The quantum state immediately after the measurement with outcome  $m$ , will take the form

$$|\psi^{PM}\rangle = \frac{P_m \psi}{\sqrt{p(m)}}. \quad (2.11)$$

One property of the projective measurement is related to the calculation of the expectation value of the outcomes. In particular, consider many identically prepared systems that have been measured, each described by the quantum state  $|\psi\rangle$ , the expectation value of the outcomes is defined as

$$\langle M \rangle \equiv \sum_n m p(m) = \sum_n m \langle \psi | P_m | \psi \rangle = \langle \psi | M | \psi \rangle. \quad (2.12)$$

## Postulate 4: Evolution

The evolution of a quantum state is described by a unitary transformation, which means that the state  $|\psi(t)\rangle$  of the system at time  $t$  is related to the state  $|\psi(t')\rangle$  of the system at the time  $t'$  by a unitary operator  $U$  which depends only on the times  $t'$  and  $t$  as follows

$$|\psi(t')\rangle = U(t', t) |\psi(t)\rangle \quad (2.13)$$

where  $U(t', t)$  is the unitary time evolution operator. The time evolution of a quantum state of a closed system is described by the Schrödinger equation

$$i\hbar \frac{d}{dt} |\psi\rangle = H |\psi\rangle \quad (2.14)$$

where  $H$  is a fixed Hermitian operator also known as the Hamiltonian of the closed system. If the Hamiltonian  $H$  is time independent, the evolution operator  $U(t', t)$  may be written as

$$U(t', t) = \exp \left[ \frac{-iH(t' - t)}{\hbar} \right] \quad (2.15)$$

## Postulate 5: Composite Systems

The state space of a composite physical system is the tensor product of the state spaces of the component physical systems. In particular, given the Hilbert space of the system  $A$  is  $\mathcal{H}_A$  and the Hilbert space of the system  $B$  is  $\mathcal{H}_B$ , the Hilbert space of the composite system  $AB$  will be  $\mathcal{H}_A \otimes \mathcal{H}_B$ . Let's consider  $|i\rangle_A$  as the orthonormal basis for the space  $\mathcal{H}_A$  and  $|\mu\rangle_B$  a basis for  $\mathcal{H}_B$ , then the states  $|i, \mu\rangle_{AB} \equiv |i\rangle_A \otimes |\mu\rangle_B$  constitute a basis for the space  $\mathcal{H}_A \otimes \mathcal{H}_B$ , where the inner product can be defined as follows

$${}_{AB}\langle i, \mu | j, \nu \rangle_{AB} = \delta_{ij} \delta_{\mu\nu} \quad (2.16)$$

An operator that acts only on one subsystem can be extended to the composite system by taking the tensor product with the identity operator on the other subsystem. For example, suppose  $O_A$  is an operator defined on the space  $\mathcal{H}_A$ . In that case, the corresponding operator on the composite system is defined as  $O_A \otimes I_B$ , where  $I_B$  is the identity operator on  $\mathcal{H}_B$ , and it acts as follows:

$$(O_A \otimes I_B)(|i\rangle_A \otimes |\mu\rangle_B) = O_A |i\rangle_A \otimes |\mu\rangle_B. \quad (2.17)$$

## 2.2 The Qubit

The fundamental concept of classical computation and classical information is the bit, which can take one of the two possible values 0,1. In quantum computing and quantum information, the corresponding unit is called "quantum bit", or qubit and describes a state in the simplest possible quantum system. As a classical bit has a state, i.e. 0 or 1, the two possible states for a qubit are the states  $|0\rangle$  and  $|1\rangle$ . Let's consider the smallest nontrivial Hilbert space which has two dimensions, then the most general normalized state can be written as

$$|\psi\rangle = a |0\rangle + b |1\rangle \quad (2.18)$$

where  $a$  and  $b$  are complex numbers that satisfy the property  $|a|^2 + |b|^2 = 1$ . Thus, a qubit is a quantum state described by a two-dimensional Hilbert space as shown in

Eq.(2.18). The primary distinction between qubits and classical bits is that a qubit can be written as a linear combination of the states  $|0\rangle$  and  $|1\rangle$ . If a measurement is performed projecting the qubit onto the basis  $|0\rangle, |1\rangle$ , then the outcome  $|0\rangle$  will be obtained with a probability  $|a|^2$  while the outcome  $|1\rangle$  with a probability  $|b|^2$ . Another key difference between classical and quantum bits involves the measurement of the state. Measuring a qubit alters its initial state, causing it to collapse from its superposition, as illustrated in Eq.(2.18), to a specific state.

A more intuitive way to represent the simple qubit is through the Bloch sphere, which can be used since  $|a|^2 + |b|^2 = 1$  holds for a qubit. Therefore, a qubit can be represented as the surface of a sphere with radius one, as described in Figure 2.1.

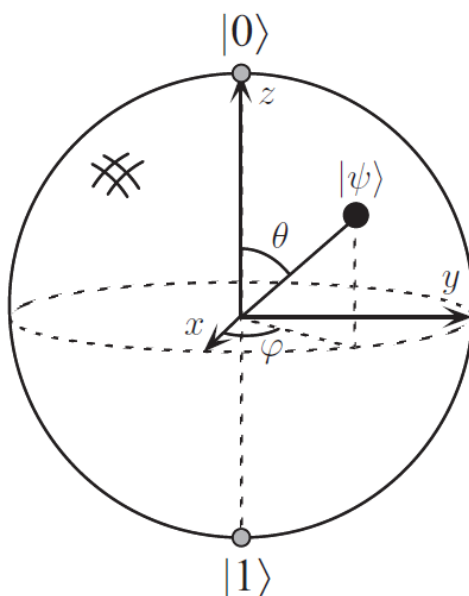


Figure 2.1: Bloch sphere representation of a qubit.

The qubit can then be written as follows

$$|\psi\rangle = \cos \frac{\theta}{2} |0\rangle + e^{i\phi} \sin \frac{\theta}{2} |1\rangle \quad (2.19)$$

where  $\theta$  and  $\phi$  are real numbers and define a point on the unit three-dimensional sphere. A qubit is a mathematical object that can be represented physically in various forms, some of which are utilized in quantum computers and other different fields of interest, such as quantum cryptography [2]. Another possible representation involves particles with spin  $s = 1/2$ . Since the spin projection for these particles has two possible states, they can be effectively treated as qubits. Let's consider the case in which there are two qubits. In the classical case of two bits, there would be four possible states, 00, 01, 10 and

11. Similarly, a pair of qubits has four computational states, i.e.  $|00\rangle$ ,  $|01\rangle$ ,  $|10\rangle$  and  $|11\rangle$ . Thus, the state vector describing the two qubits can be written as

$$|\psi\rangle = \alpha_{00}|00\rangle + \alpha_{01}|01\rangle + \alpha_{10}|10\rangle + \alpha_{11}|11\rangle \quad (2.20)$$

where the normalization condition is given by  $\sum_{x,y \in \{0,1\}} |a_{xy}|^2 = 1$ . The probability of observing the quantum state in one of the possible states, for example,  $|00\rangle$ , is given by  $|a_{00}|^2$ . Suppose now measuring the first qubit alone which gives  $|0\rangle$ , the post-measurement state will be

$$|\psi'\rangle = \frac{\alpha_{00}|00\rangle + \alpha_{01}|01\rangle}{\sqrt{|a_{00}|^2 + |a_{01}|^2}} \quad (2.21)$$

A specific set of two-qubit states obtained for particular values of  $\alpha_{xy}$  is known as the *Bell state* or *EPR pair*, defined as:

$$\begin{aligned} |\psi\rangle &= \frac{|00\rangle + |11\rangle}{\sqrt{2}} \\ |\psi\rangle &= \frac{|01\rangle + |10\rangle}{\sqrt{2}} \\ |\psi\rangle &= \frac{|00\rangle - |11\rangle}{\sqrt{2}} \\ |\psi\rangle &= \frac{|01\rangle - |10\rangle}{\sqrt{2}} \end{aligned} \quad (2.22)$$

These states exhibit a characteristic where measuring the first qubit one obtains two possible results: 0 with probability  $1/2$ , leaving the post-measurement state  $|\phi'\rangle = |00\rangle$ , and 1 with the same probability, leading to the state  $|\phi'\rangle = |11\rangle$ . Therefore, a measurement of the second qubit will always give the same result as the measurement of the first qubit, meaning that the outcomes are correlated. This property defines the two qubits as maximally entangled (a concept that will be explained later in this chapter).

## 2.3 The Density operator

The density matrix is an important mathematical tool in quantum mechanics, particularly for describing mixed states and statistical ensembles. Let's consider a quantum state is in one of a number of states  $|\psi_i\rangle$ , where  $i$  is an index, with respective probabilities  $p_i$  and  $\{p_i, |\psi_i\rangle\}$  is defined as the ensemble of pure states. Then, the density operator for the system is defined as

$$\rho \equiv \sum_i p_i |\psi_i\rangle \langle \psi_i| \quad (2.23)$$

which is also usually called the *density matrix* of a system. The density operators are characterized by the following properties:

- $\rho = \rho^\dagger$ , which means the density operator is Hermitian,
- The trace of the density operator is equal to one,  $\text{tr}(\rho) = 1$ ,
- $\rho$  is a positive operator, meaning that for any  $|\psi_i\rangle$  in the space  $\langle\psi|\rho|\psi\rangle \geq 0$

Suppose the evolution of a closed state is described by a unitary operator  $U$ , then the system evolves to  $U|\psi_i\rangle$ , where  $|\psi_i\rangle$  is the initial state with probability  $p_i$ . Therefore, the evolution operator can be described by the equation

$$\rho = \sum_i p_i |\psi_i\rangle \langle\psi_i| \xrightarrow{U} \sum_i p_i U |\psi_i\rangle \langle\psi_i| U^\dagger = U \rho U^\dagger. \quad (2.24)$$

Consider performing a measurement described by the operator  $M_m$ , then it is possible to use the density operator to describe it. If the initial state considered is  $|\psi_i\rangle$ , the probability of obtaining the result  $m$  is

$$p(m) = \sum_i p(m|i)p_i, \quad (2.25)$$

where the term  $p(m|i)$  can be written as

$$p(m|i) = \langle\psi_i|M_m^\dagger M_m|\psi_i\rangle = \text{tr}(M_m^\dagger M_m |\psi_i\rangle \langle\psi_i|). \quad (2.26)$$

Thus, the probability of getting result  $m$  can be written using Eq.(2.26) as

$$p(m) = \sum_i p_i \text{tr}(M_m^\dagger M_m |\psi_i\rangle \langle\psi_i|) = \text{tr}(M_m^\dagger M_m \rho) \quad (2.27)$$

After performing the measurement, the initial state  $|\psi_i\rangle$  becomes

$$|\psi_i^m\rangle = \frac{M_m |\psi_i\rangle}{\sqrt{\langle\psi_i|M_m^\dagger M_m|\psi_i\rangle}} \quad (2.28)$$

The corresponding density operator  $\rho_m$  post-measurement is described by

$$\rho_m = \sum_i p(i|m) |\psi_i^m\rangle \langle\psi_i^m| = \sum_i p_i \frac{M_m |\psi_i^m\rangle \langle\psi_i^m| M_m^\dagger}{\langle\psi_i|M_m^\dagger M_m|\psi_i\rangle} = \frac{M_m \rho M_m^\dagger}{\text{tr}(M_m^\dagger M_m \rho)} \quad (2.29)$$

in which it has been used the probability theory,  $p(i|m) = p(m|i)p_i/p(m)$  and the Eqs.(2.26-2.27) have been substituted. Let's now introduce a feature of quantum states related to the density operator. It is possible to distinguish between two types of quantum state as follows

- *Pure state*: a state  $|\psi\rangle$  in a quantum state is considered pure if it is known exactly. For a pure state, the density operator is simply  $\rho = |\psi\rangle\langle\psi|$  and it must be satisfied the condition  $\text{tr}(\rho^2) = 1$ .
- *Mixed state*: a state  $|\psi\rangle$  is said to be mixed if it is a mixture of different pure states in the ensemble of  $\rho$ . In this case, the mixed state satisfies the condition  $\text{tr}(\rho^2) < 1$ .

One of the density operator's more interesting applications is describing subsystems of a composite quantum system. Suppose to consider two physical systems  $A$  and  $B$ , whose state is represented by a density operator  $\rho^{AB}$ . The partial system  $A$  can be described by the reduced density operator defined as follows

$$\rho^A \equiv \text{tr}_B(\rho^{AB}), \quad (2.30)$$

where  $\text{tr}_B$  is a map of operators known as the partial trace over the system  $B$  and it is defined as

$$\text{tr}_B(|a_1\rangle\langle a_2| \otimes |b_1\rangle\langle b_2|) \equiv |a_1\rangle\langle a_2| \text{tr}(|b_1\rangle\langle b_2|), \quad (2.31)$$

in which  $|a_i\rangle$  are two vectors in state  $A$ , and  $|b_i\rangle$  belong to space state  $B$ . It may not be immediately clear that the reduced density operator for system  $A$  accurately describes its state. The physical explanation for this identification is that the reduced density operator provides the correct measurement statistics for observations made on system  $A$ . Consider a quantum system in the state  $\rho^{AB} = \rho \otimes \sigma$ , where  $\rho$  is the density for the system  $A$  and  $\sigma$  is the density operator for system  $B$ . Thus, the reduced density operator for state  $A$  can be written as

$$\rho^A = \text{tr}_B(\rho \otimes \sigma) = \rho \text{tr}(\sigma) = \rho. \quad (2.32)$$

For the state  $B$ , the result obtained is  $\rho^B = \sigma$ . The density operator in the case of Bell state  $(|00\rangle + |11\rangle)/\sqrt{2}$  can be defined as

$$\rho = \left( \frac{|00\rangle + |11\rangle}{\sqrt{2}} \right) \left( \frac{\langle 00| + \langle 11|}{\sqrt{2}} \right). \quad (2.33)$$

By tracing out the second qubit, the reduced density matrix of the first qubit becomes

$$\rho^1 = \text{tr}_2(\rho) = \frac{|0\rangle\langle 0| + |1\rangle\langle 1|}{2} = \frac{I}{2}. \quad (2.34)$$

An important consideration can be extrapolated from this result: the state in Eq.(2.34) is a mixed state, as evidenced by  $\text{tr}((I/2)^2) = 1/2 < 1$ . The state of the joint system of two qubits is a pure state, meaning it is known exactly. However, the first qubit is a mixed state, indicating incomplete knowledge about it. This peculiar property, where the joint state of a system is completely known while a subsystem is in a mixed state, is a defining feature of entanglement.

## 2.4 Entanglement

The density operator in a bipartite system can be expressed in a particularly useful form known as the *Schmidt decomposition*. Let's consider a pure state  $|\psi\rangle$  of a composite system  $AB$ . Then, there exist orthonormal states  $|i_A\rangle$  for system  $A$  and orthonormal states  $|i_B\rangle$  of system  $B$  such that

$$|\psi\rangle = \sum_i \lambda_i |i_A\rangle |i_B\rangle, \quad (2.35)$$

where the coefficients  $\lambda_i$  are real non-negative numbers known as *Schmidt coefficients*, which satisfies the property  $\sum_i \lambda_i^2 = 1$ . From Eq.(2.35), the reduced density operator for the substates can be written as

$$\rho^A = \sum_i \lambda_i^2 |i_A\rangle \langle i_A| \quad \rho^B = \sum_i \lambda_i^2 |i_B\rangle \langle i_B| \quad (2.36)$$

where it can be seen that the eigenvalues of  $\rho^A$  and  $\rho^B$  are identical for both density operators. These eigenvalues are fundamental in describing important properties of quantum systems, for example, for a pure state of a composite system such features will be the same for both subsystems. The states  $|i_A\rangle$  and  $|i_B\rangle$  in Eq.(2.35) are referred to as the Schmidt bases for subsystems  $A$  and  $B$  respectively. The number of non-zero values coefficients  $\lambda_i$  is known as the Schmidt number for the state  $|\psi\rangle$ , which is crucial because they quantify the "degree" of entanglement between the states  $A$  and  $B$ . Specifically, a bipartite pure state  $|\psi\rangle$  of a system  $AB$  is entangled if its Schmidt number is greater than one, otherwise it's said to be separable. In this case, a separable bipartite pure system can be expressed as a direct product of states in  $A$  and  $B$  subsystems,

$$|\psi\rangle = |u\rangle_A \otimes |v\rangle_B. \quad (2.37)$$

For such separable states, the reduced density matrices for the subsystems are  $\rho^A = |u\rangle \langle u|$  and  $\rho^B = |v\rangle \langle v|$ , indicating that both subsystems are in pure states. Thus, any state that cannot be expressed as a direct product is entangled. In such cases, the reduced density matrices for subsystems  $A$  and  $B$  are mixed states. In addition, if the state  $|\psi\rangle$  of the composite system  $AB$  is entangled, then the subsystem  $A$  and  $B$  are quantum correlated. This means that the quantum states of  $A$  and  $B$  are linked in such a way that the state of one subsystem cannot be fully described independently of the state of the other.

The entanglement is a fundamental property of a quantum system, however, the necessary and sufficient conditions to determine the entanglement of a mixed state are generally difficult to calculate. One condition for the observation of entanglement is the quantum observables called *concurrence* [23], in particular, a state can have non-zero concurrence only if it is entangled. For a mixed state, the concurrence  $c(\rho)$  can

be defined using the convex roof extension method. This approach involves determining a limit in terms of the different ensembles of states  $(p_i, |\psi\rangle)$  that could have led to the mixed state  $\rho$ . Therefore, the concurrence can be written as

$$c(\rho) = \inf \sum_i p_i c(|\psi\rangle), \quad \text{with} \quad \sum_i p_i = 1, \quad p_i \geq 0, \quad (2.38)$$

in which the infimum is taken over all the ensembles  $\{p_i, |\psi_i\rangle\}$  for which is valid  $\rho = \sum_i p_i |\psi_i\rangle \langle \psi_i|$ . In the case of a bipartite system of a pair of qubits, the concurrence can be calculated analytically, while for systems with dimensions greater than  $d = 2 \times 3$  only a lower bound can be computed as will be shown in Chapter 3.

The entanglement is also fundamental in describing the difference between classical and quantum physics. Let's consider the concept of measurement: in classical physics, a measurement is simply the observation of a property that an object possesses, regardless of how the measurement is obtained. In quantum mechanics, however, an unobserved object, such as a particle, does not possess physical properties that exist independently of observation. Instead, these physical properties emerge from measurements made on the system. For instance, a qubit does not have defined properties of spin along the  $z$ -direction and the  $x$ -direction, but given the state vector, quantum mechanics specifies the probabilities of the possible measurement outcomes for these observables. This counterintuitive behaviour of quantum mechanics generated several doubts among physicists of that time. One of the greatest objectors of this theory was Albert Einstein. In 1935, along with Nathan Rosen and Boris Podolsky, he published a famous paper describing a thought experiment known as the EPR paradox [21]. Their main argument was that quantum mechanics is not a complete theory of Nature, because it is possible to identify elements of reality that were not included in quantum mechanics.

To explain the EPR paradox, consider a pair of two particles  $A$  and  $B$  with spin  $s = 1/2$  emitted by a particle with spin zero, which is equivalent to considering an entangled pair of qubits. The particles are then separated and given to two observers, namely Alice and Bob who are at a distance such that Alice cannot modify the outcome of the experiments performed by Bob and vice versa. In this setup, if Alice measures  $\sigma_z$ , then by quantum mechanics the value of  $\sigma_z$  for Bob's measurement is known with certainty. The same reasoning can be made for the measurement of  $\sigma_x$ , thus both physical properties must correspond to an element of reality following the EPR criterion. However, this conclusion is in contrast to what has been described earlier, since quantum mechanics only explains how to calculate the probabilities of respective measurement outcomes if the observable is measured. Thus, the three authors concluded that quantum mechanics cannot be a complete theory and to solve this problem they suggested the existence of some other degrees of freedom, known as hidden variables which account for the behavior of entangled particles. In a hidden-variable theory, measurement is fundamentally deterministic but appears to be probabilistic because some degrees of freedom

are not precisely known. Let's consider a particle with a spin of one-half quantized along  $n$ -direction. The state which describes the particle with spin  $s = 1/2$  along  $z$ -direction can be written as

$$|\uparrow_z\rangle = \cos \frac{\theta}{2} |\uparrow_n\rangle + \sin \frac{\theta}{2} |\downarrow_n\rangle \quad (2.39)$$

Using hidden variables theory, there is an additional variable  $\lambda$  that nobody can control, thus it can take any value between zero and one. Now suppose the spin is measured along the axis  $n$ , the outcome can be described by

$$\begin{aligned} |\uparrow_n\rangle, & \quad \text{for } 0 \leq \lambda \leq \cos^2 \frac{\theta}{2} \\ |\downarrow_n\rangle, & \quad \text{for } \cos^2 \frac{\theta}{2} \leq \lambda \leq 1 \end{aligned} \quad (2.40)$$

It is obvious that if  $\lambda$  is known, the outcome is completely deterministic, while if  $\lambda$  is unknown, the probability distribution governing the measurement will align with the predictions of quantum theory. Let's now consider an experiment that recalls the theorem proposed by John Bell in 1964, which assumes the hidden variables theory. Suppose Charlie, an observer, prepares two particles and gives one particle to Alice and the other to Bob. Alice can perform two distinct experiments on the particle she receives, designed to measure two different properties  $Q$  and  $R$ . The outcomes of each experiment are denoted as  $q$  and  $r$ , and these values are restricted to  $+1$  or  $-1$ . Similarly, Bob can measure the two properties  $S$  and  $T$ , with outcomes  $s$  and  $t$ , with values still limited to  $+1$  or  $-1$ . The experiment is schematically represented in Figure 2.2. Now define the



Figure 2.2: Schematic representation of the experiment for Bell inequalities

combination of measurements  $QS + RS + RT - QT$ , it can be rewritten as

$$QS + RS + RT - QT = (Q + R)S + (R - Q)T \quad (2.41)$$

Because both  $Q$  and  $R$  take values  $\pm 1$ , then either  $Q = R$  or  $Q = -R$ . In the first case  $(R - Q)T = 0$ , while in the second  $(Q + R)S = 0$ . Therefore in both situations, it can be noticed that  $QS + RS + RT - QT = \pm 2$ . The probability that, before the measurements by Alice and Bob are performed, the system is in the state where  $Q = q$ ,  $R = r$ ,  $S = s$  and  $T = t$  can be defined as  $p(q, r, s, t)$ .

Now the expectation value of combinations of experiments is

$$\begin{aligned}
 B &= E(QS) + E(RS) + E(RT) - E(QT) \\
 &= E(QS + RS + RT - QT) \\
 &= \sum_{qrst} p(q, r, s, t)(qs + rs + rt - qt) \\
 &\leq 2
 \end{aligned} \tag{2.42}$$

where in the last part the property defined above has been used. This formula is called *CHSH inequality* and belongs to a class of inequalities known as Bell inequalities. Now the experiment is repeated considering that the two particles have spin  $s = 1/2$  prepared in a Bell state, and the expectation values of measurements are computed using quantum mechanics formulation. Therefore, Alice and Bob measure the following observables:

$$\begin{aligned}
 Q &= \sigma_z & S &= -\frac{\sigma_z + \sigma_x}{\sqrt{2}} \\
 R &= \sigma_x & T &= \frac{\sigma_z - \sigma_x}{\sqrt{2}}.
 \end{aligned} \tag{2.43}$$

where  $\sigma_x$  and  $\sigma_z$  are two of the Pauli matrices. As before, the outcome of all four experiments can be +1 or -1. Thus, the value of  $B$  using quantum mechanics formalism can be written as

$$\begin{aligned}
 B &= \langle QS \rangle + \langle RS \rangle + \langle RT \rangle - \langle QT \rangle \\
 &= \frac{1}{\sqrt{2}} + \frac{1}{\sqrt{2}} + \frac{1}{\sqrt{2}} - \left( -\frac{1}{\sqrt{2}} \right) = 2\sqrt{2}.
 \end{aligned} \tag{2.44}$$

This result is in contradiction with Eq.(2.42) where it was obtained that the average of all possible combinations of experiments could not exceed 2. This provides a mathematical framework for a setup that can be used to test how Nature behaves. Over the years, numerous experiments have been carried out to test Bell's inequality across various systems. One such experiment, which demonstrated that Nature violates Bell's inequality following quantum mechanics, was recognized with the Nobel Prize in 2022. In Eq.(2.42), there must be some assumptions that are not fully correct. In particular, two hypotheses are questionable:

- The assumption that the physical properties Q, R, S, and T have definite values which exist independently of observation. This concept is known as *realism*.
- The supposition that, for example, Alice performing the measurement does not influence the result obtained by Bob and vice versa.

These two assumptions together are known as local realism. As previously mentioned, Bell inequality experiments demonstrate that at least one of these assumptions is incorrect. It's important to note that not every quantum state leads to a violation of Bell's inequalities. For instance, in the case of a separable pure state, the Bell inequality is respected. Therefore, while a system must be in an entangled state to violate Bell's inequalities, entanglement alone is not sufficient for such a violation. Additionally, in experiments like those of Alice and Bob, the violation of Bell's inequality depends on the choice of measurement axes and the fact that the observables measured must not commute. The entanglement therefore is a new fundamental resource with deep implications both in fundamental physics and practical application, for example in quantum computing. In this thesis, an application of entanglement will be presented to study fundamental Standard Model particles, in particular, bosons, which can be considered as qutrits, which will be discussed in the next chapter.

# Chapter 3

## Quantum State Tomography and Qutrit Formalism

The density matrix is fundamental in quantum mechanics, as it provides a complete description of the quantum system under consideration. The determination of the density matrix from an ensemble of measurements is known as "Quantum State Tomography" (QST). This chapter will describe how to obtain the spin density matrix for a multiparticle system, in particular for a bipartite system of particles with spin  $s = 1$  and how the spin state of these particles can be described using the *qutrit* formalism. In this thesis, the focus will be mainly on systems of two heavy vector bosons, with a detailed study of  $WZ$  diboson states. Additionally, the concept of concurrence will be introduced, along with its role in determining the entanglement of a bipartite system of particles.

### 3.1 Generalized Gell-Mann parameterizations

As explained in the previous chapter, the density matrix of a system describes the state of a quantum system, in particular, it is useful for dealing with mixed states, where the system may be in a probabilistic combination of different pure states. The density matrix is defined as

$$\rho = \sum_i p_i |\psi_i\rangle \langle \psi_i| \quad (3.1)$$

where  $p_i$  can be interpreted as a set of probabilities for the states  $|\psi\rangle$  within an ensemble. Let's now consider a particle with a spin  $s$  and write its spin density matrix  $\rho$ . The density operator will be Hermitian defined on the Hilbert space state with a dimension  $d = 2s + 1$  and with  $d^2 - 1$  real parameters, due to its properties. In the case of a multiparticle system, the Hilbert space where the density matrix is defined can be written as

$$\mathcal{H} = \mathcal{H}_1 \otimes \mathcal{H}_2 \otimes \cdots \otimes \mathcal{H}_n \quad (3.2)$$

that has a dimension  $d = (2s_1 + 1)(2s_2 + 1) \dots (2s_n + 1)$ , where  $s_i$  is the spin of each single particle. The parameters of the spin density matrix can be determined using quantum state tomography, a technique that involves reconstructing the density matrix from a series of measurements on an ensemble of identically prepared states. This approach is necessary because it is not possible to directly determine the spin of a particle during collisions at the LHC from the measurement of a single instance of the state. The key concept of quantum tomography is the relation between the spin of the particle and its direction, therefore studying the decay products is fundamental to reconstructing the spin of the original particle. The first step is finding a way to write the density matrix through a parameterization that can be determined experimentally. In this thesis, it has been used a parameterization based on the generalised  $d$ -dimensional Gell-Mann (GGM) operators  $\lambda^{(d)}$  [6]. These  $d^2 - 1$  matrices for a Hilbert space represent the generators for the group  $SU(d)$  and have the following properties:

$$\begin{aligned} [\lambda_i^{(d)}, \lambda_j^{(d)}] &= 2if_{ijk}\lambda_k^{(d)}, \\ \{\lambda_i^{(d)}, \lambda_j^{(d)}\} &= \frac{4}{d}\delta_{ij}I_d + 2g_{ijk}\lambda_k^{(d)} \end{aligned} \quad (3.3)$$

where  $f_{ijk}$  and  $g_{ijk}$  are the commutator and anticommutator structure constants and  $I_d$  is the  $d$ -dimensional identity matrix. The GGM matrices can be obtained by writing the generators in the standard basis:

- $\frac{d(d-1)}{2}$  symmetric matrices

$$\lambda_{jk}^{(d),S} = |j\rangle\langle k| + |k\rangle\langle j|, \quad 1 \leq j < k \leq d; \quad (3.4)$$

- $\frac{d(d-1)}{2}$  antisymmetric matrices

$$\lambda_{jk}^{(d),A} = -i|j\rangle\langle k| + i|k\rangle\langle j|, \quad 1 \leq j < k \leq d; \quad (3.5)$$

- $(d-1)$  diagonal matrices

$$\lambda_l^{(d),D} = \sqrt{\frac{2}{l(l+1)}} \left( \sum_{j=1}^l |j\rangle\langle j| - l|l+1\rangle\langle l+1| \right), \quad 1 \leq l \leq d-1. \quad (3.6)$$

Therefore, from this definition, the GGM matrices are Hermitian, traceless and orthogonal and satisfy the following relations:

$$\begin{aligned} \text{tr}(\lambda_j^{(d)}\lambda_k^{(d)}) &= 2\delta_{jk}, \\ \text{tr}(\lambda_j^{(d)}) &= 0, \end{aligned} \quad (3.7)$$

These properties make them an ideal basis for representing the density matrix. Now the operator  $\rho$  for a single particle with spin  $s$  can be expressed as

$$\rho^{(d)} = \frac{1}{d}I_d + \sum_{i=1}^{d^2-1} a_i \lambda_i^{(d)} \quad (3.8)$$

where  $d$  is the dimension of the Hilbert state and  $a_i$  are the real parameters that form the Bloch vector  $\vec{a} = (\{a_{jk}^S\}, \{a_{jk}^A\}, \{a_l^D\})$  with dimension  $d^2 - 1$ .

The case with spin  $s = 1$  is used in this thesis to describe  $W$  and  $Z$  bosons, where the Hilbert space of each particle has dimension  $d = 3$  and thus has 8 different real parameters [5]. For spin-1 particles the GGM matrices are

$$\begin{aligned} \lambda_1^{(3)} = \lambda_{12}^{(3),S} &= \begin{pmatrix} 0 & 1 & 0 \\ 1 & 0 & 0 \\ 0 & 0 & 0 \end{pmatrix}, & \lambda_2^{(3)} = \lambda_{12}^{(3),A} &= \begin{pmatrix} 0 & -i & 0 \\ i & 0 & 0 \\ 0 & 0 & 0 \end{pmatrix}, & \lambda_3^{(3)} = \lambda_1^{(3),D} &= \begin{pmatrix} 1 & 0 & 0 \\ 0 & -1 & 0 \\ 0 & 0 & 0 \end{pmatrix}, \\ \lambda_4^{(3)} = \lambda_{13}^{(3),S} &= \begin{pmatrix} 0 & 0 & 1 \\ 0 & 0 & 0 \\ 1 & 0 & 0 \end{pmatrix}, & \lambda_5^{(3)} = \lambda_{13}^{(3),A} &= \begin{pmatrix} 0 & 0 & -i \\ 0 & 0 & 0 \\ i & 0 & 0 \end{pmatrix}, & \lambda_6^{(3)} = \lambda_{23}^{(3),S} &= \begin{pmatrix} 0 & 0 & 0 \\ 0 & 0 & 1 \\ 0 & 1 & 0 \end{pmatrix}, \\ \lambda_7^{(3)} = \lambda_{23}^{(3),A} &= \begin{pmatrix} 0 & 0 & 0 \\ 0 & 0 & -i \\ 0 & i & 0 \end{pmatrix}, & \lambda_8^{(3)} = \lambda_2^{(3),D} &= \frac{1}{\sqrt{3}} \begin{pmatrix} 1 & 0 & 0 \\ 0 & 1 & 0 \\ 0 & 0 & -2 \end{pmatrix}. \end{aligned} \quad (3.9)$$

which are the generators of the group  $SU(3)$ . The corresponding spin density matrix for a qutrit can be written as

$$\begin{aligned} \rho^{(3)} &= \frac{1}{3}I_3 + \sum_{i=1}^8 a_i \lambda_i^{(3)} \\ &= \begin{pmatrix} \frac{1}{3} + a_3 + \frac{1}{\sqrt{3}}a_8 & a_1 - ia_2 & a_4 - ia_5 \\ a_1 + ia_2 & \frac{1}{3} - a_3 + \frac{1}{\sqrt{3}}a_8 & a_6 - ia_7 \\ a_4 + ia_5 & a_6 + ia_7 & \frac{1}{3} - \frac{2}{\sqrt{3}}a_8 \end{pmatrix}. \end{aligned} \quad (3.10)$$

The coefficients  $a_i$  of the density operator can be determined by computing the expectation values of the corresponding operators. This follows from the relations involving the Gell-Mann matrices in Eq.(3.7). Therefore, the expectation values of the operators corresponding to the Gell-Mann matrices are obtained as follows

$$\langle \lambda_i^{(d)} \rangle = \text{tr}(\rho \lambda_i^{(d)}) = 2a_i. \quad (3.11)$$

Using the parameterization (3.8), a generalization can be made for a multi-particle system. In particular for a two-particle state of particles with spin  $s_1$  and  $s_2$ , the bipartite

density matrix can be defined as

$$\rho^{(d)} = \frac{1}{d} I_d + \sum_{i=1}^{d_1^2-1} a_i \lambda_i^{(d_1)} \otimes \frac{1}{d_2} I_{d_2} + \sum_{j=1}^{d_2^2-1} \frac{1}{d_1} I_{d_1} \otimes b_j \lambda_j^{(d_2)} + \sum_{i=1}^{d_1^2-1} \sum_{j=1}^{d_2^2-1} c_{ij} \lambda_i^{(d_1)} \otimes \lambda_j^{(d_2)} \quad (3.12)$$

where  $d_i = (2s_i + 1)$  is the dimension of the Hilbert space of each particle and  $d = d_1 d_2$  is the full Hilbert space. The parameters  $a_i$  and  $b_j$  are the Bloch vectors for the single particle, while the  $c_{ij}$  are the correlation parameters of the two particles. For the specific case that will be studied in this thesis of a diboson system, the spin density matrix of the state is defined as follows

$$\rho = \frac{1}{9} I_9 + \frac{1}{3} \sum_{i=1}^8 a_i \lambda_i \otimes I_3 + \frac{1}{3} \sum_{j=1}^8 b_j I_3 \otimes \lambda_j + \sum_{i=1}^8 \sum_{j=1}^8 c_{ij} \lambda_i \otimes \lambda_j \quad (3.13)$$

where the complete Hilbert space, which has a dimension of  $d = 9$ , is characterized by 80 parameters.

## 3.2 Weyl-Wigner formalism for spin-1 particle

As introduced in the previous section, the core idea behind quantum tomography lies in the relation between the spin of a particle and its direction. In particular, when studying spin-1 particles, such as  $W$  and  $Z$  bosons, the chiral nature of electroweak interaction plays a fundamental role. For example, the interaction between  $W$  boson and emitted leptons ensures that the direction of the charged lepton is correlated with its spin. This correlation makes the charged decay lepton a useful tool for reconstructing the spin of the original boson. Thus, analyzing the decay products is crucial for accurately reconstructing the spin of the original particle. From the theoretical perspective, the process where particles with a specific spin density matrix decay according to angular distributions can be described using analytical calculations or Monte Carlo simulations. However, the inverse process—using the angular distributions of decay products to determine the spin density matrix of the original particle—can be accomplished through the Weyl-Wigner transformation, which maps functions between the quantum space of angular distributions and the Hilbert space. The Wigner  $Q$  symbols are used to forward mapping from bounded operators  $A : \mathcal{H} \rightarrow \mathcal{H}$  in the Hilbert space  $\mathcal{H}$  of the spin states onto the space of functions on the sphere  $S^2$ . The Wigner  $Q$  symbols are defined as follows

$$\Phi_A^Q(\hat{\mathbf{n}}) = \langle \hat{\mathbf{n}} | A | \hat{\mathbf{n}} \rangle, \quad (3.14)$$

with  $\hat{\mathbf{n}}$  as a unit vector in  $\mathcal{R}^3$ . The inverse mapping is obtained through the Wigner  $P$  symbols which connect the space of functions on  $S^2$  to the operators  $A : \mathcal{H} \rightarrow \mathcal{H}$  using

the following definition

$$A = \frac{2j+1}{4\pi} \int d\Omega_{\hat{\mathbf{n}}} |\hat{\mathbf{n}}\rangle \Phi_A^P(\hat{\mathbf{n}}) \langle \hat{\mathbf{n}}|, \quad (3.15)$$

where the angular integral is over directions of unit vector  $\hat{\mathbf{n}}$ .

Let's now consider the specific case of the  $WZ$  diboson system decaying into the fully leptonic channel to determine the coefficients of the spin density matrix in Eq.(3.13). The  $W$  vector boson decays by coupling only to left-chiral spin-half fermions and right-chiral spin-half antifermions, resulting in maximal parity violation. Under the approximation  $m_l \ll m_W$ , the decay  $W^+ \rightarrow l^+ \nu$  produces a  $l^+$  with positive helicity and a  $\nu$  with negative helicity. Consequently, the spin of the  $W^+$  is effectively  $+1$  in the direction of the  $l^+$  momentum. The scenario is reversed for the  $W^-$  boson, with its spin being  $-1$  along the momentum direction of  $l^-$ . Therefore, measuring the decay direction of the outgoing leptons in the  $W^\pm$  boson rest frame is equivalent to projectively measuring the heavy vector-boson spin in that frame. In particular, the probability density function for a  $W^\pm$  boson is given (3.10) to emit a charged lepton  $l^\pm$  into infinitesimal solid angle  $d\Omega$  along the direction  $\hat{\mathbf{n}}(\theta, \phi)$  is given by

$$p(l_{\hat{\mathbf{n}}}^\pm; \rho) = \frac{d}{4\pi} \text{tr}(\rho \Pi_{\pm, \hat{\mathbf{n}}}), \quad (3.16)$$

where  $d = 3$  for the  $W^\pm$  bosons and the probability density function is defined such that

$$\int d\Omega_{\hat{\mathbf{n}}} p(l_{\hat{\mathbf{n}}}^\pm; \rho) = 1. \quad (3.17)$$

The spin-1 projection operator  $\Pi_{+, \hat{\mathbf{n}}} \equiv |+\rangle_{\hat{\mathbf{n}}} \langle +|_{\hat{\mathbf{n}}}$  selects a positive helicity  $l^+$  in the direction  $\hat{\mathbf{n}}$  with a negative helicity  $\nu$  in the direction  $-\hat{\mathbf{n}}$ . Similarly for  $\Pi_{-, \hat{\mathbf{n}}} \equiv |-\rangle_{\hat{\mathbf{n}}} \langle -|_{\hat{\mathbf{n}}}$ , a negative helicity  $l^-$  is selected in the direction  $\hat{\mathbf{n}}$  accompanied by a positive helicity  $\bar{\nu}$  in the direction  $-\hat{\mathbf{n}}$  for the  $W^-$  case. The full expression for the angular probability density function can be written in terms of the parameters of the Gell-Mann basis as

$$p(l_{\hat{\mathbf{n}}}^\pm; \rho) = \frac{3}{4\pi} \left( \frac{1}{3} + \sum_{i=1}^8 \Phi_i^{Q^\pm} a_i \right). \quad (3.18)$$

The eight functions  $\Phi_i^{Q^\pm}$  are the Wigner  $Q$  symbols for the Gell-Mann operators for the

$W^\pm$  bosons and each function, shown in Figure 3.1, is defined as

$$\begin{aligned}
 \Phi_1^{Q^\pm} &= \frac{1}{\sqrt{2}} \sin \theta (\cos \theta \pm 1) \cos \phi & \Phi_5^{Q^\pm} &= \frac{1}{2} \sin^2 \theta \sin 2\phi \\
 \Phi_2^{Q^\pm} &= \frac{1}{\sqrt{2}} \sin \theta (\cos \theta \pm 1) \sin \phi & \Phi_6^{Q^\pm} &= \frac{1}{\sqrt{2}} \sin \theta (-\cos \theta \pm 1) \cos \phi \\
 \Phi_3^{Q^\pm} &= \frac{1}{8} (\pm 4 \cos \theta + 3 \cos 2\theta + 1) & \Phi_7^{Q^\pm} &= \frac{1}{\sqrt{2}} \sin \theta (-\cos \theta \pm 1) \sin \phi \\
 \Phi_4^{Q^\pm} &= \frac{1}{2} \sin^2 \theta \cos 2\phi & \Phi_8^{Q^\pm} &= \frac{1}{8\sqrt{3}} (\pm 12 \cos \theta - 3 \cos 2\theta - 1).
 \end{aligned} \tag{3.19}$$

where  $\theta$  and  $\phi$  are the polar and azimuthal angles which define the direction  $\hat{\mathbf{n}}$ . These functions can be written as

$$\Phi_i^{Q^\pm} = \langle \pm \hat{\mathbf{n}} | \lambda_i^{(3)} | \pm \hat{\mathbf{n}} \rangle = \text{tr}(\lambda_i^{(3)} \Pi_{\pm, \hat{\mathbf{n}}}) \tag{3.20}$$

which satisfy the conditions of the Wigner  $Q$  symbol in Eq.(3.14). Therefore, it is now possible to map in the forward direction from the spin density matrix to the angular distributions.

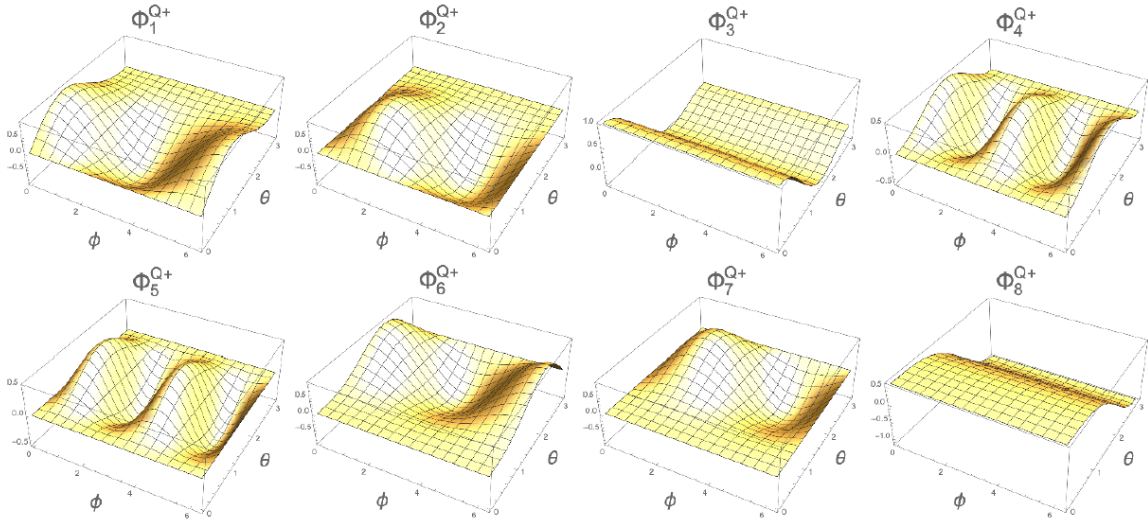


Figure 3.1: Plots show the shape of the Wigner  $Q$  symbols  $\Phi_i^{Q^+}$  corresponding to each Gell-Mann operators. In particular, the plots display how the angular probability density function varies in function of the angles.

The next step is to determine the set of Wigner  $P$  symbols to complement the  $Q$  symbols already found to reconstruct the density matrix from the experimental data.

Using the definition (3.15), the product of two generalised Gell-Mann operators for a generic dimension  $d$  is given by

$$\lambda_i^{(d)} \lambda_j^{(d)} = \lambda_i^{(d)} \left( \frac{d}{4\pi} \int d\Omega_{\hat{\mathbf{n}}} \Phi_j^{P^+}(\hat{\mathbf{n}}) |\hat{\mathbf{n}}\rangle \langle \hat{\mathbf{n}}| \right). \quad (3.21)$$

By taking the trace over these operators, it can be shown that the Wigner  $Q$  and  $P$  symbols are orthogonal. The eight Wigner  $P$  symbols for the  $d = 3$  dimension can be constructed using the respective  $Q$  symbols as follows

$$\Phi_i^{P^\pm}(\hat{\mathbf{n}}) = [M^{-1}]_{ij} \Phi_j^{Q^\pm}(\hat{\mathbf{n}}) \quad (3.22)$$

where the symmetric matrix  $M$  is composed of real elements defined by the inner product

$$M_{ij} = \frac{3}{2} \langle \Phi_i^{Q^\pm} \Phi_j^{Q^\pm} \rangle = \frac{3}{2} \frac{1}{4\pi} \int d\Omega_{\hat{\mathbf{n}}} \Phi_i^{Q^\pm}(\hat{\mathbf{n}}) \Phi_j^{Q^\pm}(\hat{\mathbf{n}}) \quad (3.23)$$

of the  $Q$  symbols. Therefore, the  $\Phi^{P^\pm}$  symbols for the  $W^\pm$  are

$$\begin{aligned} \Phi_1^{P^\pm} &= \sqrt{2}(5 \cos \theta \pm 1) \sin \theta \cos \phi & \Phi_5^{P^\pm} &= 5 \sin^2 \theta \sin 2\theta \\ \Phi_2^{P^\pm} &= \sqrt{2}(5 \cos \theta \pm 1) \sin \theta \sin \phi & \Phi_6^{P^\pm} &= \sqrt{2}(\pm 1 - 5 \cos \theta) \sin \theta \cos \phi \\ \Phi_3^{P^\pm} &= \frac{1}{4}(\pm 4 \cos \theta + 15 \cos 2\theta + 5) & \Phi_7^{P^\pm} &= \sqrt{2}(\pm 1 - 5 \cos \theta) \sin \theta \sin \phi \\ \Phi_4^{P^\pm} &= 5 \sin^2 \theta \cos 2\theta & \Phi_8^{P^\pm} &= \frac{1}{4\sqrt{3}}(\pm 12 \cos \theta - 15 \cos 2\theta - 5). \end{aligned} \quad (3.24)$$

It can be observed that the Wigner  $Q$  and  $P$  symbols for a given  $\lambda_i$  are not generally proportional to each other. The functions  $\Phi_i^{P^\pm}$  are illustrated graphically in Figure 3.2.

The spin density matrix parameters  $a_i$  for any  $W^\pm$  boson can be determined from charged lepton emission angles using Wigner  $P$  symbols as follows

$$a_i = \frac{1}{2} \int d\Omega_{\hat{\mathbf{n}}} p(l_{\hat{\mathbf{n}}}^\pm; \rho) \Phi_i^{P^\pm}. \quad (3.25)$$

The experimental measurement  $\hat{a}_i$  of the spin density matrix parameter  $a_i$  is derived through an angular average over the ensemble of decays as

$$\hat{a}_i = \frac{1}{2} \langle \Phi_i^{P^\pm} \rangle_{\text{av}} \quad (3.26)$$

In the case of the  $Z$  boson, the angular information aligns with multiple spin hypotheses along that direction. Therefore it is equivalent to a non-projective measurement along  $\hat{\mathbf{n}}$  and the coefficients of the matrix will undergo variations due to changes in Wigner  $Q$  and  $P$  symbols. In particular,  $Z$  boson will couple to fermions following the relation in

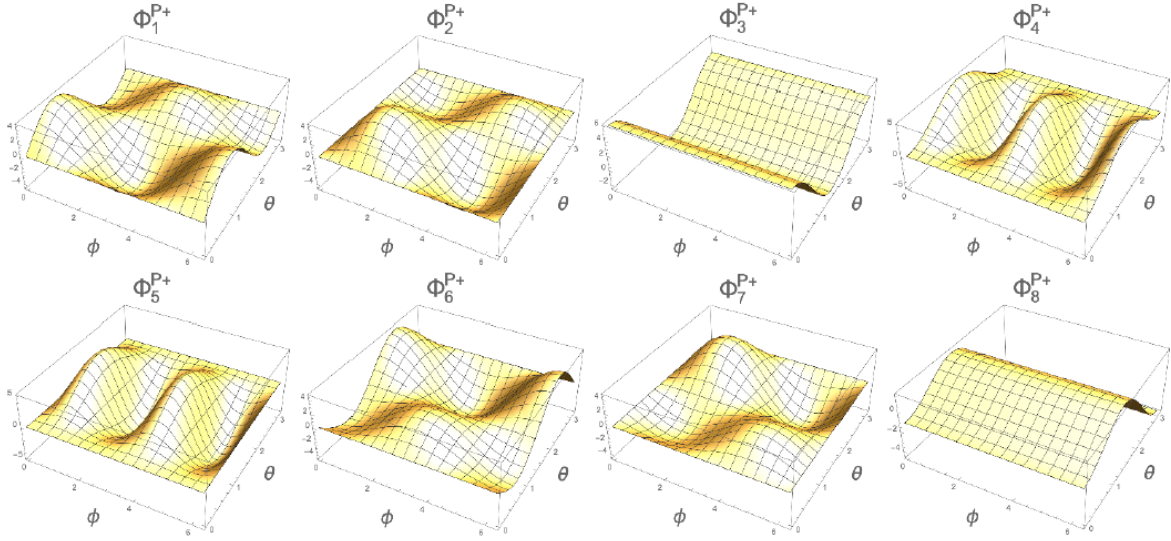


Figure 3.2: Plots show the shape of the Wigner  $P$  symbols  $\Phi_i^{P+}$  corresponding to each Gell-Mann operators.

Eq.(1.30) where  $\theta_W$  is the weak mixing angle and  $V_f$  and  $A_f$  are the vector and axial coupling constants. In the  $Z \rightarrow l^+l^-$  decays, these couplings can be represented by the right- and left-chiral coefficients  $c_R$  and  $c_L$  as follows:

$$V_l = c_L + c_R \quad A_l = c_L - c_R. \quad (3.27)$$

Given  $V_l = -0.0398$  and  $A_l = -0.5064$  [29], the coefficients are determined to be  $c_L = -0.273$  and  $c_R = 0.233$ . The generalised  $Q$  symbols for the  $Z$  boson can be written as a linear combination of projective  $Q$  symbols as follows

$$\tilde{\Phi}_{Z,i}^Q = \frac{1}{|c_R|^2 + |c_L|^2} \left( |c_R|^2 \Phi_i^{Q+} + |c_L|^2 \Phi_i^{Q-} \right) \quad (3.28)$$

Since  $|c_R| \neq |c_L|$ , the matrix in equation (3.23) written using generalized Wigner  $Q$  symbols is invertible. Therefore, it is possible to compute the generalized  $P$  symbols as follows:

$$\tilde{\Phi}_{Z,i}^P = A_{ij} \Phi_j^{P+} \quad (3.29)$$

where the matrix  $A_{ij}$  is defined as

$$A_{ij} = \frac{1}{|c_R|^2 - |c_L|^2} \begin{pmatrix} |c_R|^2 & 0 & 0 & 0 & 0 & |c_L|^2 & 0 \\ 0 & |c_R|^2 & 0 & 0 & 0 & 0 & |c_L|^2 \\ 0 & 0 & |c_R|^2 - \frac{1}{2}|c_L|^2 & 0 & 0 & \frac{\sqrt{3}}{2}|c_L|^2 & 0 \\ 0 & 0 & 0 & |c_R|^2 - |c_L|^2 & 0 & 0 & 0 \\ 0 & 0 & 0 & 0 & |c_L|^2 & 0 & 0 \\ |c_L|^2 & 0 & \frac{\sqrt{3}}{2}|c_L|^2 & 0 & 0 & \frac{1}{2}|c_L|^2 + |c_R|^2 & 0 \\ 0 & |c_L|^2 & 0 & 0 & 0 & 0 & |c_R|^2 \end{pmatrix}$$

When  $|c_R| = 1$  and  $|c_L| = 0$ , the matrix  $A$  becomes the identity matrix. Consequently, the generalised  $P$  symbols reduce to the Wigner  $P$  symbols, as previously derived in equation (3.24) for the  $W^+$  boson decay in the limit of massless fermion daughters. Therefore, the experimental value of the coefficients  $b_j$  for the  $Z$  boson in the spin density matrix (3.13) can be computed as

$$\hat{b}_j = \frac{1}{2} \left\langle \tilde{\Phi}_{Z,j}^P \right\rangle_{\text{av}} \quad (3.30)$$

Consider now the full  $WZ$  diboson system and extrapolate the correlation parameters  $c_{ij}$  of the spin density matrix. The  $c_{ij}$  coefficients of a general bipartite system of two parents  $A$  and  $B$ , can be computed by performing the double integral over the pair of daughter emission directions as

$$c_{ij} = \left( \frac{1}{2} \right)^2 \iint d\Omega_{\hat{\mathbf{n}}_1} d\Omega_{\hat{\mathbf{n}}_2} p(l_{\hat{\mathbf{n}}_1}^+, l_{\hat{\mathbf{n}}_2}^-, \rho) \tilde{\Phi}_{A,i}^P(\hat{\mathbf{n}}_1) \tilde{\Phi}_{B,j}^P(\hat{\mathbf{n}}_2), \quad (3.31)$$

where  $\hat{\mathbf{n}}_1$  and  $\hat{\mathbf{n}}_2$  are respectively the daughter directions from parents  $A$  and  $B$ . In the case of the  $WZ$  diboson system, the previous equation can be rewritten as

$$c_{ij} = \left( \frac{1}{2} \right)^2 \iint d\Omega_{\hat{\mathbf{n}}_1} d\Omega_{\hat{\mathbf{n}}_2} p(l_{\hat{\mathbf{n}}_1}^+, l_{\hat{\mathbf{n}}_2}^\pm, \rho) \tilde{\Phi}_{Z,i}^P(\hat{\mathbf{n}}_1) \Phi_{W,j}^{P^\pm}(\hat{\mathbf{n}}_2), \quad (3.32)$$

where the generalised Wigner  $P$  symbols defined in Eq.(3.29) are used for the  $Z$  boson, while the Wigner  $P$  functions from equations (3.24) are applied to  $W^\pm$  boson. In figure 3.3 are shown the value of  $c_{ij}$  coefficients for  $WW$ ,  $WZ$  and  $ZZ$  diboson systems. The angular integrals are performed in the rest frame of the respective parent particle, which will be described with details in Chapter 4.

The  $c_{ij}$  coefficients for the  $WZ$  system can be experimentally measured from the angular average as

$$\hat{c}_{ij} = \left( \frac{1}{2} \right)^2 \left\langle \tilde{\Phi}_{Z,i}^P(\hat{\mathbf{n}}_1) \Phi_{W,j}^{P^\pm}(\hat{\mathbf{n}}_2) \right\rangle_{\text{av}}. \quad (3.33)$$

For two or more indistinguishable parents, as in the case of the  $ZZ$  diboson system, the density matrix must be built to have symmetry under the exchange of parent particles' labels.

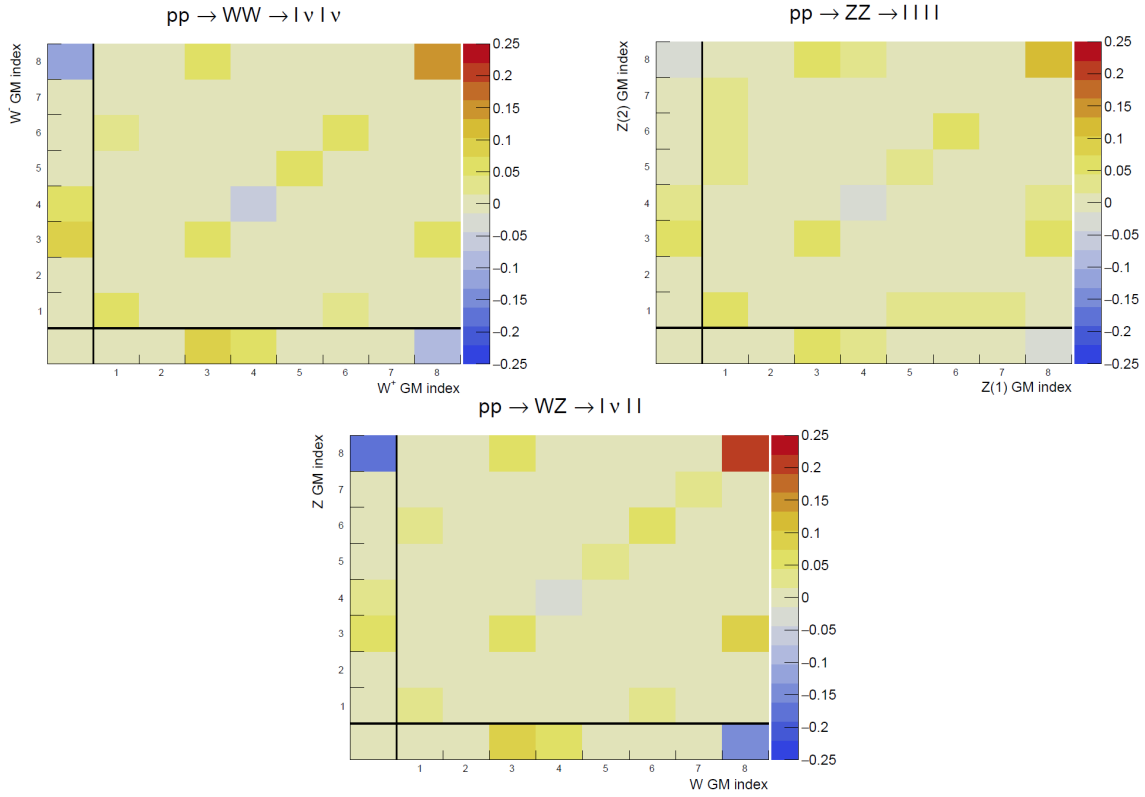


Figure 3.3: Gell-Mann parameters obtained from quantum state tomography for  $WW$ ,  $ZZ$ , and  $WZ$  systems. The bottom row of each plot contains the  $a_i$  parameters, the leftmost column the  $b_i$  parameters and the rows and columns 1-8 represent the  $c_{ij}$  coefficients. For the  $ZZ$  plot,  $a_i = b_j$  since they are indistinguishable particles.

### 3.3 Concurrence

As explained in the previous chapter, entanglement is a fundamental property belonging to quantum systems. In particular, a quantum mixed state  $\rho$  of  $n$  systems is considered entangled if it cannot be described as a convex combination of product states, such as

$$\rho = \sum_i^n p_i \rho_1^i \otimes \cdots \otimes \rho_n^i \quad 0 < p_i \leq 1. \quad (3.34)$$

Concurrence [23] is a quantum observable used to determine the entanglement of a state; if its value is greater than zero, the state is entangled [24]. The concurrence for a mixed state is defined using the convex roof extension method, which involves finding an upper bound for various ensembles of states  $(p_i, |\psi\rangle)$  that could result in the specific mixed

state  $\rho$ . Therefore, it can be expressed as

$$c(\rho) = \inf \sum_i p_i c(|\psi\rangle), \quad \sum_i p_i = 1, \quad p_i \geq 0, \quad (3.35)$$

where the infimum is computed over all the ensembles  $\{p_i, |\psi\rangle\}$  such that  $\rho = \sum_i p_i |\psi_i\rangle \langle \psi_i|$ . The concurrence can be obtained analytically for a bipartite system of a pair of qubits, reaching a maximum value of one for maximally entangled states. However, the concurrence cannot be determined analytically for bipartite systems with dimensions greater than  $2 \times 3$ . Nonetheless, it is still possible to compute a lower bound [5] for a mixed state as

$$(c(\rho))^2 \geq 2\text{tr}(\rho^2) - \text{tr}(\rho_A^2) - \text{tr}(\rho_B^2) \equiv c_{MB}^2 \quad (3.36)$$

where  $\rho_A$  and  $\rho_B$  are the reduced density matrix for subsystems  $A$  and  $B$  defined as in Eq.(2.30). For diboson systems such as  $WW$ ,  $ZZ$  and  $WZ$ , the spin density matrix is described by Eq.(3.13). Consequently, the terms in Eq. (3.36) can be written as

$$\begin{aligned} \text{tr}(\rho^2) &= \frac{1}{9} + \frac{2}{3} \sum_{i=1}^8 a_i^2 + \frac{2}{3} \sum_{j=1}^8 b_j^2 + 4 \sum_{i,j=1}^8 c_{ij}^2, \\ \text{tr}(\rho_A^2) &= \frac{1}{3} + 2 \sum_{i=1}^8 a_i^2, \\ \text{tr}(\rho_B^2) &= \frac{1}{3} + 2 \sum_{j=1}^8 b_j^2. \end{aligned} \quad (3.37)$$

Therefore, the bound (3.36) can be computed as

$$c_{MB}^2 = -\frac{4}{9} - \frac{2}{3} \sum_{i=1}^8 a_i^2 - \frac{2}{3} \sum_{j=1}^8 b_j^2 + 8 \sum_{i,j=1}^8 c_{ij}^2 \quad (3.38)$$

where  $a_i$ ,  $b_j$  and  $c_{ij}$  are the 80 GGM coefficients of the  $3 \times 3$  spin density matrix. This lower bound has an important property: if  $c_{MB}^2 > 0$ , then  $c(\rho) > 0$  which implies the state considered is entangled. Otherwise, if  $c_{MB}^2 \leq 0$ , this measure cannot be used to determine whether the state is entangled. In the case of a qutrit pair, the maximum concurrence is achieved in a completely symmetric and entangled pure state, where it equals  $(c(\rho))^2 = \frac{4}{3}$ .

A detailed analysis of bipartite systems of qutrits of heavy vector bosons has been performed by Alan Barr et al. [5] using Monte Carlo simulations of proton-proton collision at the centre-of-mass energy of 13 TeV without any selection or reconstruction on the leptons. In the analysis, the coefficients of the spin density matrix have been calculated for  $WW$ ,  $ZZ$  and  $WZ$  diboson systems, which can be used to show the consistency

<b>Process</b>	$\mathbf{c}_{\text{MB}}^2$
$pp \rightarrow W^+W^- \rightarrow \ell^+\nu_\ell\ell^-\bar{\nu}_\ell$	-0.147
$pp \rightarrow H(125) \rightarrow WW^{(*)} \rightarrow \ell^+\nu_\ell\ell^-\bar{\nu}_\ell$	0.973
$pp \rightarrow H(200) \rightarrow WW \rightarrow \ell^+\nu_\ell\tau^-(30)\bar{\nu}_\tau$	0.946
$pp \rightarrow ZZ \rightarrow e^+e^-\mu^+\mu^-$	-0.21
$pp \rightarrow H(125) \rightarrow ZZ^{(*)} \rightarrow e^+e^-\mu^+\mu^-$	0.53
$pp \rightarrow W^+Z \rightarrow e^+\nu_e\mu^+\mu^-$	0.10

Table 3.1: Lower bound of the concurrence for different diboson systems obtained with quantum state tomography [5].

of the results obtained for the Gell-Mann parameters in Figure 3.3. Table 3.1 reports the physical events considered in the study and the respective concurrence computed using Eq.(3.36) in the inclusive region of phase space. Quantum spin observables, especially concurrence, have been shown [4] to serve as valuable probes and constraints in studying new physics, particularly as described by higher-dimensional operators within the Standard Model effective field theory. This thesis focuses on the  $WZ$  system because it has the highest concurrence among diboson final states when considered inclusively. Additionally, the  $WZ$  system presents a promising opportunity for exploring new physics models that are not yet constrained by existing data.

# Chapter 4

## Data analysis

This chapter presents the analysis conducted for this thesis. It begins with an introduction to the data and Monte Carlo samples, including a description of the studied object. Next, it details the selection criteria and methods used for particle-level analysis. Then, it continues with the measurement of the coefficients of the spin density matrix and the introduction of the bootstrap method and the unfolding technique. Finally, the results of the lower bound of the concurrence are presented including studies in different regions of the phase space, targeted to enhance the entanglement between the two bosons

### 4.1 Monte Carlo Simulation

The dataset used for the analysis in this thesis has been generated through Monte Carlo simulation using the software `MG5_aMC@NLO` [3], which is a framework designed to provide all the essential components for simulating hard-scattering processes in both Standard Model (SM) and Beyond Standard Model (BSM) phenomenology. Hard scattering is the interaction between the partons belonging to the colliding protons and the outgoing particles in the interactions. The sample has then been interfaced with `Pythia` [7] for the parton shower and hadronization process of the events. During parton showering, an initial high-energy parton (a quark or gluon) undergoes a series of emissions, producing a cascade of lower-energy partons by emitting gluons and splitting gluons into quark-antiquark pairs. All coloured particles involved in the hard scattering undergo this process, including the initial partons belonging to the proton. `Pythia` also accounts for electroweak showering, where all charged particles can emit photons, leading to the production of additional quarks or leptons. The hadronization instead is the process by which the free quarks and gluons produced at the end of the parton showering stage combine to form hadrons. In Monte Carlo simulations, these processes are fundamental for creating realistic and accurate simulations that match what is observed in actual experiments. `Pythia` also simulates the evolution of the remaining partons in the proton

that are not involved in the hard scattering.

The events generated for this study simulate the collision of  $pp$  beams at LHC with a centre of mass energy of  $\sqrt{s} = 13$  TeV, which create, at leading order (LO) in  $\alpha_s$ , a pair of  $WZ$  bosons decaying into fully leptonic mode as follows

$$pp \rightarrow W^\pm Z \rightarrow l\nu ll. \quad (4.1)$$

where the  $l$  are the leptons, which can be either electrons  $e$  or muons  $\mu$ , while  $\nu$  is the respective neutrino.

The cross-section used for the generation for  $pp \rightarrow W^\pm Z$  is computed at NNLO with MATRIX [22] and is equal to

$$\sigma = 49.1_{-1.0}^{+1.1} \text{ pb} \quad (4.2)$$

Therefore, the cross-section for the channel under study can be computed as

$$\sigma(pp \rightarrow WZ) \times BR(W^\pm Z \rightarrow l\nu ll) = 0.7179 \text{ pb} \quad (4.3)$$

where the branching ratio for the events can be obtained from

BR ( $W \rightarrow l\nu$ )	10.86%
BR ( $Z \rightarrow l^+l^-$ )	3.3658%
BR( $WZ \rightarrow l\nu ll$ )	1.4621 %

Table 4.1: The branching ratio for the process studied during the analysis[29].

The number of events for the analysis has been calculated using the cross-section described before and the luminosity that is expected to be collected by ATLAS combining the data-taking at  $\sqrt{s} = 13$  TeV and  $\sqrt{s} = 13.6$  TeV, corresponding to  $L = 450 \text{ fb}^{-1}$ . In the analysis that will be performed from LHC experiments the data-taking at different energies will have to be considered separately, but the significance of the measurement or any interpretation performed on the result can be combined across the data-taking periods.

## 4.2 Event selections

In this thesis, the analyses were conducted at various stages using the Rivet toolkit [8], a framework designed to read and implement event selection and reconstruction of the HEPMC format, commonly used by all MC generators for particle physics. In particular, there are two distinct levels at which the observables of interest are defined, the parton-level corresponds to the "truth" generated through the Monte Carlo simulation, without considering any showering effects on the lepton and any selection. Here, the  $W$

and  $Z$  bosons considered during the analysis are taken just before their weak decay and the four-vectors of the decay products, including the neutrino, are taken directly from the MC record and consequently correctly associated with the parent boson. The other level where the observables are defined is the particle level, which considers effects due to the selection and reconstruction, similar to what an analysis conducted on data collected at an LHC experiment would do. Effects due to the limited resolution of the detector are not considered. This approximation is valid for the feasibility study conducted in this thesis because the main distortion effects in lepton reconstruction are due to the detector acceptance, considered in the selection cuts applied, while the leptons in the detector acceptance are reconstructed with high efficiency ( $> 90\%$ ) and high resolution [11]. At this stage, a realistic analysis is performed, taking into account several factors: the minimum transverse momentum required for leptons to be efficiently reconstructed, the detector acceptance, and the criteria necessary for an event to meet the trigger requirements at ATLAS and CMS. Triggers are systems or algorithms that rapidly evaluate the basic characteristics of each collision event in real-time. When an event meets certain predefined criteria, it "passes the trigger" and is subsequently saved for more detailed analysis. The particle level selections used to replicate detector effects and define the physical objects are

- The leptons are merged (dressed) with all photons in a clustering cone of  $\Delta R = 0.1$ .
- The momentum of each lepton should be  $p_T > 7$  GeV,
- Pseudorapidity of the leptons:  $|\eta| < 2.5$ ,

where  $\Delta R$  represents the angular separation between two particles in the detector, used to define a clustering cone around the particle of interest and it is defined as  $\Delta R = \sqrt{\Delta\eta^2 + \Delta\phi^2}$ , with  $\Delta\eta$  and  $\Delta\phi$  the difference of pseudorapidity and azimuthal angle between of two particles. Instead, the selection of  $|\eta| < 2.5$  reflects the pseudorapidity range of precision tracking of the Inner Detector of the ATLAS experiment. Experiments located at colliders cannot reconstruct neutrinos, and the only experimental signature of the presence of these particles is the missing transverse energy. The missing transverse energy  $E_T^{miss}$  is defined as the imbalance in the total transverse energy observed in the detector. It is calculated by summing the transverse momenta of all detected particles and then taking the vector sum:

$$E_T^{miss} = - \sum_i p_{T,i} \quad (4.4)$$

where  $p_{T,i}$  is the transverse momentum of the  $i$ -th detected particle. Missing transverse energy is fundamental in high-energy physics analysis for identifying and studying events involving neutrinos, such as  $W$  decay, as they do not interact with the detector directly.

The same quantity is used in this thesis for the particle level analysis, which consequently does not use any truth information on the longitudinal coordinate of the neutrino.

The events at the particle level selected for contributing to the  $pp \rightarrow W^\pm Z \rightarrow l\nu ll$  signal process must satisfy the following requirements:

- The transverse momentum of the leading lepton must be greater than 27 GeV,
- Number of final leptons  $n_l = 3$ ,
- Total charge of the event  $q_{tot} = \pm 1$ .

The requirement that the leading lepton's transverse momentum exceeds 27 GeV is the criterion needed for the trigger selection. After applying the previous event selection criteria, figure 4.1 displays the distributions of various kinematic variables for the fundamental particles used in the analysis at both the particle and parton levels. Here, the difference in the number of events passing the two selections is clear, as is the variation in the shape of their distributions. These discrepancies will affect the reconstruction of the variables of interest, as demonstrated in the next chapters. The accurate reconstruction of full events is a highly complex analysis, particularly when it comes to identifying which charged leptons originate from the decay of the  $W$  or  $Z$  bosons. This challenge becomes even greater when all the leptons in the final state belong to the same family, such as when  $WZ \rightarrow eee$  and  $WZ \rightarrow \mu\mu\mu$ . To address this issue, the  $Z$  boson is reconstructed using an algorithm that relies on the invariant mass of the decay products. Specifically, the  $Z$  boson is initially reconstructed for the two possible pairs of leptons that could have decayed from the boson, and then the configuration with a mass closer to the true  $Z$  boson mass, listed in Table 1.1, is selected. Plot (d) in Fig.4.1d illustrates the reconstructed  $Z$  boson mass for events where all charged leptons belong to the same family and for those where they do not, demonstrating the algorithm's effectiveness.

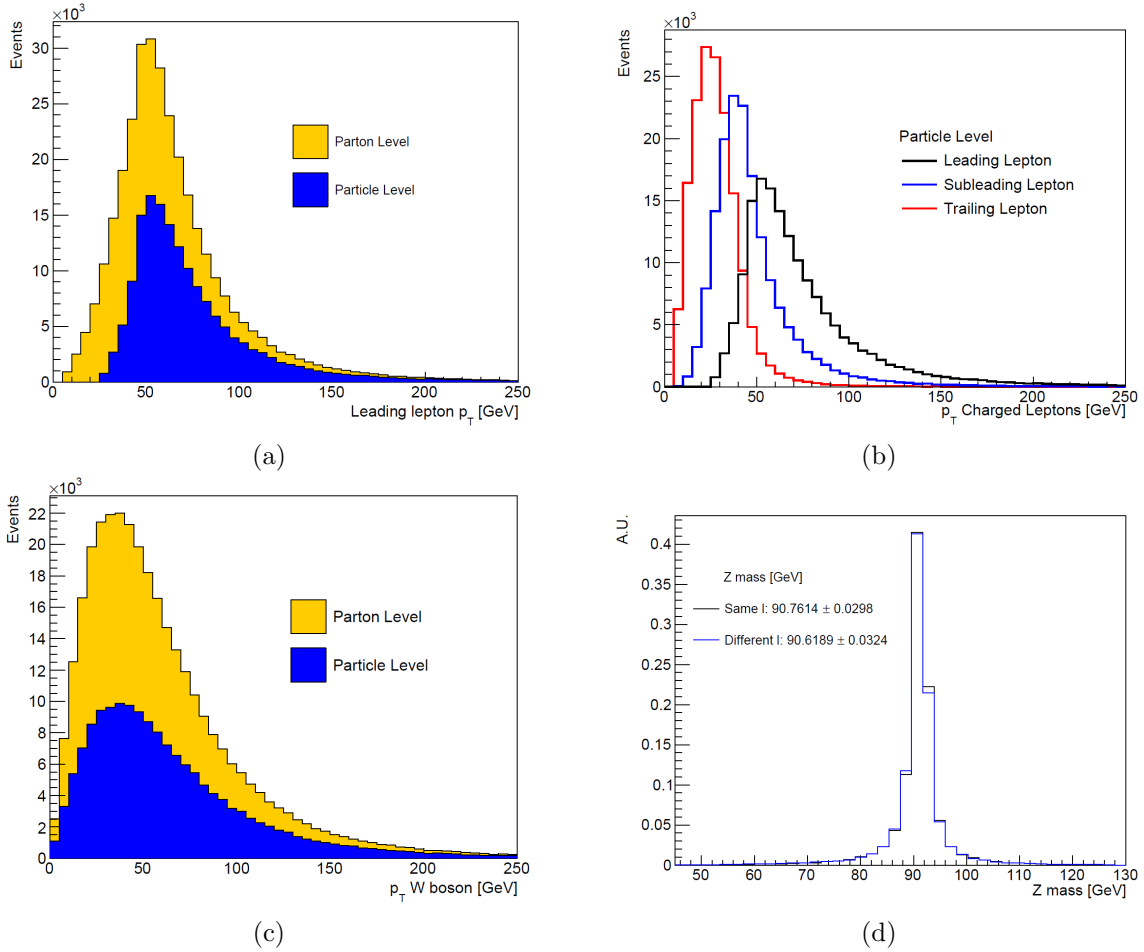


Figure 4.1: Distribution of kinetic variables of particles in the analyzed process. Plot (a) shows the difference in transverse momentum between particle and parton levels for the leading charged leptons. Figure (b) presents the transverse momentum ( $p_T$ ) of all the charged leptons involved in the  $WZ$  decay. Plot (c) reports the  $p_T$  of the  $W$  boson at the particle level, where it is reconstructed, and the parton level obtained from MC simulation. Finally, plot (d) shows the reconstruction of the  $Z$  mass at the particle level, distinguishing between cases where the final charged leptons are all from the same family and where they are not.

### 4.2.1 Reconstruction of the $p_z$ component of the neutrino momentum

The selected  $WZ$  final state has three charged leptons, that are well reconstructed in multipurpose detectors such as ATLAS or CMS. As previously illustrated, the reconstruction of charged leptons is based on their flavour and charge, with additional information on

the  $Z$  mass included in cases involving three leptons of the same flavour. The remaining particle to reconstruct is the  $W$  boson, obtained by summing the four-momentum of the remaining charged lepton and the neutrino. Given the aim of this work, which is to simulate the same reconstruction and selection of an analysis performed in a real detector, this study faced the same limitation presented in a multipurpose detector for the neutrino reconstruction which arises from the fact that the neutrino ( $\nu$ ) produced in the  $W$  boson decay does not interact with the detector. In this analysis, the experimental signature of the neutrino corresponds to the missing transverse energy  $E_T^{miss}$  of the event. However, to determine the complete  $W$  boson four-momentum, it is necessary to reconstruct the  $p_z$  component of the neutrino's momentum. To address this issue, the mass of the  $W$  boson given in Table 1.1, can be used as a constraint to obtain the missing momentum component of the neutrino. Using the four-momentum conservation of the process  $W \rightarrow l\nu$ , the following expression can be obtained

$$\begin{aligned} m_W^2 &= (p_l^2 + p_\nu^2) \\ &= m_l^2 + m_\nu^2 + 2(E_l E_\nu - \vec{p}_l \vec{p}_\nu) \end{aligned} \quad (4.5)$$

where the mass of the neutrino can be neglected. This equation can be rewritten and solved as a quadratic equation in terms of the  $p_{\nu,z}$  of neutrino. The equation has the form

$$ap_{\nu,z}^2 + bp_{\nu,z} + c = 0. \quad (4.6)$$

with the coefficients  $b$  and  $c$  defined as

$$\begin{aligned} a &= E_l^2 - p_{l,z}^2, \\ b &= -2kpl_z, \\ c &= E_l^2 p_{\nu,T} - k^2 \end{aligned} \quad (4.7)$$

where the parameter  $k$  is written as

$$k = \frac{m_W^2 - m_l^2}{2} + p_{l,x}p_{\nu,x} + p_{l,y}p_{\nu,y}. \quad (4.8)$$

In previous equations,  $E_l$  represents the energy of lepton,  $p_{l,x}, p_{l,y}, p_{l,z}$  are the momentum component of the lepton and  $p_{\nu,T} = \sqrt{p_{\nu,x}^2 + p_{\nu,y}^2}$  is the missing transverse energy of the event. When the equation yields two solutions, indicated by a positive discriminant, the chosen  $p_{\nu,z}$  for the neutrino is the one with the smallest magnitude. If the discriminant is negative, the solution is imaginary and as  $p_{\nu,z}$  component is taken the real part of the solution. In this analysis, this occurred in only 9% of the reconstructed events at the parton level. Figure 4.2 shows the transverse momentum  $p_T$  of the neutrino at the parton and particle level, along with the  $p_z$  values reconstructed using Eq. (4.5) and those obtained directly from the momentum provided by the Monte Carlo simulation. The plot shows that the shape of the  $p_{\nu,z}$  component reconstructed at the particle level is more peaked compared to the truth level, highlighting the effect of using the previously described algorithm for neutrino reconstruction.

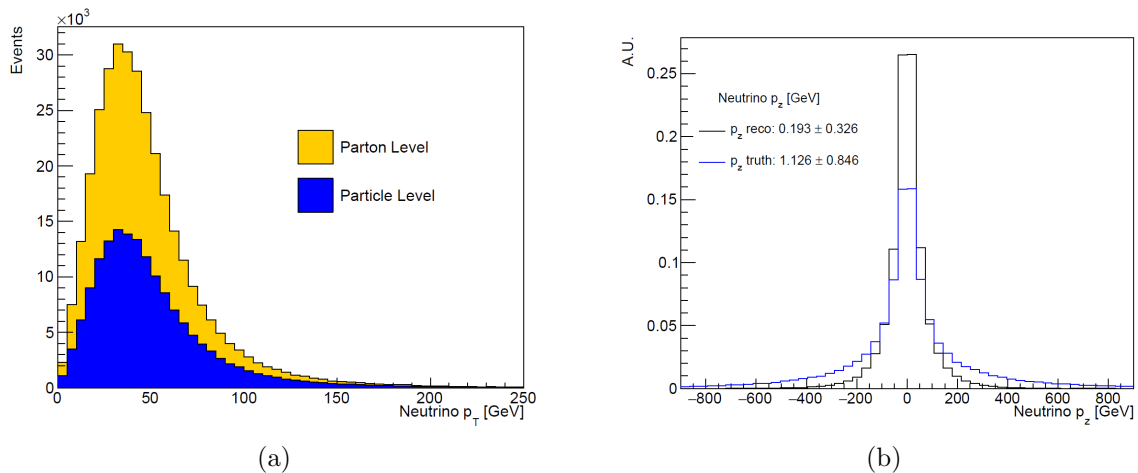


Figure 4.2: Distribution of transverse momentum distribution of the neutrino (a) at parton and particle level and the comparison (b) between neutrino  $p_z$  reconstructed using the missing transverse energy (MET) and the longitudinal momentum given at the truth level.

### 4.3 Basis choice

As introduced in Chapter 3, studying the decay products of the  $WZ$  boson bipartite system is fundamental for retrieving the spin density matrix of the ensemble, in particular the coefficients  $a_i$ ,  $b_j$  and  $c_{ij}$  need to be determined. To achieve this, a quantum state tomography approach, described in detail in Chapter 3, is performed on the leptons of the simulated final state. The coefficients of the spin density matrix (3.13) can then be obtained using the Weyl-Wigner formalism described in Section 3.2, where the parameters depend on the angular distributions of the decay products. However, a proper basis choice is required for this analysis. The polar and azimuthal angles  $\theta$  and  $\phi$  of the leptons must be considered in the centre of mass frame of the parent heavy vector boson. During the analysis, the fundamental particles considered for the reconstruction of spin density matrix parameters are the decayed charged lepton from the  $W^\pm$  bosons for the coefficients  $a_i$  and the positive lepton from  $Z$  bosons for the  $b_j$ . The parameters  $c_{ij}$  are computed using Eq.(3.35) with the same leptons employed for the other coefficients.

In the  $WZ$  system, the relevant reference frames are obtained in two steps: a first  $\hat{z}$  boost from the laboratory to the  $WZ$  diboson centre-of-mass frame, then followed by a  $\hat{k}$  boost from  $WZ$  frame to the rest frame of each single boson. Figure 4.3 illustrates an example of the  $W^+$  centre-of-mass frame with the newly chosen axes.

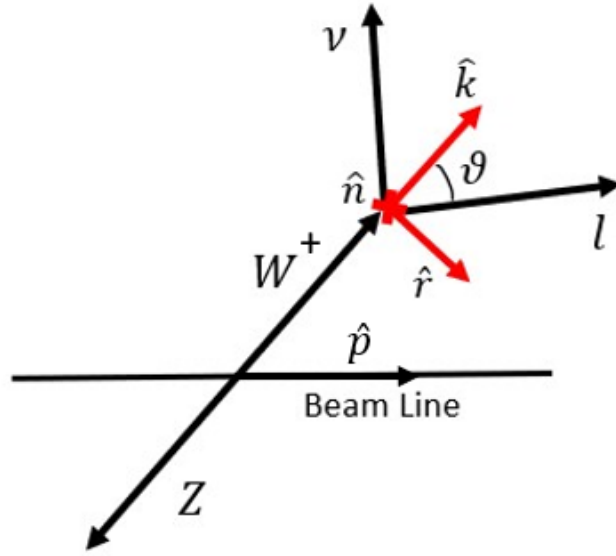


Figure 4.3: Sketch of the new axes in the rest frame of the  $W^+$  boson. A similar procedure is applied for the centre-of-mass frame of  $Z$  boson. The  $\hat{\mathbf{n}}$  axis is pointing out of the page. The angle  $\theta$  in the figure is the polar angle used to compute spin density matrix parameters.

The new basis shown in Figure 4.3, also called *helicity basis*, is defined as follows

$$\left\{ \begin{array}{l} \hat{\mathbf{k}} = \text{direction of the boson} \\ \hat{\mathbf{r}} = \frac{1}{r}(\hat{\mathbf{p}} - y\hat{\mathbf{k}}) \\ \hat{\mathbf{n}} = \frac{1}{r}(\hat{\mathbf{p}} \times \hat{\mathbf{k}}) \end{array} \right. \quad (4.9)$$

where  $\hat{\mathbf{p}}$  is the direction of one of the proton beams, while the parameters  $r$  and  $y$  are defined as

$$y = \hat{\mathbf{p}} \cdot \hat{\mathbf{k}} \quad r = \sqrt{1 - y^2}. \quad (4.10)$$

In the case of  $W^-$  boson, the procedure to determine the new basis is identical, but the direction of the  $\hat{\mathbf{k}}$  axis is inverted. This analysis marks the first time that the  $W^-$  boson is considered for this type of measurement.

## 4.4 Measurement of spin density matrix coefficients

Using the new basis (4.9) defined in the previous section and the definition of the spin density matrix coefficients given in Eqs. (3.26),(3.30) and (3.33), it is now possible to compute the charged lepton decay angles in the rest frame of the boson and utilize them to determine the parameters of the matrix. In particular, the spin density matrix cannot be obtained for measurements of a single instance of the state and, for the analysis, the ensemble of the decays has to be considered. Each coefficient of the matrix, such as the  $\hat{a}_i$  parameter in Eq.(3.26), is determined by plotting the Wigner  $P$  symbols for each event using azimuthal  $\phi$  and polar  $\theta$  angles, and then taking the mean value of the histograms. Figure 4.4 presents the results of some of the  $a_i$  coefficients for the  $W^\pm$  boson of the  $W^\pm Z$  system at the particle level. The error for these values is the error of the mean obtained from the histograms.

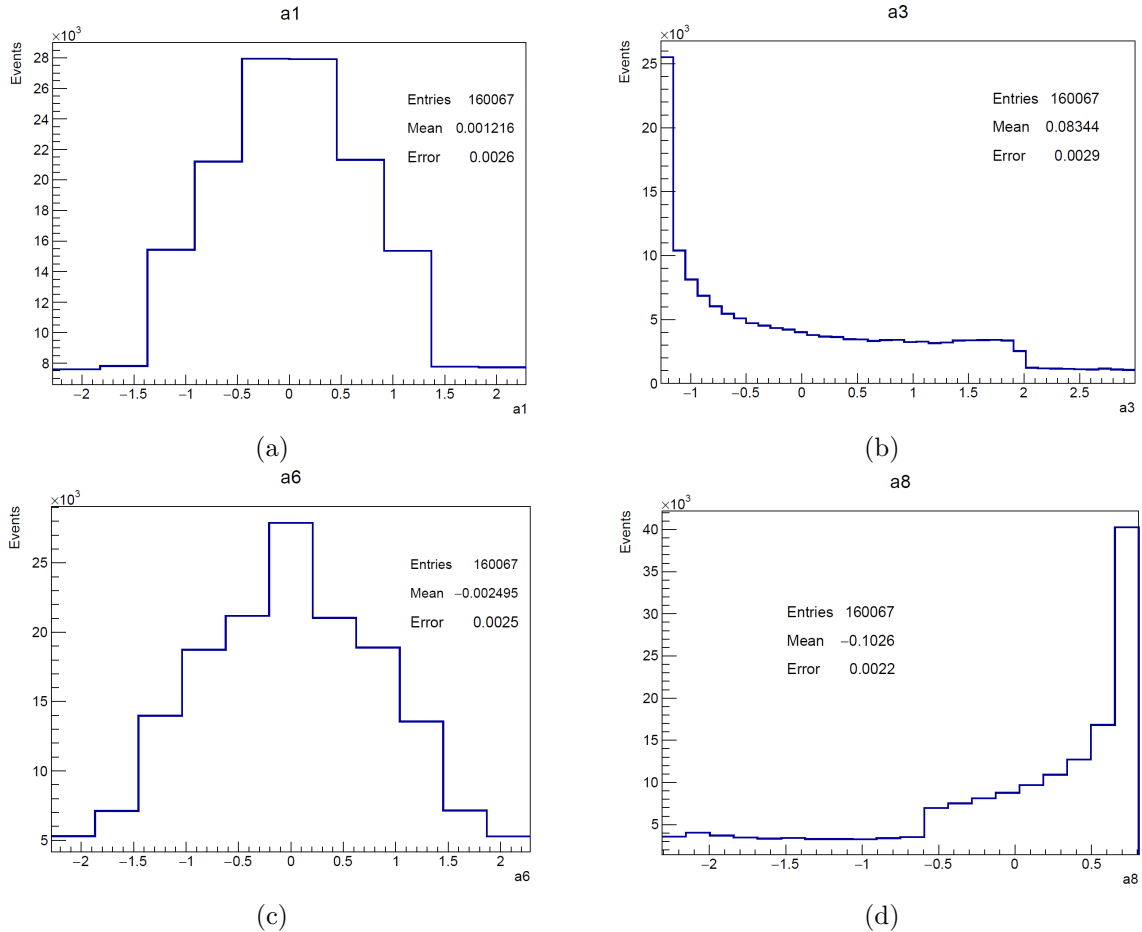


Figure 4.4: Representation of four  $a_i$  coefficients of the spin density matrix related to  $W$  boson spin.

Similarly, the  $b_j$  coefficients have been measured for the  $Z$  boson, where the positively charged lepton is chosen for determining the generalized Wigner  $P$  symbols in Eq.(3.29). The results obtained for the  $\hat{b}_j$  parameters are reported in Figure 4.5, which shows plots of several coefficients.

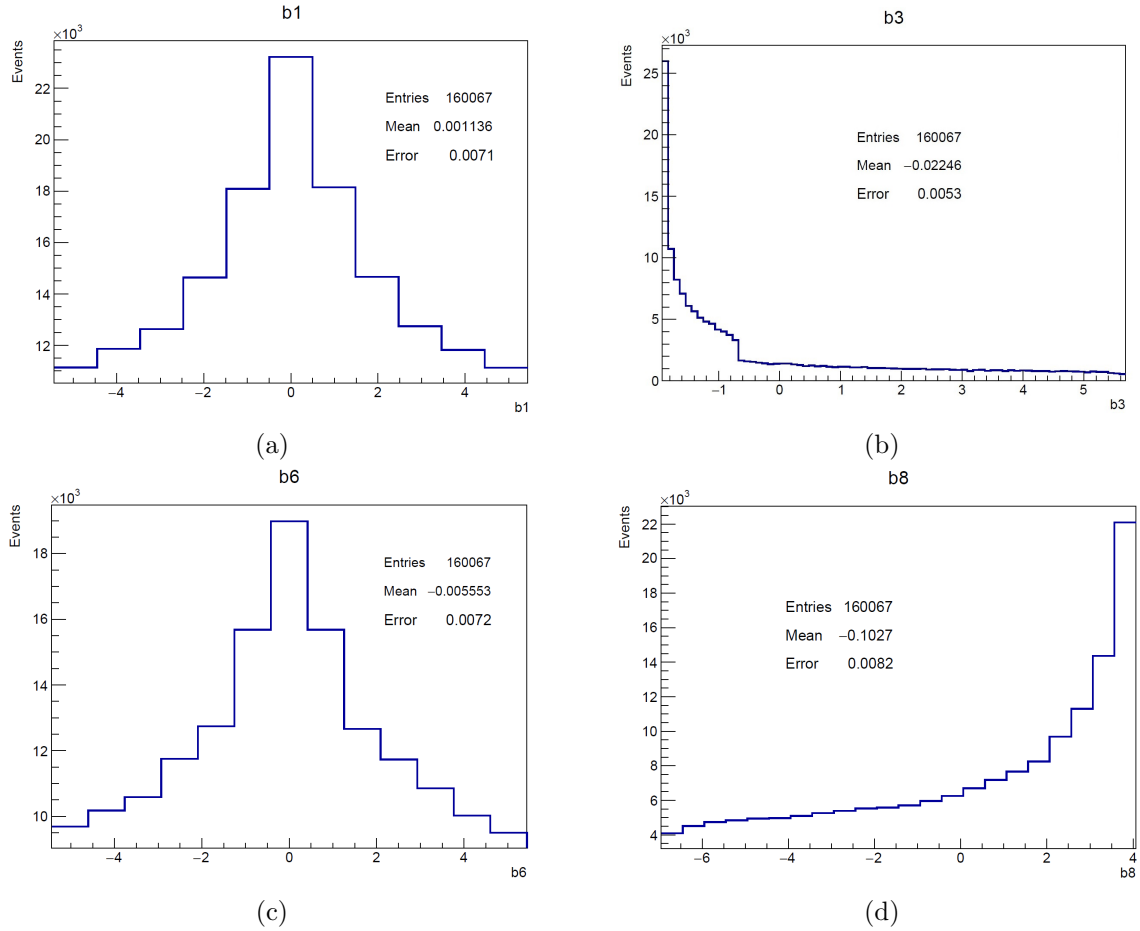


Figure 4.5: Representation of four  $b_j$  coefficients of the spin density matrix related to  $Z$  boson spin.

Finally, the  $c_{ij}$  coefficients, responsible for the correlations between the two heavy vector bosons, have been computed using Eq. (3.33). The Wigner  $P$  symbols used in this calculation are the same as those used for determining the  $a_i$  and  $b_j$  parameters. Figure 4.6 displays some of the 64  $c_{ij}$  coefficients of the  $WZ$  diboson system.

The number of bins for each coefficient varies significantly in all the figures presented in this section. The choice of the binning is a crucial aspect of the analysis process, as overly broad binning could introduce bias into the value of the extracted parameter. Therefore to minimize the bias in the histogram mean, the binning has been selected to

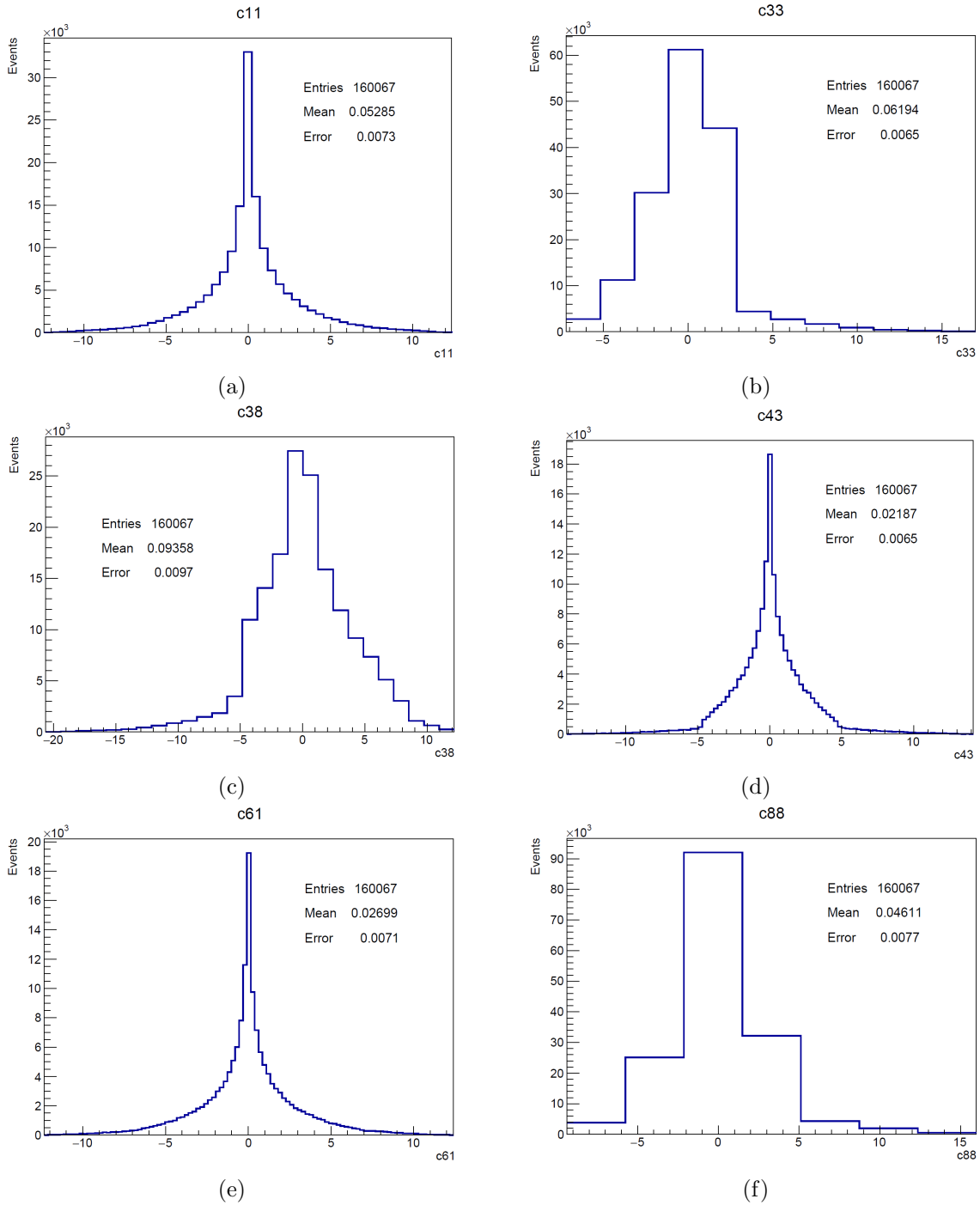


Figure 4.6: Representation of various  $c_{ij}$  coefficients of the spin density matrix that parametrise the correlations between  $W$  and  $Z$  bosons.

have a difference below 5% between the binned and unbinned mean at the truth level.

Using this reference frame, most of these coefficients, which are the parameters of the spin density matrix of the  $WZ$  diboson systems defined in Chapter 3, are compatible with zero at the LHC, with small deviations in some directions.

#### 4.4.1 Differences between Parton and Particle level

As explained in Section 4.2, the primary difference between parton and particle levels lies in the selection applied to events at the particle level and the reconstruction needed to extract the neutrino  $p_z$ . Specifically, there are two effects at the particle level: the selection criteria for objects, which include requirements on the  $p_T$  and  $\eta$  of each lepton, and the event selection that simulates the trigger, where the  $p_T$  of the leading lepton exceeds 27 GeV. Additional differences can be generated by the radiation of additional particles, such as photons, that modify the directions of the particle level leptons compared to parton level. These selections are necessary to replicate the detector effects, which can smear the density distribution of the observed physical variable due to limited acceptance and reconstruction effects.

Now let's examine how these cuts applied to the leptons affect the spin density matrix coefficients at different levels. Figure 4.7 shows the plots of two matrix parameters for the  $WZ$  diboson system.

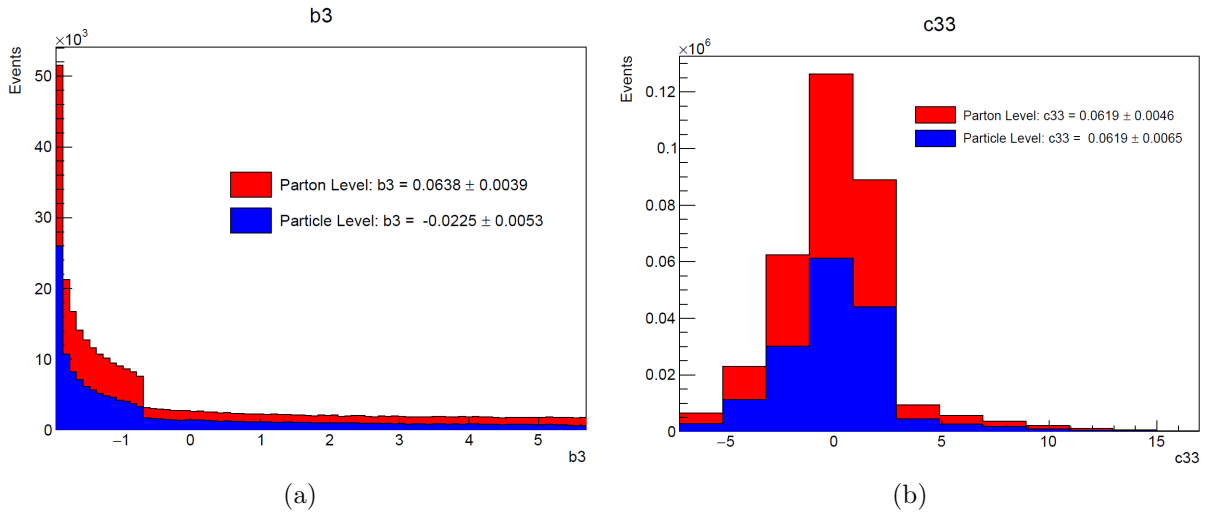


Figure 4.7: Comparison between  $b_3$  (a) and  $c_{33}$  (b) coefficients of the spin density matrix at particle and parton level.

One noticeable difference from the previous plots is the number of events at the parton and particle levels. Due to selection effects and the limitations of the measuring

device, some events cannot be detected by the detector. In particular, the number of events per level is reported in Table 4.2.

Level	Events
Parton	329967
Particle	160067

Table 4.2: Number of the events obtained in the analysis at particle and parton level.

From this table, it is possible to determine the detector efficiency of the analysis at the particle level for the process  $WZ \rightarrow l\nu ll$  as the ratio of the particle events and the parton one. Therefore, the efficiency  $\varepsilon$  can be calculated as

$$\varepsilon = \frac{N_{particle}}{N_{parton}} = 0.458. \quad (4.11)$$

All 80 coefficients of the density matrix are presented in Figure 4.8, in particular, the left plot shows the parameters computed at the parton level, while in the right plot, the coefficients are obtained at the particle level with all the selections defined in Section 4.2.

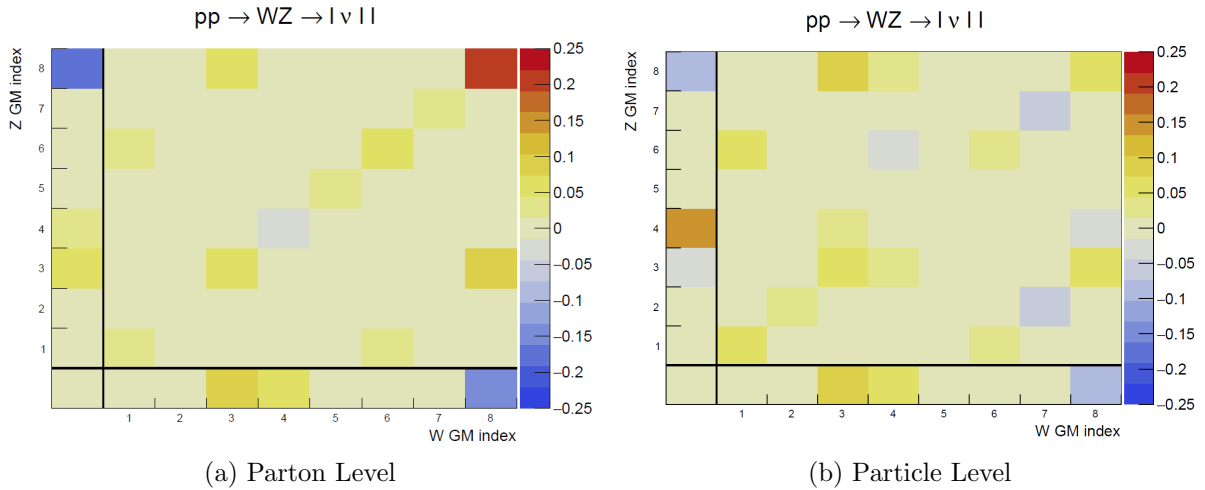


Figure 4.8: Visual comparison of the spin density matrix coefficients at the parton level (a) and the particle level reveals significant changes in some values from one level to the other.

It is evident that various values of the parameters in the two plots are significantly different, indicating that the reconstructed values deviate from the theoretical predictions

at the parton level. This deviation arises from the effects introduced at the particle level described in Section 4.2. Consequently, these effects have distorted the shape of the distribution of certain coefficients, and this distortion cannot be corrected merely by accounting for the efficiency differences between the particle and parton levels. To address this issue, the effects induced by the detector on the reconstructed quantities must be removed using unfolding techniques. This procedure, which is explained in detail in the following chapters, is fundamental to retrieving the true distribution of measured values.

#### 4.4.2 Studies with different analysis limitations

In the previous section, we highlighted the key differences in the coefficients of the spin density matrix between the two types of analysis levels. Now, let's examine the particle level to understand the implications on the parameters when analysis limitations are altered or removed. In particular, three scenarios will be considered in this section as shown in Table 4.3, where the two main limitations of the realistic analysis are the cut on the transverse momentum  $p_T$  of the leading lepton, which simulates the trigger, and the reconstruction of the four-momentum of the neutrino.

Different scenarios	
Scenario 1	No lepton $p_T > 27$ GeV cut
Scenario 2	Truth neutrino
Scenario 3	No lepton cut and truth neutrino

Table 4.3: Description of the 3 different scenarios considered in the analysis at particle level. In the first scenario, the analysis has been performed without applying the requirement of the transverse momentum on the leading lepton, while in the second, it has been used the four-momentum of the truth neutrino for the analysis. The last scenario considered both these cases simultaneously.

Figure 4.9 displays some coefficients of the spin density matrix for the  $WZ$  diboson system computed at the truth level, at the particle level and at the particle level with the different scenarios explained in Table 4.3, making a comparison between the results obtained in the different cases. In each histogram of Figure 4.9, the distributions have been normalized to emphasize the impact on shape. In particular, the most significant effect which spoils the particle level from the theoretical prediction is the reconstruction of the  $p_z$  momentum of the neutrino, in fact when considering Scenario 2 and 3 where it is used the four-momentum of the neutrino at parton level, the difference between coefficients at parton and particle level is reduced. However, it has been studied that

this is not true for all the coefficients of the spin density matrix, where Scenario 3 was not improving the agreement with the parton level. This discrepancy could be attributed to other effects differentiating the truth and particle level, such as additional radiation of photons or other selection criteria applied on the lepton, like cuts on the  $\eta$  and  $p_T$  described in Section 4.2. Additionally, it can be noticed that the condition on the lower bound of leading leptons' transverse momentum (Scenario 1) does not significantly affect the original particle level results. Overall, the analysis highlights that a good reconstruction of the longitudinal momentum  $p_z$  of the neutrino is an essential aspect for the reconstruction of the spin density matrix of the  $WZ$  system.

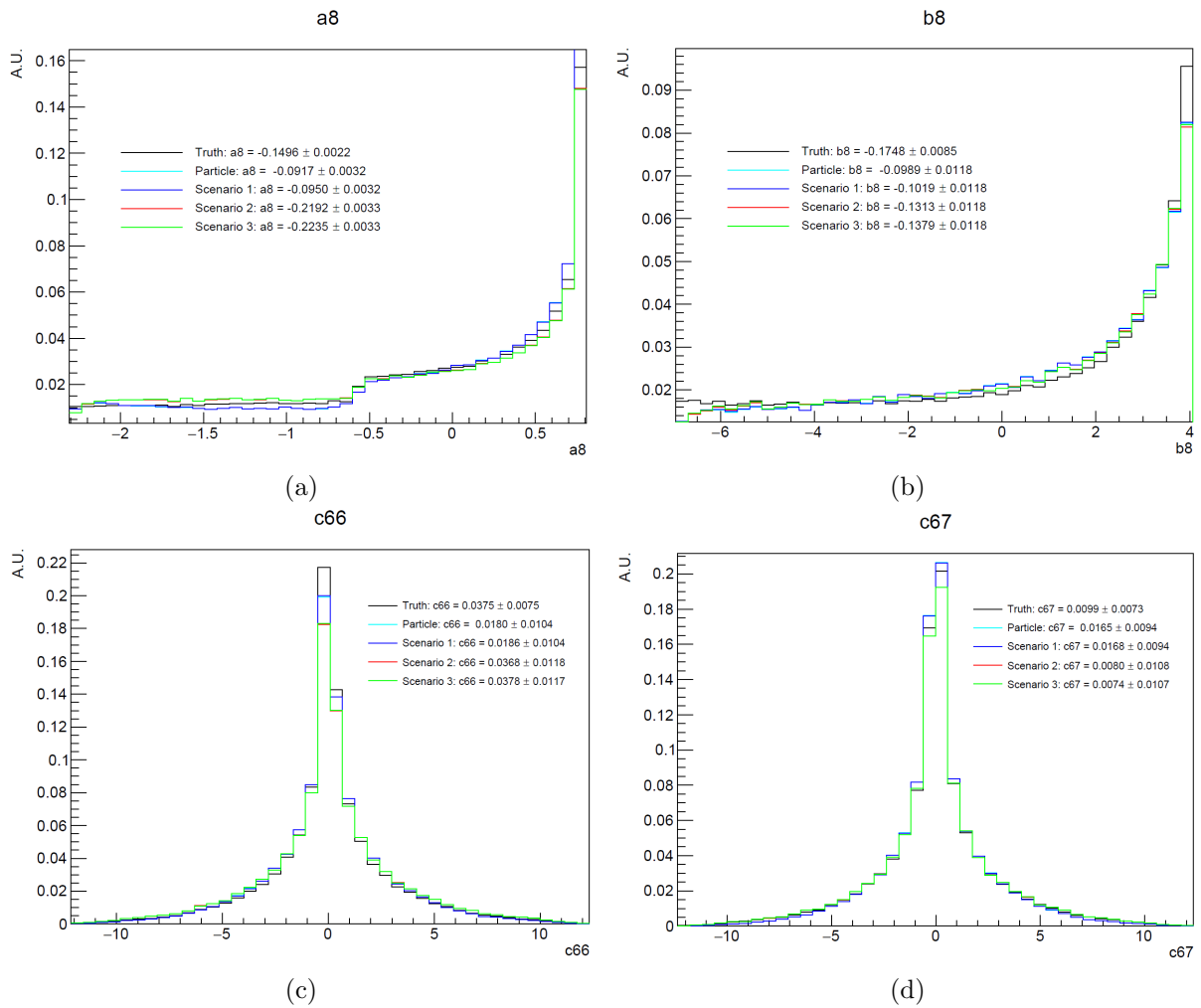


Figure 4.9: Comparison of the coefficients  $a_8$  (a),  $b_8$  (b),  $c_{66}$  (c) and  $c_{67}$  (d) at the truth and particle level and when different scenarios are applied at the particle level.

## 4.5 Unfolding

Unfolding [16] refers to the process of estimating a probability distribution in the absence of a known parametric form, especially when data are affected by additional random fluctuations due to limited resolution, limited geometric acceptance of the detector, and reconstruction efficiency effects. This process is essential when comparing measurements with results from other experiments and theoretical predictions of the true distribution, as it corrects distortions caused by specific experimental conditions. In this work, unfolding is used to correct the distortions of the realistic analysis since the entanglement condition is defined on the un-distorted level.

Let's consider a random variable  $y$  and one wants to determine its *probability density function* (PDF)  $f(y)$ . Due to the distortions introduced by the detector effects, the measured value  $x$  of each observation will be different from the truth one of  $y$ , with a distribution  $g(x)$ . The two pdfs can be related as follows through a convolution

$$g(x) = \int R(x|y)f(y)dy \quad (4.12)$$

where  $R(x|y)$  is known as response function. In particle physics, distribution functions are usually histograms obtained by measuring the desired quantity for multiple events. Now assuming an histogram has  $\mathbf{n} = (n_1, \dots, n_N)$  entries per bin subjected to statistical fluctuations, it is possible to define the vectors  $\boldsymbol{\mu} = (\mu_1, \dots, \mu_M)$ , which corresponds to the expectation values for the true histogram of  $y$ , and  $\boldsymbol{\nu} = (\nu_1, \dots, \nu_N)$  which is the vector of the expected number of events in bins of the variable  $x$ . The relation which links these two new variables can be obtained by Eq.(4.12) as

$$\nu_i = \sum_{j=1}^M R_{ij}\mu_j, \quad i = 1, \dots, N \quad (4.13)$$

$R_{ij}$  is called the response matrix and it can be interpreted as the conditional probability

$$R_{ij} = P(\text{observed in bin } i \mid \text{true value in bin } j) \quad (4.14)$$

Therefore, the true distribution is folded with the response function and the goal of the unfolding is to provide an estimate of the true distribution  $f(y)$ . In general, the response matrix is not diagonal and the effect of off-diagonal is to smear out any fine structure leading to bin migration of events. An event generated in a bin  $j$  may be reconstructed in a different bin  $i$  with  $i \neq j$ .

In addition, it must be considered that possible background events  $\boldsymbol{\beta}$  can occur in bin  $i$ . In this analysis, the background effects have been neglected since they are expected to be  $< 15\%$ , using a selection similar to the one described in other analysis [12]. Thus, the equation (4.13) can be rewritten as

$$\boldsymbol{\nu} = R\boldsymbol{\mu} + \boldsymbol{\beta} \quad (4.15)$$

This procedure aims to find an estimator  $\hat{\boldsymbol{\mu}}$  for the true histograms. In this thesis, the method applied for the unfolding is the Iterative Bayesian Unfolding [17], which, as the name suggests, is based on Bayes' theorem. In particular, it is written in terms of independent causes  $C_i$ , corresponding to  $n_i$  events found in the truth bin  $i$  and the subsequent effects  $E_j$ , which can be considered the case where the  $n_j$  events are reconstructed in bin  $j$ . The theorem can be thus written as

$$P(C_i | E_j) = \frac{P(E_j | C_i) \cdot P_0(C_i)}{\sum_{i=1} P(E_j | C_i) \cdot P_0(C_i)} \quad (4.16)$$

where  $P_0(C_i)$  is the prior of the  $i$ -th cause. For the analysis conducted in this thesis, the `Roofold` framework [1] was utilized. This framework implements the Iterative Bayesian Unfolding method discussed earlier. To summarize, in this thesis, the general formula used for the unfolding of the spin density matrix coefficients of the  $WZ$  system is defined as follows:

$$\frac{N_j}{dX_j} = \frac{1}{\Delta X_j} \cdot \frac{1}{f_j^{\text{eff}}} \sum_i M_{ij}^{-1} f_{\text{acc}}^i D^i, \quad (4.17)$$

where  $N_j$  is the number of events of the truth level in the bin  $j$ ,  $X$  represents a generic variable, in this case, the parameters of the density matrix,  $R_{ij}$  is the migration matrix for the unfolding,  $\Delta X_j$  is the width of the bin  $j$  and  $D^i$  represents the number of events observed at the particle level in the  $i$ -th bin. The terms  $f_j^{\text{eff}}$  and  $f_{\text{acc}}^i$  are the efficiency and acceptance factor. The efficiency factor is defined as

$$f_j^{\text{eff}} = \frac{N_{\text{truth \& particle}}^j}{N_{\text{truth}}^j} \quad (4.18)$$

the ratio between the generated events that are observed at the particle level over the total generated events at the truth level, while the acceptance factor is

$$f_{\text{acc}}^i = \frac{N_{\text{truth \& particle}}^i}{N_{\text{particle}}^i} \quad (4.19)$$

is the ratio between the events generated that would pass both parton and particle level criteria divided by the number of events at the particle level. In this analysis, the acceptance is expected to be equal to one since there are no requirements at parton level. This is not the case for some studies in dedicated regions of the phase space, where the parton level selection is included. In addition, the Iterative Bayesian Unfolding algorithm requires a regularisation parameter to prevent the statistical fluctuations from being interpreted as structure in the true distribution. The degree of regularization applied in this method is controlled by the number of iterations, which has been set to 2 for this analysis.

Figure 4.10 displays the example of the response matrix for  $a_1$  and  $b_5$  spin density matrix coefficients used for the unfolding at the particle level and the efficiency of the same coefficients for each bin. This is obtained only by including events passing the particle-level requirements, so only the effects due to the mis-reconstruction are included. The non-flat efficiency will correct for the distortions caused by events not passing the selection.

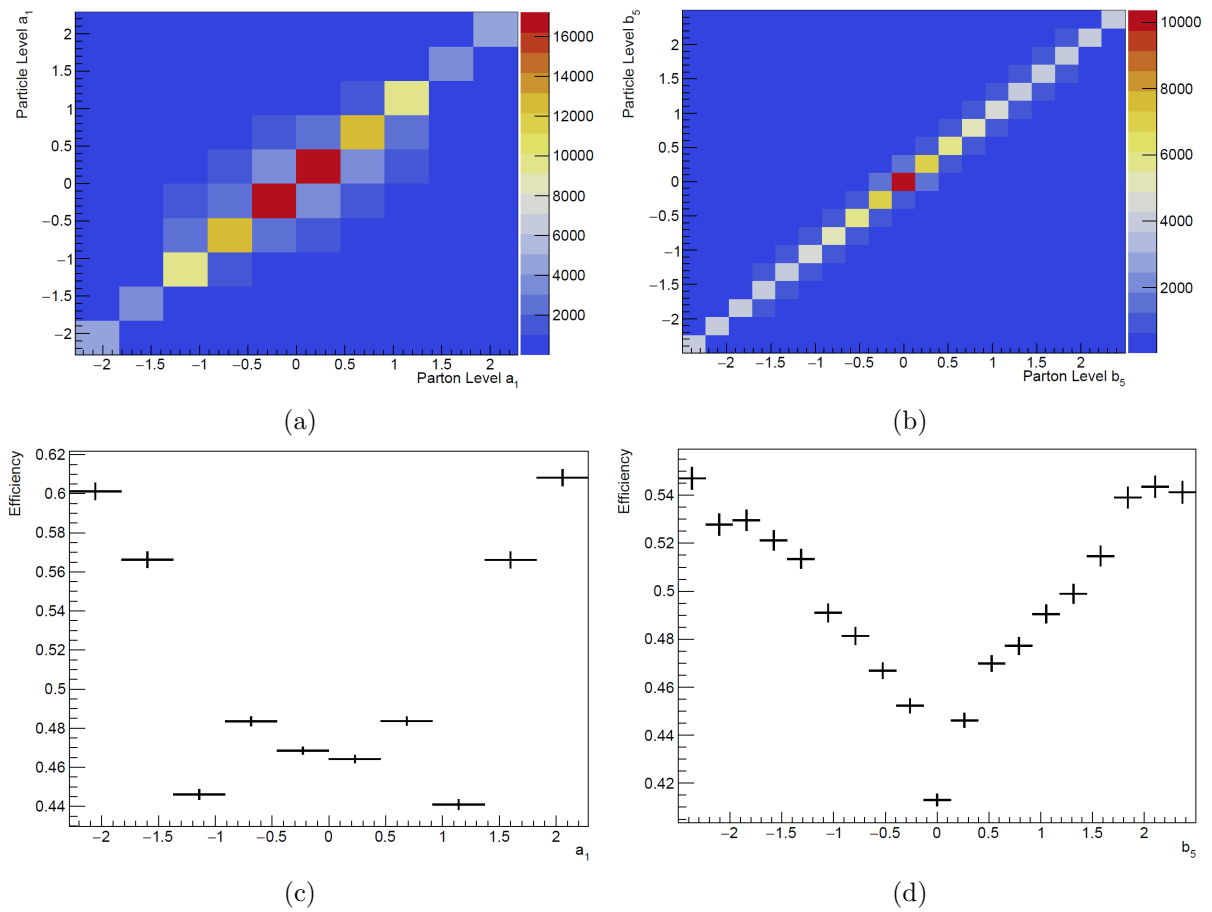


Figure 4.10: Response matrix for the coefficients  $a_1$  (a) and  $b_5$  (b) of the spin density matrix and the efficiency corrections for the parameter  $a_1$  and  $b_5$  used for the unfolding.

## 4.6 Bootstrap method

One of the hardest aspects when performing measurements in particle physics is the evaluation of the statistical uncertainties. This task becomes particularly complex when intricate methodologies are necessary due to potential correlations between events in related measurements or the migration of events across different data bins. In these cases, the formulas used to calculate statistical uncertainties may become unreliable or excessively complicated to evaluate or propagate. An example of this challenging issue is the determination of uncertainties when employing unfolding techniques like the Iterative Bayesian Unfolding introduced in the previous section.

In this thesis, the key quantity, that will be discussed in the next section, is the lower bound of the concurrence which is crucial to understand the level of entanglement of the  $WZ$  diboson system. The  $c_{MB}^2$ , as defined in Eq.(3.38), depends on the 80 coefficients of the spin density matrix for a  $WZ$  diboson system of Eq.(3.13). Each coefficient is calculated employing the simulated dataset, as a consequence non-trivial correlations exist among the various coefficients. In addition, when considering the realistic analysis, unfolding needs to be applied leading to an increase in correlation among the bins of the distributions and making also the estimate of the uncertainty for a single coefficient complicated. Therefore the method employed to estimate the expected uncertainty on  $c_{MB}^2$  must take into account both the correlations among the coefficients and the effects induced by the unfolding.

A powerful technique used to evaluate measurement uncertainties is the well-known Bootstrap Method [19, 20]. Let's consider an analysis where events from a statistical process are collected in a dataset that is analyzed to obtain a measurement of a certain physical quantity. The bootstrap method involves generating multiple "resampled" datasets by randomly drawing with replacements from the original dataset as shown in Figure 4.11. Each resampled dataset, or replica, maintains the same size as the original dataset but may include duplicate entries because of the replacement. This process simulates conducting multiple experiments to determine the distribution of the quantity of interest. By calculating the desired measurement for each resampled dataset, a distribution of the statistic is obtained. Therefore, this bootstrap distribution can be used to estimate the statistical uncertainty of the studied physical quantity.

Specifically in this analysis, a variation of the bootstrap method has been used where the resampling of the dataset is performed using a Poisson distribution with a mean equal to one defined as follows

$$P(w; \lambda = 1) = \frac{\lambda^w e^{-\lambda}}{w!} = \frac{e^{-1}}{w!} \quad (4.20)$$

where  $\lambda = 1$  is the mean of the distribution and  $w$  is the number of occurrence. This choice of distribution for the bootstrap method has been applied since in collider experiments like ATLAS and CMS, the size of the dataset is itself a Poisson variable. In

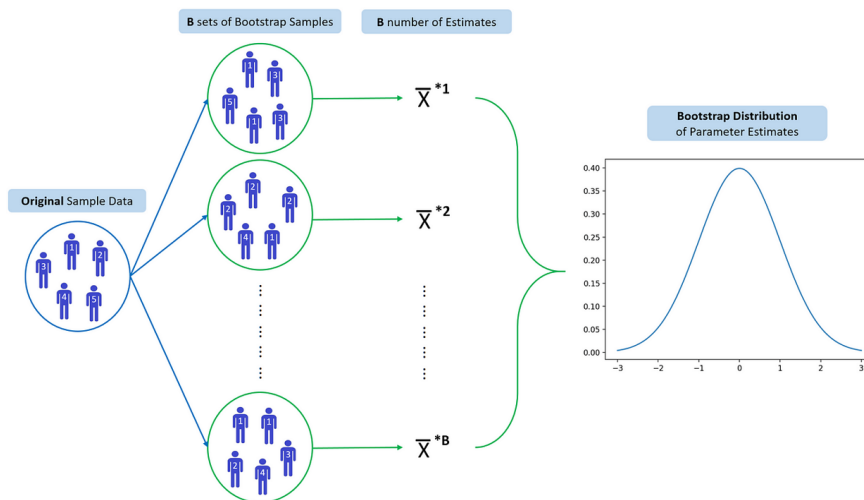


Figure 4.11: Schematic representation of the bootstrap method.

particular, each event in the nominal dataset is assigned a Poisson weight, with possible weights of  $w = 0, 1, 2, 3$ , and their probabilities of occurrence are provided in Table 4.4.

Weight	P(w)
0	0.368
1	0.368
2	0.184
3	0.061
4	0.015

Table 4.4: Probabilities of Poisson distribution for different weights.

From the table can be seen that a weight of 0, which occurs with a probability of 36.8%, removes an event from the bootstrap replicas, while in the case of  $w = 3$ , the events would be selected 3 times. As a result, the size of the resulting bootstrap samples follows a Poisson distribution, with the mean corresponding to the number of events in the original dataset. This is because the sum of independent Poisson variables also follows a Poisson distribution, with its mean equal to the sum of the individual means. In this analysis, the number of copies of the original dataset has been set to  $N_{sample} = 100$ . The exact way bootstrap replicas are employed in determining the uncertainty on the parton level and unfolded concurrence will be explained in the next section.

## 4.7 Measurement of the Concurrence

The coefficients of the spin density matrix computed in the previous section will now be used to measure the lower bound of the concurrence, a key quantum observable in this analysis for determining whether the  $WZ$  diboson system is entangled. The lower bound of the concurrence for the matrix 3.13 obtained by quantum state tomography can be measured using the following equation:

$$c_{MB}^2 = -\frac{4}{9} - \frac{2}{3} \sum_{i=1}^8 a_i^2 - \frac{2}{3} \sum_{j=1}^8 b_j^2 + 8 \sum_{i,j=1}^8 c_{ij}^2. \quad (4.21)$$

Firstly, the lower bound was calculated at the parton level using events generated through Monte Carlo simulation without any selection criteria. Figure 4.8a shows the coefficients used for this measurement. The result of the theoretical predictions obtained using the parton level dataset is

$$c_{MB}^2 = 0.0361 \pm 0.0175. \quad (4.22)$$

This value was obtained using the bootstrap method outlined in Section 4.6. In particular, the number of samples (or replicas) in this analysis was set to  $N_{sample} = 100$ . For each bootstrap sample,  $c_{MB}^2$  was calculated using Eq.(4.21), and the final result was determined by averaging the concurrence values across all replicas, as shown in Figure 4.12. The statistical error in the lower bound was determined by calculating the standard deviation of the concurrence distribution across the bootstrap replicas. The actual uncertainty on the concurrence is determined by the number of simulated events, not by the number of replicas, which are only used to estimate the uncertainty. In this case, around 300,000 events were simulated, roughly corresponding to the number expected at the LHC with a luminosity of  $450 \text{ fb}^{-1}$ .

Let's note that the lower bound value of the concurrence is positive. As described in Chapter 3, this indicates that on average the  $WZ$  diboson system is generated as entangled. Another point to be noticed is that the value of the concurrence is quite close to zero and at less than  $3\sigma$  to zero, considering the parton level uncertainty, which represents the statistical uncertainty expected for a perfect measurement. This suggests that measuring a  $c_{MB}^2$  different from zero across the entire  $WZ$  phase space will be challenging. However, this finding is consistent with the last row of Table 3.1, where a Monte Carlo simulation was used to study the theoretical prediction of the specific decay  $pp \rightarrow W^+Z \rightarrow e^+\nu_e \mu^+\mu^-$ , confirming the potential for an inclusive measurement of entanglement of  $WZ$  system in  $pp$  collisions.

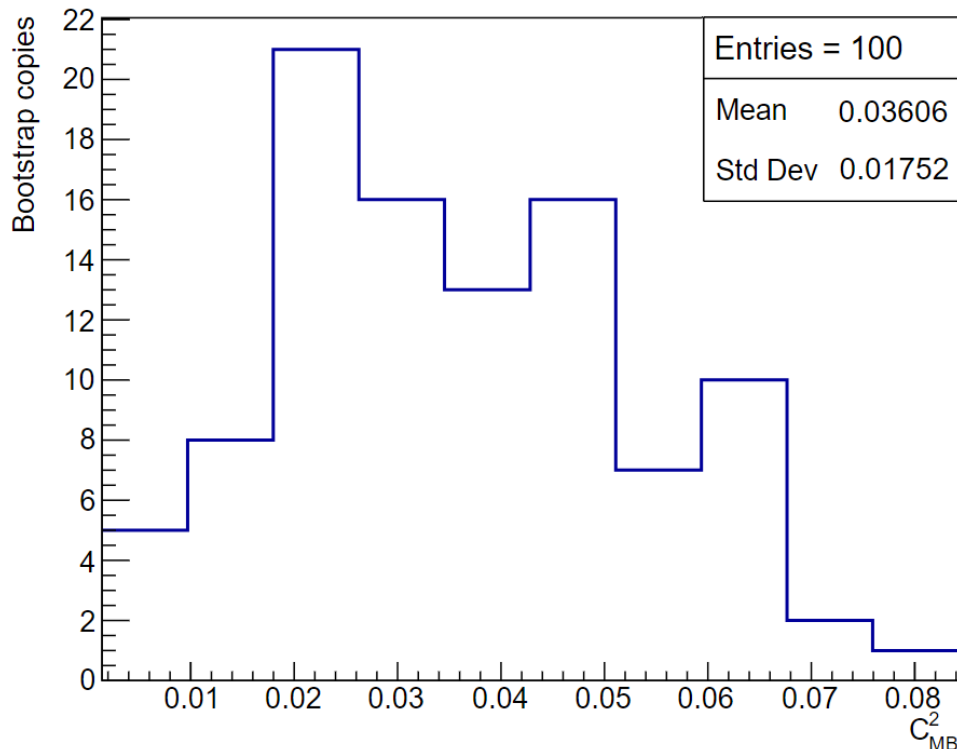


Figure 4.12: Distribution of the concurrence at parton level obtained through the bootstrap method with  $N_{sample} = 100$ .

The next step in the analysis involves measuring the  $c_{MB}^2$  at LHC. This is a key result in this thesis, marking the first feasibility study of the entanglement of the  $WZ$  system, that accounts for realistic selection and reconstruction effects. In fact, at the particle level, selections are applied to simulate detector effects, such as limited acceptance of the reconstructed quantities. Therefore, this measurement can be used to determine if this type of entanglement study is feasible for detectors like ATLAS and CMS and identify the primary limitations involved. The lower bound of the concurrence obtained including detector effects as described in Section 4.2 is

$$c_{MB}^2 = 0.0459 \pm 0.0305. \quad (4.23)$$

This result has been obtained through three fundamental steps. First, the lower bound was calculated at the particle level using a bootstrap method, similar to the approach used at the parton level. In this step, the number of samples was fixed at  $N_{sample} = 100$  to determine the mean value and its standard deviation. However, the value of the concurrence obtained from this computation would present the same issue of the spin density matrix coefficients described in Section 4.4. Specifically, the parameters of the density matrix need to be unfolded to reduce the effects induced by the imperfect

measuring devices. The second step, therefore, consists of applying the Iterative Bayesian Unfolding technique depicted in Section 4.5 through `RooUnfold` framework to the 80 coefficients in all the bootstrap copies. In the final step, the unfolded bootstrap samples are then utilized to determine the distribution of  $c_{MB}^2$ , from which an estimate of the mean and its associated uncertainty can be derived. In particular, each bootstrap replica was unfolded using the original dataset at the particle level as the true distribution for constructing the response matrix, as used in calculating the spin density matrix coefficients in Section 4.4. From this process, the newly unfolded parameters of each bootstrap sample were used to compute the unfolded  $c_{MB}^2$  for each replica. The results are shown in Figure 4.13.

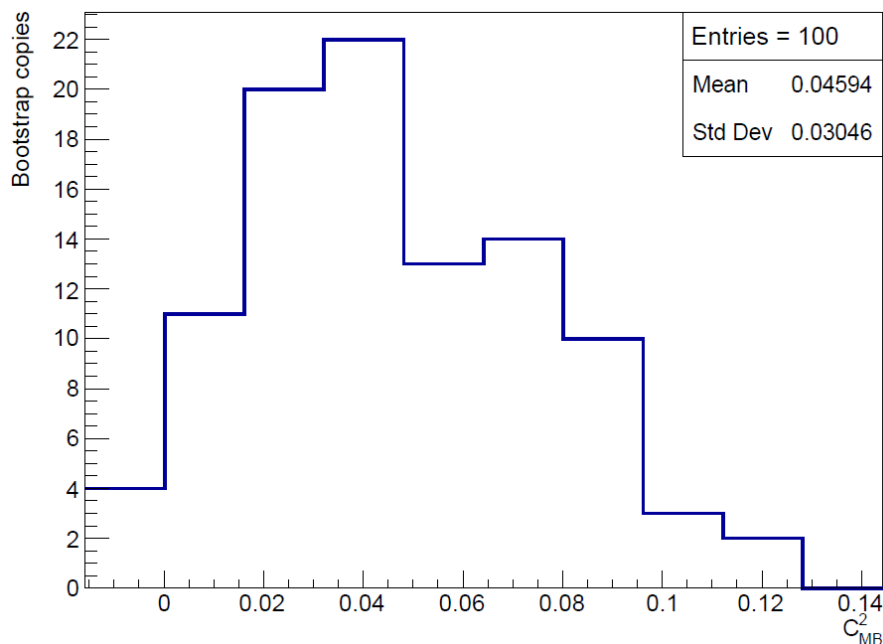


Figure 4.13: Distribution of the concurrence at particle level after the unfolding obtained through the bootstrap method with  $N_{sample} = 100$ .

Therefore the result presented in Eq.(4.23) represents the mean value of the distribution 4.13, which depicts the lower bound of the concurrence across all bootstrap copies. The statistical error, which takes into account the effects due to selections, reconstruction and unfolding is given by the standard deviation of the concurrence distribution.

The concurrence results obtained at both the parton and particle levels in Eq.(4.22-4.23) are inclusive measurements, accounting for the entire phase space region. The two values obtained at different levels are compatible but not identical, which is attributed to the statistical independence of the measurements. The results obtained at both levels are very small and considering their uncertainties the values obtained have a low significance

with a number of sigmas from the entanglement limit smaller than three. In particle physics, a phenomenon is considered evidence when it reaches a significance level of  $3\sigma$ , while a significance of  $5\sigma$  is required to claim the discovery of a new phenomenon. In particular, this suggests that detecting the entanglement of the  $WZ$  system at LHC inclusively using data from Run 2 and 3 would be very challenging.

### 4.7.1 Concurrence in different phase space regions

As discussed in the previous section, the observation of the entanglement of the  $WZ$  diboson system would be difficult based on the result of the concurrence obtained previously in the inclusive region. Therefore, an additional study has been conducted to investigate the  $W^\pm Z \rightarrow l\nu ll$  process across different phase space regions with specific selections to observe how the lower bound of the concurrence varies. In particular, in this part of the analysis, the focus was moved to the  $W$  and  $Z$  bosons by applying cuts mainly on two specific physical quantities: the invariant mass of the diboson system and the emission angle  $\theta_{CM}$  of the  $W^\pm$  boson relative to the proton beam in the centre-of-mass frame. The choice of these regions has been made following the analysis performed in [5]. Figure 4.14 shows the distributions of these two quantities at parton level. These plots show that most of the events generated at the truth level are concentrated in the region where the  $W^\pm$  boson is emitted near the proton beam, with  $|\cos\theta_{CM}|$  close to one. Additionally, the majority of events occur in a region where the invariant mass of the diboson system is between 200 and 400 GeV.

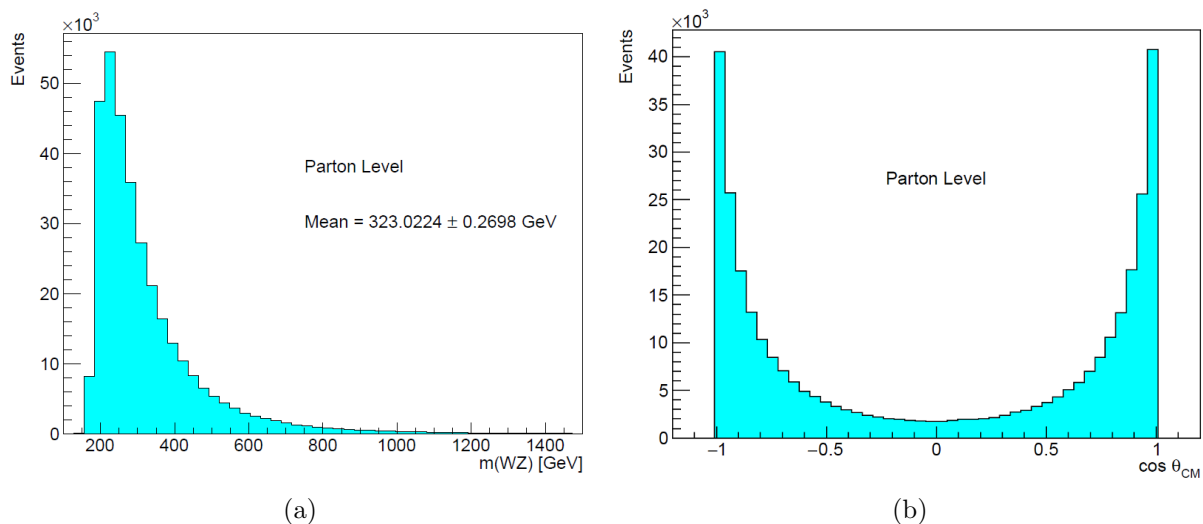


Figure 4.14: Distribution at the parton level of the invariant mass of the  $WZ$  system (a) and the emission angle  $\theta_{CM}$  (b) of the  $W^\pm$  boson relative to the proton beam in the  $WZ$  centre-of-mass.

For this study, the theoretical prediction of the concurrence was computed in four different regions as a function of the emission angle  $\theta_{CM}$  and the invariant mass of the  $WZ$  system. This computation has been performed first at the truth level obtaining the histogram shown in Figure 4.15.

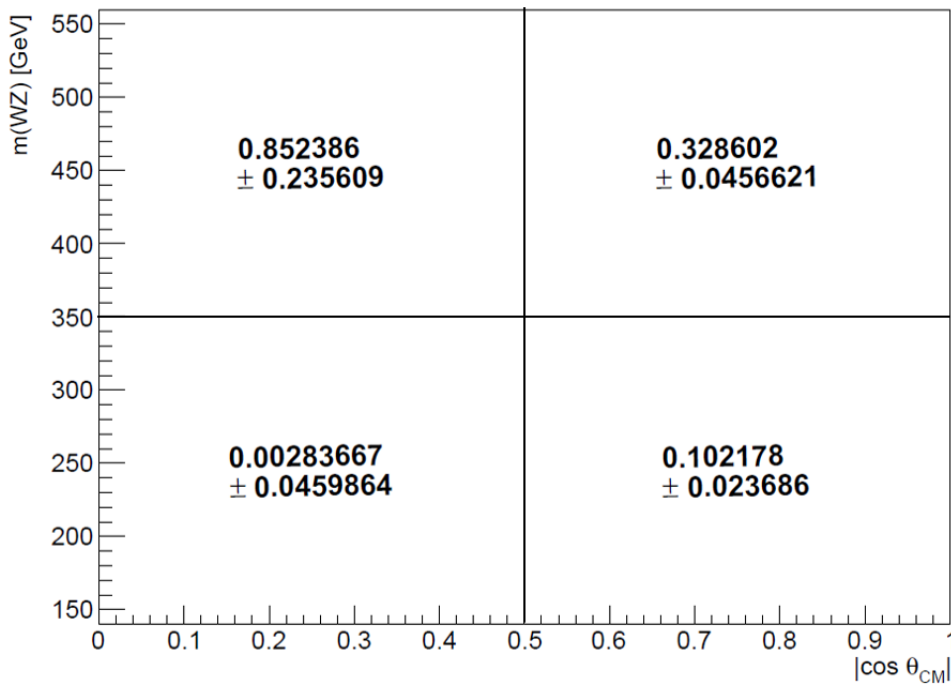


Figure 4.15: Measurement of the concurrence at parton level in different regions as function of the emission angle  $\theta_{CM}$  and the invariant mass of the  $WZ$  system. Specifically, for each bin, the x-axis represents the cosine of  $\theta_{CM}$ , while the value on the y-axis is a lower bound  $m(WZ)$  on the invariant mass of the diboson pair.

The plot shows that the concurrence for events emitted at a small  $\theta_{CM}$  angle relative to the proton beam is higher than that of the inclusive measurement, with greater statistical significance. This region of the  $\theta_{CM}$  angle also contains the majority of simulated events, as can be inferred from Figure 4.14b. In the region of small  $|\cos \theta_{CM}|$ , the concurrence is consistent with zero in the inclusive region of the invariant mass, while in the region with events with a  $m(WZ) > 350$  GeV, the lower bound of the concurrence approaches one, though with high statistical uncertainty due to the limited statistics, as illustrated in Figures 4.14.

Encouraged by the result obtained by the analysis in different phase space regions at parton level, the study was extended to the particle level, which accounts for detector effects, to determine whether the entanglement of the  $WZ$  system can be detected by ATLAS and CMS using data from the Run 3. Following the application of the unfolding technique described in Section 4.5 to remove effects due to the selection and reconstruc-

tion, the lower bound of the concurrence  $c_{MB}^2$  at particle level is presented in Figure 4.16.

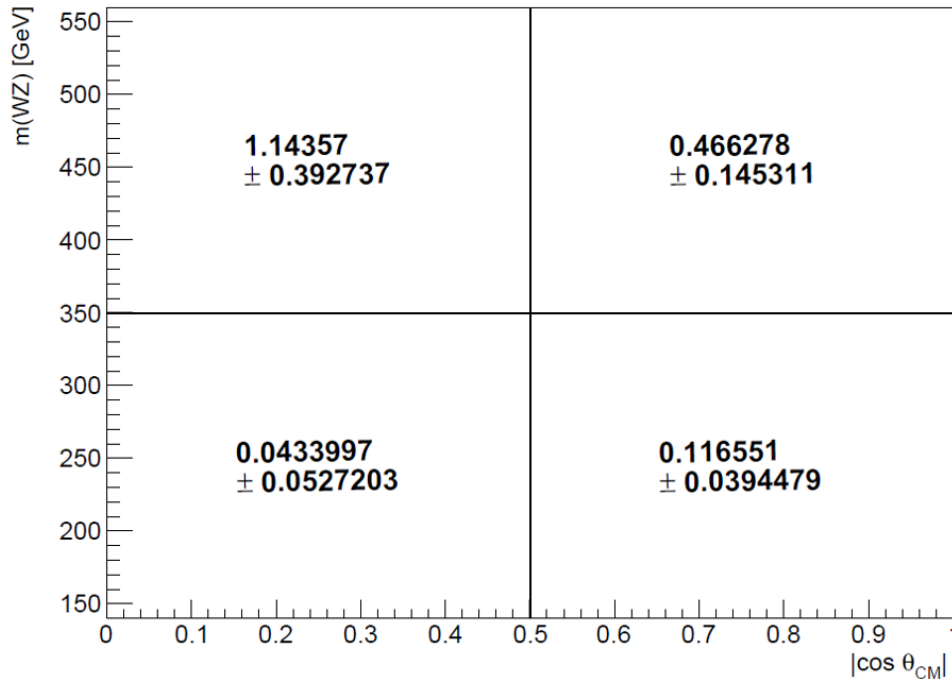


Figure 4.16: Measurement of the concurrence at particle level in different regions as function of the emission angle  $\theta_{CM}$  and the invariant mass of the  $WZ$  system. Specifically, for each bin, the x-axis represents the cosine of  $\theta_{CM}$ , while the value on the y-axis is a lower bound  $m(WZ)$  on the invariant mass of the diboson pair.

The plot at particle level shows similarities to the parton level case. In particular, in the region where  $|\cos \theta_{CM}| > 0.5$ , the concurrence value increases compared to the lower bound of Eq.(4.23). However, it can be noticed that the statistical error in these results is larger than at the parton level, as it also accounts for the detector's limited acceptance and the resolution of the reconstructed quantities. In this region, evidence of the entanglement of the  $WZ$  system could be obtained at LHC with a significance of  $3\sigma$ , in particular in the region with a lower bound on the  $m(WZ)$  of 350 GeV. Similar to the parton level, the lower bound of the concurrence can reach a negative value in regions of small  $|\cos \theta_{CM}|$  when considering events with an arbitrary invariant mass. However, for events with  $m(WZ) > 350$  GeV, the concurrence calculated in this analysis would exceed the theoretical maximum value of  $\frac{4}{3}$ . Nevertheless, this outcome can be attributed to the limited statistics of events in this particular region.

### 4.7.2 Transverse momentum selection

The observation of the entanglement of the  $WZ$  system at the LHC, as it has been presented previously, can be very challenging as inclusive measurement and even in different phase space regions, as shown in Figure (4.15-4.16), only evidence of the entanglement can be measured with a significance around  $3\sigma$ . Therefore, the same analysis presented in the previous sections has been refined introducing an additional selection on the total transverse momentum of the  $WZ$  system. In particular, the total  $p_T^{WZ}$  of the diboson system has been calculated in the laboratory frame. Theoretically, from the conservation of momenta, the value of this physical quantity should be zero because the protons in the beam collide head-on. However, the total transverse momentum of the  $WZ$  system both at the parton and particle level follows the distribution displayed in Figure 4.17.

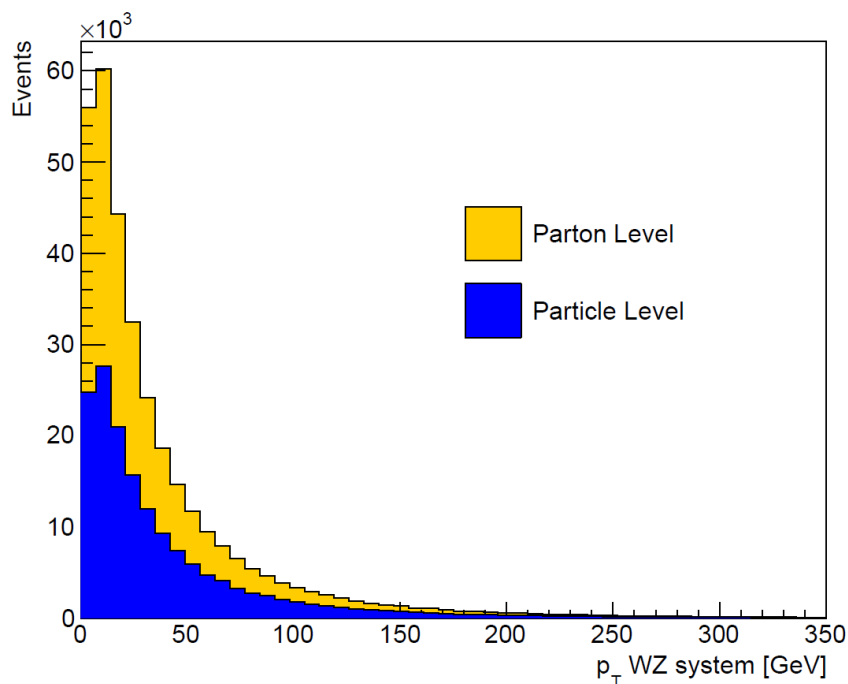


Figure 4.17: Distribution of the total transverse momentum  $p_T$  of the  $WZ$  system obtained in the laboratory frame.

This effect can be caused by the emission of hard photons from the  $W$  and  $Z$  bosons during their propagation before the decay into leptons, causing a loss of energy of the boson which results in a total transverse momentum of the system different from zero. Additionally, a similar effect can arise from the radiation of gluons from the initial state during the propagation of heavy vector bosons, although this does not impact the entanglement.

As a consequence, this process could spoil the measurement of the entanglement

in the  $WZ$  system by modifying the correlation between the two heavy vector bosons. Therefore, based on the distribution of Figure 4.17, an addition cut was applied to the analysis requiring a  $p_T^{WZ} < 40$  GeV, where  $p_T^{WZ}$  is the total transverse momentum of the  $WZ$  system calculated in the laboratory frame. Firstly, the selection was applied at parton level to determine if the theoretical prediction on the concurrence could be improved compared to the inclusive measurement obtained in Eq.(4.22). The following analysis has been performed using the same procedure displayed for the measurement in the inclusive region, employing the bootstrap method to compute the result. The lower bound of the concurrence at the truth level with a selection of  $p_T^{WZ} < 40$  GeV is

$$c_{MB}^2 = 0.0811 \pm 0.0219 \quad (4.24)$$

When compared to the lower bound of the concurrence in the inclusive region,  $c_{MB}^2 = 0.0361 \pm 0.0175$ , this result shows several differences. Notably, the mean value of the concurrence has increased, approaching 0.1. Additionally, while the uncertainty—calculated as the statistical error of the distribution—has slightly increased, the significance of the result has improved, reaching nearly  $4\sigma$ . In contrast, the significance was approximately  $2\sigma$  in the inclusive measurement at the truth level.

Let's now consider the analysis of the lower bound of the concurrence at the particle level. The result presented in Eq.(4.23), has a very low significance in the inclusive region, which implies that measuring the entanglement of the  $WZ$  system at LHC with the current dataset would be difficult. Therefore, to improve this feasibility study, the condition of  $p_T^{WZ} < 40$  GeV was imposed on the events of the available dataset from MC simulation and the result obtained for the concurrence is the following

$$c_{MB}^2 = 0.0994 \pm 0.0365 \quad (4.25)$$

The lower bound calculation has been performed using the unfolding technique and bootstrap method explained in Section 4.7 at the particle level. By excluding from the analysis events in which the  $W$  or  $Z$  boson emitted high energy photons, it was observed that the value of the concurrence, which distribution is illustrated in Figure 4.18, has increased. Consequently, the significance has risen to nearly  $3\sigma$ , close to the threshold required to claim evidence of the result.

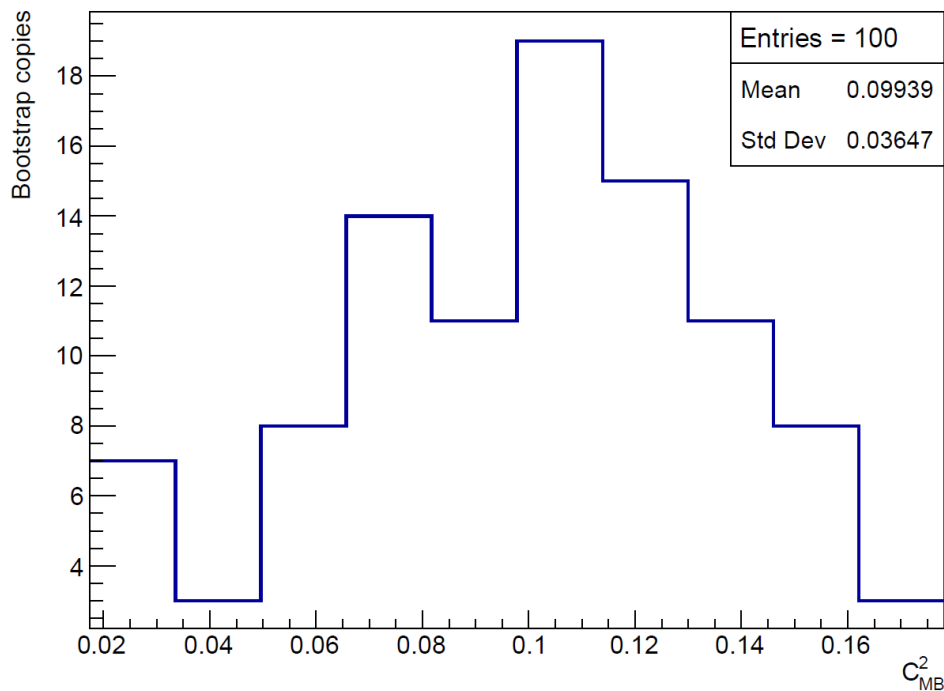


Figure 4.18: Distribution of the concurrence at particle level after the unfolding obtained through the bootstrap method with  $N_{sample} = 100$  with the selection of  $p_T^{WZ} < 40$  on the total transverse momentum of the  $WZ$  system.

The analysis conducted at both parton and particle levels, using the total transverse momentum selection, reveals a promising lower bound for the concurrence. Therefore, different regions of the phase space have been investigated for the  $WZ$  decay process with this specific cut. In particular, the study continued focusing on examining the behaviour of the lower bound of the concurrence at different emission angles  $\theta_{CM}$  of the charged vector boson and invariant mass of the  $WZ$  diboson system, similar to the approach taken in the previous section. The results of the concurrence as a function of the emission angle of the  $W$  boson and the invariant mass of the  $WZ$  system are presented in Figure 4.19.

From the plot in Figure 4.18 some consideration of the selection of the transverse momentum can be made. As for the analysis presented in Section 4.7.1, in the region where  $W$  bosons have an emission angle such that the  $|\cos \theta_{CM}| > 0.5$ , the lower bound of the concurrence has increased reaching a significance around  $3.5\sigma$ , indicating the evidence of the entanglement in  $WZ$  system can be measured using Run 3 events with this selection in specific region of the phase space. This study currently does not account for the systematic uncertainties associated with the objects used in the analysis. However, considering the high precision achieved at the LHC in measuring charged leptons,

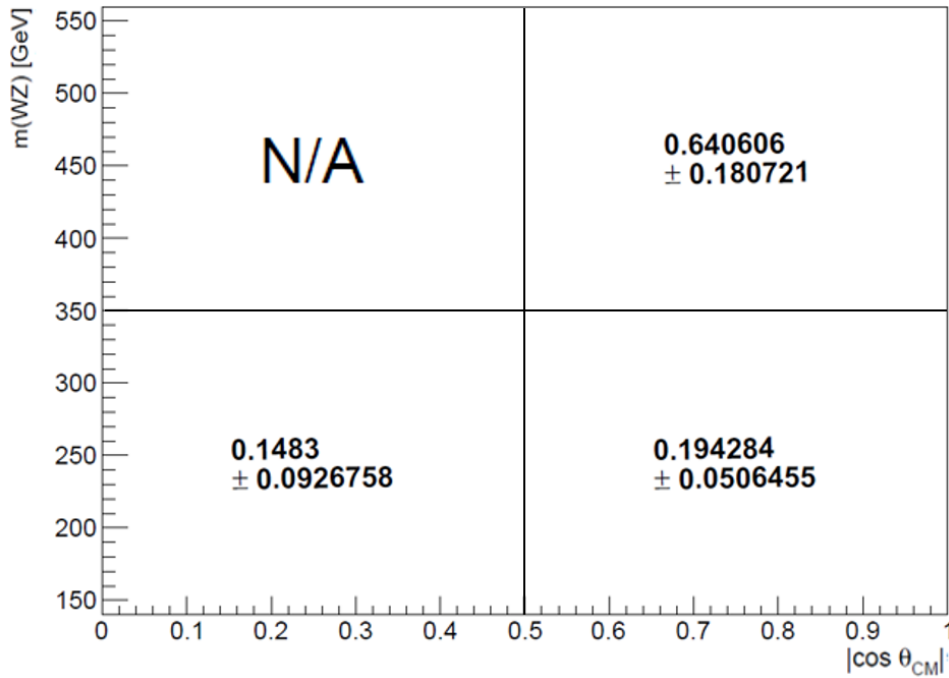


Figure 4.19: Measurement of the concurrence with a selection on the total transverse momentum of the  $WZ$  system of  $p_T^{WZ} < 40$  GeV at particle level in different regions of phase space. This is analyzed as function of the emission angle  $\theta_{CM}$  and the invariant mass of the  $WZ$  system.

these systematic uncertainties are expected to be smaller compared to the statistical uncertainties. In the top-left region of Figure 4.19, the value of the lower bound is not available due to the limited statistics of events in that region, which, as can be pointed out from Figure 4.14, do not contain the majority of the processes.

# Conclusions

This thesis presents the first feasibility study for the measurement of the quantum correlation of the  $W^\pm Z$  system produced in a proton-proton collision at the Large Hadron Collider. In particular, this work provides the first realistic study of the entanglement of this specific diboson system, which takes into account effects due to limited acceptance of the detector, distortions caused by the reconstruction and the effects on the uncertainties and the distortions caused by the reconstruction. The analysis is performed at the truth level and particle level by studying the following events

$$pp \rightarrow W^\pm Z \rightarrow l'^\pm \nu l^+ l^-, \quad (4.26)$$

which are generated through Monte Carlo simulation with a number of events equivalent to the luminosity  $L = 450 \text{ fb}^{-1}$  of Run 2 and Run 3 of the LHC at a centre of mass energy  $\sqrt{s} = 13 \text{ TeV}$ . The key quantum observable calculated in this analysis is the lower bound of the concurrence, which is used to determine the entanglement of the quantum state composed by the  $W$  and the  $Z$  bosons. The lower bound is defined mathematically in Eq.(3.38) and depends on the 80 coefficients of the spin density matrix of the diboson system in Eq.(3.13). The calculation was first performed at the parton level to be able to validate the theoretical predictions, and then including selections and reconstruction effects to evaluate the feasibility of this measurement for the ATLAS and CMS detectors. In this case, an unfolding technique was applied to all the distributions used to derive  $c_{MB}^2$  to recover the parton level value. The lower bounds of the concurrence obtained as inclusive measurements are the following

$$\begin{aligned} \text{Parton Level : } c_{MB}^2 &= 0.0361 \pm 0.0175 \text{ (stat.)}, \\ \text{Unfolded Level : } c_{MB}^2 &= 0.0459 \pm 0.0305 \text{ (stat.)}. \end{aligned} \quad (4.27)$$

The results are consistent, demonstrating the capability of the method to reconstruct this complex observable. However, the significance is low even at the parton level, which ideally represents a perfect detector. The situation deteriorates further when considering the lower bound of the concurrence at the unfolded level, where uncertainties increase due to detector effects. This suggests that observing entanglement in the inclusive region using data from Run 3 would be challenging. To address this, additional studies were performed to explore entanglement under different selections and in various regions,

examining their impact on concurrence. When selecting events with a total transverse momentum of the diboson system of  $p_T^{WZ} < 40$  GeV, the concurrence calculated at both the parton and unfolded levels is:

$$\begin{aligned} \text{Parton Level : } c_{MB}^2 &= 0.0811 \pm 0.0219 \text{ (stat.)}, \\ \text{Unfolded Level : } c_{MB}^2 &= 0.0994 \pm 0.0365 \text{ (stat.)}. \end{aligned} \tag{4.28}$$

With this new selection, the lower bound of the concurrence has increased, approaching a significance of  $3\sigma$ , which is close to the threshold for claiming evidence of the result.

Additionally, the concurrence has been analyzed in different phase space regions, as detailed in Sections 4.7.1 and 4.7.2. In particular, it has been shown that the concurrence increases when considering events with an invariant mass  $m(WZ) > 350$  GeV and a  $|\cos\theta_{CM}|$  of the emission angle of the  $W^\pm$  boson close to one. In particular, when considering events with a cut on the total transverse momentum of the diboson system of  $p_T^{WZ} < 40$  GeV, the unfolded  $c_{MB}$  reached a value of:

$$c_{MB}^2 = 0.641 \pm 0.181 \tag{4.29}$$

which has a significance exceeding  $3.5\sigma$ .

In conclusion, this type of analysis on the  $WZ$  system is highly complex as it involves the measurements of 80 different coefficients to determine the spin density matrix. Even with the fully leptonic decay channel used in this thesis, significant discrepancies are observed between the coefficients derived including detector effects and their theoretical values. This can be attributed to the presence of the neutrino which introduces additional challenges due to its reconstruction and the limited acceptance of the detector. Therefore, a specialized method is needed to correct and refine the measurements of these observables. The results obtained give hints about the effective possibility of measuring entanglement between the  $W$  and  $Z$  boson, however with the current dataset of Run 3 it would be very challenging due to the low level of entanglement expected in this final state, compared to the statistical uncertainty. The analysis also reveals that in specific regions of phase space, there may be stronger correlations between the two heavy vector bosons, as indicated in Eq.(4.29).

The  $c_{MB}^2$  for the  $WZ$  system, which has never been measured before, even if it doesn't result in the observation of entanglement between the two heavy vector bosons could still be used as a new powerful tool in the search for new physics [4].

# Bibliography

- [1] Tim Adye. “Proceedings of the PHYSTAT 2011 Workshop on Statistical Issues Related to Discovery Claims in Search Experiments and Unfolding”. In: *PHYSTAT 2011 Workshop on Statistical Issues Related to Discovery Claims in Search Experiments and Unfolding*. Ed. by H. B. Prosper and L. Lyons. CERN-2011-006. CERN, Geneva, Switzerland: CERN, Jan. 2011, pp. 313–318.
- [2] Sukhpal Singh Gill et al. *Quantum Computing: Vision and Challenges*. 2024. arXiv: 2403.02240 [cs.DC]. URL: <https://arxiv.org/abs/2403.02240>.
- [3] J. Alwall et al. “The automated computation of tree-level and next-to-leading order differential cross sections, and their matching to parton shower simulations”. In: *Journal of High Energy Physics* 2014.7 (2014). ISSN: 1029-8479. DOI: 10.1007/jhep07(2014)079. URL: [http://dx.doi.org/10.1007/JHEP07\(2014\)079](http://dx.doi.org/10.1007/JHEP07(2014)079).
- [4] Rafael Aoude et al. *Probing new physics through entanglement in diboson production*. 2023. arXiv: 2307.09675 [hep-ph]. URL: <https://arxiv.org/abs/2307.09675>.
- [5] Rachel Ashby-Pickering, Alan J. Barr, and Agnieszka Wierzychucka. “Quantum state tomography, entanglement detection and Bell violation prospects in weak decays of massive particles”. In: *Journal of High Energy Physics* 2023.5 (2023). ISSN: 1029-8479. DOI: 10.1007/jhep05(2023)020. URL: [http://dx.doi.org/10.1007/JHEP05\(2023\)020](http://dx.doi.org/10.1007/JHEP05(2023)020).
- [6] Reinhold A. Bertlmann and Philipp Krammer. “Bloch vectors for qudits”. In: *Journal of Physics A: Mathematical and Theoretical* 41.23 (2008), p. 235303. DOI: 10.1088/1751-8113/41/23/235303. URL: <https://doi.org/10.1088/1751-8113/41/23/235303>.
- [7] Christian Bierlich et al. *A comprehensive guide to the physics and usage of PYTHIA 8.3*. 2022. arXiv: 2203.11601 [hep-ph]. URL: <https://arxiv.org/abs/2203.11601>.

- [8] Christian Bierlich et al. “Robust Independent Validation of Experiment and Theory: Rivet version 3”. In: *SciPost Physics* 8.2 (2020). ISSN: 2542-4653. DOI: 10.21468/scipostphys.8.2.026. URL: <http://dx.doi.org/10.21468/SciPostPhys.8.2.026>.
- [9] John M. Campbell, Richard K. Ellis, and C. Williams. “Vector boson pair production at the LHC”. In: *Journal of High Energy Physics (JHEP)* 07 (2011). arXiv:1105.0020 [hep-ph]. arXiv: 1105.0020 [hep-ph].
- [10] NNPDF Collaboration. “Parton distributions from high-precision collider data”. In: *The European Physical Journal C* 77.663 (Oct. 2017). DOI: 10.1140/epjc/s10052-017-5199-5. URL: <https://link.springer.com/article/10.1140/epjc/s10052-017-5199-5>.
- [11] The ATLAS Collaboration. “Electron and photon efficiencies in LHC Run 2 with the ATLAS experiment”. In: *Journal of High Energy Physics* 2024.5 (2024). ISSN: 1029-8479. DOI: 10.1007/jhep05(2024)162. URL: [http://dx.doi.org/10.1007/JHEP05\(2024\)162](http://dx.doi.org/10.1007/JHEP05(2024)162).
- [12] The ATLAS Collaboration. “Measurement of  $W^\pm Z$  production cross sections and gauge boson polarisation in pp collisions at  $\sqrt{s} = 13$  TeV with the ATLAS detector”. In: *The European Physical Journal C* 79 (2019). ISSN: 1434-6052. DOI: 10.1140/epjc/s10052-019-7027-6. URL: <http://dx.doi.org/10.1140/epjc/s10052-019-7027-6>.
- [13] The ATLAS Collaboration. “Measurement of the  $W+W$  production cross section in pp collisions at a centre-of-mass energy of  $\sqrt{s} = 13$  TeV with the ATLAS experiment”. In: *Physics Letters B* 773 (2017). ISSN: 0370-2693. DOI: 10.1016/j.physletb.2017.08.047. URL: <http://dx.doi.org/10.1016/j.physletb.2017.08.047>.
- [14] The ATLAS Collaboration. “Measurement of  $ZZ$  production in the  $\ell\nu\nu$  final state with the ATLAS detector in pp collisions at  $\sqrt{s} = 13$  TeV”. In: *Journal of High Energy Physics* 2019.10 (2019). ISSN: 1029-8479. DOI: 10.1007/jhep10(2019)127. URL: [http://dx.doi.org/10.1007/JHEP10\(2019\)127](http://dx.doi.org/10.1007/JHEP10(2019)127).
- [15] John C. Collins, David E. Soper, and George F. Sterman. “Factorization of Hard Processes in QCD”. In: *Advances in Series on High Energy Physics* 5 (1989). arXiv:hep-ph/0409313 [hep-ph], pp. 1–91. arXiv: hep-ph/0409313 [hep-ph].
- [16] Glen Cowan. *Statistical Data Analysis*. Oxford: Clarendon Press, 1998. ISBN: 978-0198501558.
- [17] G. D’Agostini. *Improved iterative Bayesian unfolding*. 2010. arXiv: 1010.0632 [physics.data-an]. URL: <https://arxiv.org/abs/1010.0632>.

- [18] S. D. Drell and T.-M. Yan. “Partons and their applications at high energies”. In: *Annals of Physics* 66.2 (1971), pp. 578–623. URL: <http://www.sciencedirect.com/science/article/pii/0003491671900716>.
- [19] Bradley Efron. “Bootstrap methods: another look at the jackknife”. In: *The Annals of Statistics* 7.1 (1979), pp. 1–26. DOI: 10.1214/aos/1176344552.
- [20] Bradley Efron and Robert J. Tibshirani. *An Introduction to the Bootstrap*. 1st. Chapman and Hall/CRC, 1994. DOI: 10.1201/9780429246593.
- [21] A. Einstein, B. Podolsky, and N. Rosen. “Can Quantum-Mechanical Description of Physical Reality Be Considered Complete?” In: *Physical Review* 47 (1935), pp. 777–780. DOI: 10.1103/PhysRev.47.777.
- [22] Massimiliano Grazzini et al. “ $W\pm Z$  production at hadron colliders in NNLO QCD”. In: *Physics Letters B* 761 (Oct. 2016), pp. 179–183. ISSN: 0370-2693. DOI: 10.1016/j.physletb.2016.08.017. URL: <http://dx.doi.org/10.1016/j.physletb.2016.08.017>.
- [23] Florian Mintert et al. “Measures and dynamics of entangled states”. In: *Physics Reports* 415 (2005), pp. 207–259.
- [24] Florian Mintert et al. “Measures and dynamics of entangled states”. In: *Physics Reports* 415 (2005), pp. 207–259. DOI: 10.1016/j.physrep.2005.04.001. URL: <https://doi.org/10.1016/j.physrep.2005.04.001>.
- [25] Michael A. Nielsen and Isaac L. Chuang. *Quantum Computation and Quantum Information*. Cambridge: Cambridge University Press, 2000. ISBN: 9781107002173.
- [26] John Preskill. *Quantum Information and Computation*. <http://theory.caltech.edu/~preskill/>.
- [27] Chris Quigg. *Gauge Theories of the Strong, Weak, and Electromagnetic Interactions: Second Edition*. 2nd. Princeton: Princeton University Press, 2013. ISBN: 0691135487.
- [28] Matthew D. Schwartz. *Quantum Field Theory and the Standard Model*. Cambridge: Cambridge University Press, 2013. DOI: 10.1017/9781139540940.
- [29] R. L. Workman et al. “Review of Particle Physics”. In: *PTEP* 2022 (2022), p. 083C01. DOI: 10.1093/ptep/ptac097.